CRANFIELD UNIVERSITY

David Munro

Toward a Rigorous Derivation of a Stable and Consistent Smoothed Particle Hydrodynamics Method

School of Engineering

Crashworthiness, Impact & Structural Mechanics Group

PhD

Academic Year: 2012 - 2015

Supervisor: Dr James Campbell

November 2015

Executive Summary

The aim of this thesis is to provide an investigation toward a rigorous derivation of a stable and consistent numerical method based on the established Smoothed Particle Hydrodynamics method. The method should be suitable for modelling the large deformation transient response of fluids and solids, the interests of the Crashworthiness, Impact and Structural Mechanics group (CISM) at Cranfield University.

A literature review of the current state of the art of the SPH method finds that the conventional SPH equations are not derived in a rigorous way, often the equations are manipulated into a mathematically equivalent form in order to preserve conservation of linear momentum, which often leads to different results; the reasons for this are unknown and it is not fully understood how each particular form of the discrete equations effects the solution in terms of stability, accuracy and convergence. This leads to specific objectives being defined which underpin the overall aim of the thesis.

The first objective is to develop an understanding of the SPH method and the implementation used at Cranfield University, this is done through a capability study which demonstrates the coupled SPH-FE method and a number of relevant improvements to the MCM code including the addition of a turbulence model and the modification of the SPH contact algorithm to model lateral forces between materials. This is demonstrated through the implementation of a friction model, which suggests that the contact algorithm is suitable for resolving lateral forces based on the relative velocity between materials, with the potential for coupling with a structural FE model.

The second objective focuses on the consistency between the discrete continuity equation and the momentum equation. The discrete forms of the governing equations do not correctly mimic their continuous counterparts for the conventional SPH forms of the equations; this is due to the discrete continuity equation not properly conserving volume, which is implied by the momentum equation in continuous form. A correction is applied to the momentum equation which accounts for the effect of this loss of volume in the calculation; the effect of this correction is tested for its impact on the stability properties of the method, with results suggesting that the source of the instability lies elsewhere.

The third objective focuses on the accuracy and consistency of the SPH method; the literature review concludes that the conventional form of the SPH equations cannot properly replicate the gradient of a constant, non-zero field. However the discrete analogue of the continuous equations implies that this is done correctly, the implications of this not being well understood. A form of the governing equations is derived rigorously which naturally removes any error that arises due to this incorrect gradient approximation, and the implementation is tested on the effect on numerical stability. The results suggest that the modified method is stable for the test cases that are selected, a stability analysis is performed which provides a region of stability for the modified SPH form.

The final objective looks toward the finite element method (FEM) for potential improvements to the method. Mixed element methods are commonly used in FEM and allow more than one field variable to be interpolated independently of one another, this can be used to alleviate problems that are subject to volumetric locking and the problems associated with the under integration of elements, which can be viewed as analogous to the issues that appear with particle methods. For those reasons, the mixed element approach is identified as a potential route toward achieving the overall aim. A mixed SPH form is developed based on the Hu-Washizu principle, which is tested against the same benchmark tests for stability used throughout the thesis, concluding that the independent interpolation of field variables does not stabilise the method for the particular test case used, and for the particular mixed form that was identified.

Keywords: Mixed Methods, Hu-Washizu, Background Stress, Conservation of Volume, Friction modelling, Contact

Structure of the Thesis

This thesis consists of nine main chapters. The first three are introductory, followed by the main discussion and results in the next six sections.

Chapter One – Introduction

The first chapter introduces the aims and objectives of this work. The SPH method is introduced by literature review describes the evolution of the method and current areas of research.

Chapter Two – SPH Theory

The mathematical theory of the SPH method is described and the discrete continuity and momentum equations are derived in full. The time integration scheme used in the MCM (Meshless Continuum Mechanics) code is described.

Chapter Three – Outstanding Issues

An in depth literature review is presented here which focuses on the issues associated with the SPH method and the attempts that have been made to address them.

Chapter Four – Capability Study of the SPH Method

The current capability of the SPH method is demonstrated in a series of test problems, the impact of a rigid cylinder on water and the response of a solid plate subjected to loading from underwater explosions. The details of a turbulence model are described an implemented in the MCM code which adds functionality and extends the current modelling capability.

Chapter Five – Modelling Lateral Contact Forces in SPH

The contact algorithm is adapted to model lateral forces between two SPH materials; the algorithm is implemented and verified for several test cases, opening up potential for lateral forces to be resolved in a full FSI problem.

Chapter Six – Correcting for Loss of Mass Continuity

A possible source of error in the SPH framework is identified and corrected in this chapter, which to date has not been done in SPH in this way. The continuous derivation of the governing equations demonstrates that the conventional SPH equations do not properly mimic the properties of their continuous counterparts; the effect of the correction on the numerical stability is investigated and discussed.

Chapter Seven – Corrections on Interpolation Errors in SPH

An artefact of the SPH kernel interpolation method is identified and discussed in this chapter, an alternative set of SPH equations is derived rigorously and tested against several problems for the effect on numerical stability, conclusions are made and a stability analysis of the new set of equations is presented.

Chapter Eight – Mixed Methods in SPH

The mixed element method is identified as a potential route toward improving stability properties of the SPH method. In this chapter the mixed element method is discussed as is it applied in the finite element method, leading to an equivalent SPH implementation which is tested for its effect on numerical stability.

Chapter Nine – Conclusions and Future Work

A final discussion and recommendations for future work are presented here.

Acknowledgements

I would like express my gratitude to my supervisor, Dr James Campbell, for his invaluable advice throughout the duration of this research project, and especially for his understanding and patience over the final write-up period. I also recognise that this research project was part funded by the EU SMAES project without which, this research would not have been possible. Further thanks go to the staff within the Crashworthiness, Impact & Structural Mechanics group at Cranfield University, in particular Professor Rade Vignjevic, for his ideas and advice over the last three years.

Without the support and encouragement of my wife, Nas, and my parents, I would never have been able to get through the last three years. Thank you.

Table of Contents

List of Figures

NomenclatureW_{ij} – Kernel function centred at position i and evaluated at position j

∇W_{ij} – Spatial derivative of kernel function

np – Total number of particles in domain

$nnbr$ – Number of neighbouring particles

σ – Cauchy stress

D – Rate of deformation

v – Velocity

u – Displacement

$\bar{}$ - Overbar: Averaged or mean value

$\tilde{}$ - tilda: Fluctuation from mean

p – Pressure

m – Mass

ρ – Density

E – Internal energy

$\theta(t)$ – Angle as a function of time

μ - Coefficient of friction

f_c – Contact force between two materials

f_f – Friction contact force between two materials

ξ – Spatial co-ordinates

δ – Dirac delta function

Ω – Volume

Γ – Surface

$\nabla \cdot ()$ – Divergence operator

$\frac{D}{Dt}$ - Material derivative

h - Smoothing length

$\dot{\varepsilon}$ – Strain rate

$\dot{s}$ – Deviatoric stress rate

Δt – Timestep

c – Speed of sound

N – Finite element shape function

Δp – Particle spacing

b – Body force

dim – Dimensions

1 Introduction

1.1 Background

Over the last few decades, a great deal of effort has been directed towards the development of new computational tools for engineering analysis and the improvement of the existing methods. It is clear how valuable computer models have become to the engineering industry, and has led to many engineers using numerical models in conjunction, or even instead of experimental models.

The great advances in computing now mean that the restrictions on memory that would prevent large models from being run only a few years ago are no longer a problem, meaning that very complex problems can in theory be solved. However it is crucial to be able to understand the numerical methods that are used for each particular problem and the underlying assumptions that go with them.

Historically fluids and structures would be treated separately, the structure would be analysed using a finite element model, with various assumptions made regarding the load, and similarly the behaviour of fluid would be understood through CFD models. This eventually led to a separate class of methods used for problems classed as 'fluid structure interaction' allowing transient analysis of a structures response to external loading from a particular fluid, for example, loading from water on the bottom of an aircraft when it ditches, or perhaps high velocity impacts such as bird-strike where heavy damage to aircraft engines are caused by birds during flight or take off. A great number of these problems exist many with important engineering application.

The particular focus of this research is on the numerical modelling of the transient non-linear response of a structure subject to fluid loading. This work is conducted in the Crashworthiness, Impact & Structural Mechanics (CISM) group at Cranfield University and some of their areas of interest include aircraft ditching, bird-strike, high velocity impacts and underwater blast cases

In this range of problems the primary goal is to determine the structural response of the material in question, a popular numerical tool for this problem is finite element analysis (FEA). However in order for an accurate prediction of structural loads, the fluid must also

be modelled accurately. This is the primary motivation in the study of smoothed particle hydrodynamics (SPH), a technique that can be easily coupled with finite element methods (FEM) in order to solve fluid structure interaction problems. This method has its advantages and disadvantages which will be explored in chapter three, but it is generally agreed that the improvement of this numerical tool could lead to great benefits to the engineering industry and enable a much wider class of problem to be addressed, through an improved fluid model, leading to more accurate structural load predictions.

1.2 Smoothed Particle Hydrodynamics

Smoothed particle hydrodynamics (SPH) is a method for approximating the solutions to partial differential equations. Although the underlying method is appropriate to approximate any given function and its derivative, it is assumed that when we are discussing SPH, the approximation of partial differential equations will refer to the equations governing the continuity of mass and momentum.

The key difference between these mesh free methods and CFD methods such as finite difference, finite volume and finite element is that there is no need to provide connectivity between computational nodes by means of a grid/mesh.

In the finite difference method adjacent nodal points in a structured grid are used to evaluate the function gradient at a point, which is then used to advance the solution, similarly in the finite volume method the integral equations are discretised in order to find cell averaged values leading to flux calculations and so on, different again is the finite element method where the objective is to find the coefficient of some shape function, which can then be used to evaluate displacements at certain points within the material.

SPH however does not rely on a structured grid or even on any grid connectivity at all for that matter, the gradients are calculated point wise using neighbouring points and an approximating function (similar to the finite element shape function) which is defined over some smoothing length, this allows a Lagrangian type of approach where the field variables are carried along with the particles as they are moved, which, due to the lack of a structured grid is particularly useful for problems involving large deformations

The motivation for using such methods comes from the problems that are inherent from a method that requires a grid, such as problems with free surface flows, deformable boundaries and moving interfaces as well as the modelling of large deformations and complex mesh generation.

SPH is in fact one of the oldest of the mesh free methods, beginning in the 70's when it was developed in order to solve astrophysical problems [1]. Since its inception SPH has been extended into many other areas, including fluid structure interaction, free-surface flows& explosions.

Extensions of the SPH method in fluid flow include multiphase flow [2] and flow through porous media [3]. SPH was extended to problems involving material strength by adapting the method to work with the full stress tensor, first in two dimensions [4] and later in three dimensions [5]

Turbulence modelling techniques have been successfully extended to SPH in the form of Reynolds averaged, one & two equation models [6] [7], [8] [9] as well as attempts at large eddy simulations [10]. Extensive work on turbulence modelling in SPH has been published by Violeau [11].

The large effort involved in the research of SPH has uncovered a number of shortfalls of the method. Detailed analyses of SPH [12] have drawn attention to instabilities that develop under tension. Issues have been found with consistency and accuracy, which have since been addressed by kernel correction and normalization [13].

However there remains a number of details of the SPH method which are still not well understood by researchers, often the problems that are observed in the method are fixed through heuristic means, applying fixes or patches which appear to resolve problems when in fact they are simply covering up the root cause without identifying them. A detailed literature review of these topics in particular is presented in chapter three.

1.3 Aim

The aim of this thesis is to provide an investigation toward a rigorous derivation of a stable and consistent numerical method based on the established Smoothed Particle Hydrodynamics method.

The method should be suitable for modelling the large deformation transient response of fluids and solids, the interests of the Crashworthiness, Impact and Structural Mechanics group (CISM) at Cranfield University. Specific types of problem include bird-strike, high-velocity impact, aircraft ditching and the response of structures subject to loading from underwater explosion. For these types of problems, the correct treatment of the fluid behaviour is required in order to predict the structural loads.

The focus of this thesis therefore is on fluid behaviour using the SPH model, suitable for coupling with a structural finite element model.

Any changes to the underlying SPH method should be based on sound mathematical or physical principles and avoid the addition of heuristic fixes wherever possible. Any changes should be practical to implement and use, i.e. any increase in computation time should not render the method impractical and any assumptions made should be fully understood.

1.4 Objectives

A literature review (see chapter three) identifies that numerical stability properties of the SPH method are not fully understood despite receiving significant attention over recent years. Stability is essential in any numerical method and is identified as the main focus of research in this thesis and underpins the aim of the thesis discussed in §1.3. Given the main focus of the thesis, the following objectives are defined:

1.4.1 Develop Understanding of the SPH method

Review the current capability of the SPH method and provide a series of relevant improvements to the SPH code at Cranfield University (MCM), this develops a deep understanding of the SPH method and the MCM implementation setting a foundation for the remainder of the project.

a) *Capability Study* - Demonstrate the current capability of the SPH method to model fluid structure interaction problems with the coupled SPH-FE method.

b) *Turbulence Modelling* - Implement and verify the $k-\varepsilon$ two equation turbulence model in and SPH framework.

c) *Modelling Lateral Contact Forces* – The contact algorithm currently implemented in SPH allows normal contact forces between materials; the objective is to determine whether this contact algorithm is also suitable for resolving lateral forces between materials, using a friction model as the validation method.

1.4.2 Investigate the Discrete Continuity Equation and its Effect on Stability

A study of the SPH method is undertaken in chapter seven identifying an error in the discrete equations which means that the discrete equations no longer mimic the properties of their continuous counterparts properly.

There may be a link between the conservation properties of the discrete SPH momentum equation and stability. The study of these corrections on stability will form the basis of this objective.

One specific choice of correction will be identified and implemented in an SPH framework; the new method will then be tested for the effect on stability using two benchmark test cases.

1.4.3 Investigation into Errors in the Gradient Approximation in SPH

Some forms of the SPH equation appear to produce more accurate results than others, so far with no reasonable explanation. Also, the most popular forms of the SPH equations have not yet been derived rigorously and rely on certain assumptions for instance that the gradient of a constant function can be approximated correctly. The objective is to investigate the impact of these assumptions towards developing a stable and rigorously derived set of SPH equations.

One modified form of the SPH momentum equation will be derived, implemented and tested, this will be backed up by stability analysis to understand of the stability properties of the new modified SPH momentum equation.

1.4.4 Investigate the Compatibility of FEM Solutions with SPH

The finite element method (FEM) has become well established after much research effort, a number of issues with FEM appear to have analogies with those associated with SPH.

The use of mixed element methods have a number of benefits, in particular volumetric locking can be avoided in incompressible or nearly incompressible problems, avoiding the use of under integrating elements and hence hourglass modes. Mixed methods can be developed in many different ways, the objective is to identify one particular mixed form which can then be implemented in an SPH framework and tested for the effect on numerical stability.

1.5 Summary of Chapter One

The background of the SPH method has been presented in this chapter and the main aim of this research project has been identified; Specific objectives have been defined in order to meet this aim. In chapter two, the mathematical theory of the SPH method will be presented.

2 SPH Theory

In this section the SPH equations will be derived in full. The SPH method is based on the approximation of a continuous function which is achieved through a continuous approximation of the Dirac delta function. This approximation is then discretised an applied to the governing equations of motion, i.e. mass continuity and momentum.

SPH involves a discretization using a set of points, which hold no particular connectivity with each other, if the objective is to estimate the value of a function, $f(x)$ at a particular point then this is achieved by taking a weighted average over neighbouring points. Details of this function approximation are given in §2.1.

2.1 Approximations of Functions and their Derivatives

First the Dirac delta function is defined as:

$$\delta(\mathrm{x}) = \begin{cases} +\infty, & x=0 \\ 0, & x\neq 0 \end{cases} \tag{2.1}$$

This function will also satisfy the following property:

$$\int_{-\infty}^{+\infty} \delta(\mathrm{x}) dx = 1 \tag{2.2}$$

This can now be used to return the exact value of a particular function at a point:

$$\int_{-\infty}^{+\infty} f(x)\delta(x)dx = f(0) \tag{2.3}$$

When integrated the product of a function with the Dirac delta returns the value of the function at the point where the Dirac delta is singular.

The Dirac delta also satisfies the sifting property:

$$\int_{-\infty}^{+\infty} f(x)\delta(x-x')dx = f(x') \tag{2.4}$$

Since $\delta(x-x') = 1$ when $x = x'$, the reverse is also true:

$$\int_{-\infty}^{+\infty} f(x')\delta(x-x')dx = f(x) \tag{2.5}$$

It is this concept that forms the basis for the SPH method, we can now say:

$$\int_{\Omega} f(x')W(x-x')d\Omega \approx f(x) \tag{2.6}$$

Where in the above the Dirac delta has been replaced with a smoothing function, W and the integration is now performed over a volume Ω. Note in the (2.6) that the function is still in continuous form, but the function is approximated.

If the above equation is now discretized:

$$\sum_{j}^{N} f_j(x)W(x_i - x_j, h)d\Omega = \langle f_i(x)\rangle \tag{2.7}$$

Where the triangular brackets from now on represent an SPH interpolation of a function, j is the index over the neighbouring interpolation points over which the average is taken, and i denotes the point at which we are looking for an approximate solution. The total number of points in the domain is denoted by N.

The same process can be performed but now replacing the function $f(x)$ in (2.6) with its derivative $\frac{\partial f(x)}{\partial x}$ which results in:

$$\int_{\Omega} \frac{\partial f(x')}{\partial x} W(x-x')d\Omega \approx \frac{\partial f(x)}{\partial x} \tag{2.8}$$

However since the derivative of the function is unknown, some extra manipulation is required, (2.8) can be re-written as::

$$\int_{\Omega} \frac{\partial}{\partial x} f(x') W(x - x') d\Omega = \int_{\Omega} \frac{\partial}{\partial x} \big(f(x') W(x - x') \big) \, d\Omega - \int_{\Omega} f(x') \frac{\partial}{\partial x} W(x - x') \, d\Omega \tag{2.9}$$

Divergence theorem can then be used to express the volume integral (first term on the right hand side in (2.9)) as a surface integral.

$$\int_{\Omega} \frac{\partial}{\partial x} f(x') W(x - x') d\Omega = \int_{\partial\Omega} \big(f(x') W(x - x') \big) \cdot \hat{n} - \int_{\Omega} f(x') \frac{\partial}{\partial x} W(x - x') \; d\Omega \tag{2.10}$$

Where $\hat{n}$ is the unit vector normal to the surface.

The surface integral can be neglected since the assumption is made that the kernel function is zero on its boundary (compact support).

$$\frac{\partial}{\partial x} f(x) \approx - \int_{\Omega} f(x') \frac{\partial}{\partial x} W(x - x') \; d\Omega \tag{2.11}$$

Replacing the integral and kernel with their discrete counterparts:

$$- \sum_{j}^{N} f_j \cdot \nabla W\big(x_i - x_j, h\big) d\Omega = \langle \nabla f_i(x) \rangle \tag{2.12}$$

Resulting in an expression where the approximation for the derivative of a function can be calculated by the product of the function at the neighbouring points and the derivative of the smoothing function.

2.2 Governing Equations

The preceding approximation for a function and its derivative can now be applied directly to the governing equations of motion, i.e. Mass and momentum. In this section the governing equations of mass and momentum will be derived and then discretised into SPH form.

2.2.1 Mass Continuity

The motion of a continuum body (Figure 2-1) is described through kinematic relations, the displacement of a material point within a continuum body $\mathcal{B}$ can be described by the difference between its current position and original position

$$u(X,t) = \varphi(X,t) - X \tag{2.13}$$

Where $\varphi(X,t)$ is the mapping between the original configuration and the current configuration, and the capital X denotes the reference configuration. $\mathcal{B}$ possesses a mass, m, which is a measure of the amount of material contained in the body. The continuum mechanics approach is to assume that this mass is distributed continuously, with no discontinuities within a single material body. Mass can be described as a conserved quantity that cannot be created or destroyed, if a closed system is considered, the mass remains constant within some bounded region, but the volume is able to change.

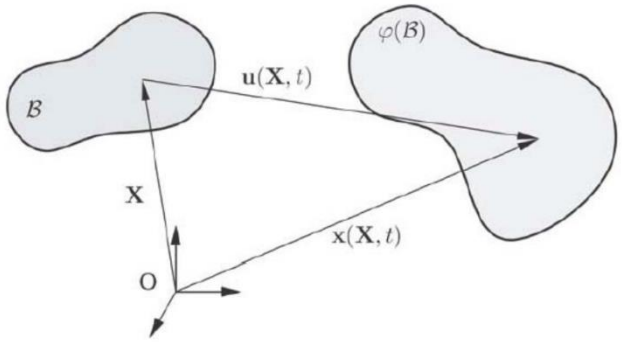

Figure *2-1 Deformation of a Continuum Body*

2.2.2 Derivation of Mass Continuity Equation

The derivation of the continuous continuity equation in Eulerian form will now be presented

Firstly the mass is written as an integral of density over an infinitesimal volume, where its rate of change in time will be written;

$$\frac{d}{dt}\int_{\Omega} \rho \, dV \tag{2.14}$$

Reynolds transport theorem then allows the time derivative to be moved to the inside of the integral.

$$\frac{d}{dt}\int_{\Omega(t)} \rho \, dV = \int_{\Omega(t)} \frac{\partial}{\partial t}\rho \, dV + \int_{\partial\Omega(t)} (v \cdot \hat{n})\rho \, dS \tag{2.15}$$

Divergence theorem is then applied, allowing the flux of mass through the surface to be associated with its behaviour within the volume.

$$\int_{\partial\Omega(t)} (v \cdot \hat{n})\rho \, dS = \int_{\Omega(t)} \rho(\nabla \cdot v) \, dV \tag{2.16}$$

$$\frac{d}{dt}\int_{\Omega(t)} \rho \, dV = \int_{\Omega(t)} \frac{\partial}{\partial t}\rho \, dV + \int_{\Omega(t)} \rho(\nabla \cdot v) \, dV \tag{2.17}$$

Conservation of mass requires that the mass remains unchanged throughout the motion of Ω, therefore

$$\frac{d}{dt}\int_{\Omega(t)} \rho \, dV = \int_{\Omega(t)} \frac{\partial}{\partial t}\rho \, dV + \int_{\Omega(t)} \nabla \cdot (\rho v) dV = 0 \tag{2.18}$$

The volume in the expression above is arbitrary and therefore the integral can be removed since all terms can be considered to be point-wise equal.

$$\frac{D\rho}{Dt} = -\rho(\nabla \cdot v) \tag{2.19}$$

The material derivative $\frac{D\rho}{Dt}$ is equal to.

$$\frac{D\rho}{Dt} = \frac{\partial \rho}{\partial t} + v \cdot \nabla \rho \tag{2.20}$$

2.2.3 Derivation of Momentum Conservation Equation

A similar process is followed to derive the conservation of momentum.

Writing the time rate of change of the total momentum within a [closed] volume as:

$$\frac{d}{dt}\int_{\Omega} \rho v \; dV \tag{2.21}$$

Applying Reynolds transport theorem in order to bring the integral to the outside,

$$\frac{d}{dt}\int_{\Omega} \rho v \; dV = \int_{\Omega} \frac{\partial}{\partial t}\rho v + \int_{\partial\Omega} (v \cdot \hat{n})\rho v \; dS \tag{2.22}$$

Then using divergence theorem to change the surface integral to a volume integral,

$$\int_{\partial\Omega} (v \cdot \hat{n})\rho v \; dS = \int_{\Omega} \rho v(\nabla \cdot v) \; dV \tag{2.23}$$

This provides an expression which can then be balanced with the forces acting on the surface.

Newton's second law tells us that a change in momentum is due to a force acting on the body. We assume that the Cauchy stress represents the traction forces.

$$\frac{d}{dt}\int_{\Omega} \rho v \; dV = \int_{\partial\Omega} (\sigma \cdot \hat{n}) \; dS \tag{2.24}$$

Therefore, after making further use of divergence theorem

$$\int_{\Omega} \frac{\partial}{\partial t} \rho v \, dV + \int_{\Omega} \rho v (\nabla \cdot v) dV = \int_{\Omega} \nabla \cdot \sigma \; dV \tag{2.25}$$

Which can be considered point wise equal, leading to:

$$\frac{\partial}{\partial t} \rho v + \rho v (\nabla \cdot v) = \nabla \cdot \sigma \tag{2.26}$$

Expanding the first term on the left hand side and re-arranging:

$$\rho \left(\frac{\partial v}{\partial t} + v \cdot \nabla v \right) + v \left(\frac{\partial \rho}{\partial t} + \rho (\nabla \cdot v) \right) = \nabla \cdot \sigma \tag{2.27}$$

The second term on the left hand side can be neglected assuming the mass continuity equation holds exactly (2.19),

$$\rho \left(\frac{\partial v}{\partial t} + v \cdot \nabla v \right) = \nabla \cdot \sigma \tag{2.28}$$

Finally writing the left hand side as the material derivative:

$$\rho \left(\frac{Dv}{Dt} \right) = \nabla \cdot \sigma \tag{2.29}$$

2.2.4 Mass Continuity Equation in SPH Form

Starting from the mass continuity equation written in continuous form (2.19)

$$\frac{D\rho}{Dt} = -\rho (\nabla \cdot \boldsymbol{v}) \tag{2.30}$$

Integrating each side and multiplying by the kernel function

$$\int_{\Omega} \frac{D\rho}{Dt} W(x - x', h) = -\int_{\Omega} \rho \nabla \cdot \boldsymbol{v} W(x - x', h) \tag{2.31}$$

In the next step we wish to move the divergence operator over to the kernel function, but first, as an intermediate step we will write:

$$\frac{\partial f}{\partial x} = \frac{1}{\phi}\left(\frac{\partial(\phi f)}{\partial x} - f\frac{\partial \phi}{\partial x}\right) \tag{2.32}$$

f and ϕ here are arbitrary and differentiable functions of x, putting the above in SPH:

$$\langle\frac{\partial f_i}{\partial x}\rangle = \frac{1}{\phi_i}\sum_j^{np}(\phi_j f_j)\nabla W_{ij}\frac{m_j}{\rho_j} - \frac{1}{\phi_i}f_i\sum_j^{np}\phi_j\nabla W_{ij}\frac{m_j}{\rho_j} \tag{2.33}$$

Now, if *f* is set as the velocity and ϕ is set to 1, we arrive at:

$$\langle\frac{D\rho}{Dt}\rangle = -\rho_i\sum_j^{np}\boldsymbol{v}_j\nabla W_{ij}\frac{m_j}{\rho_j} - \boldsymbol{v}_i\sum_j^{np}\nabla W_{ij}\frac{m_j}{\rho_j} \tag{2.34}$$

Simplifying (2.34):

$$\langle\frac{D\rho}{Dt}\rangle = -\rho_i\sum_j^{np}(\boldsymbol{v}_j - \boldsymbol{v}_i)\nabla W_{ij}\frac{m_j}{\rho_j} \tag{2.35}$$

It is clear to see from the derivation above that $f\frac{\partial\phi}{\partial x} = 0$ when $\phi = 1$, and hence $\boldsymbol{v}_i\sum_j^{np}\nabla W_{ij}\frac{m_j}{\rho_j} \approx 0$, when the particle distribution is uniform. However, including this term ensures that divergence vanishes when the velocity field is constant. For non-uniform particle distributions this is not necessarily true, this will be covered in detail in chapter seven.

2.2.5 Momentum Equation in SPH Form

Starting with the Cauchy momentum equation (2.19):

$$\rho\frac{Dv}{Dt} = \nabla\cdot\sigma \tag{2.36}$$

Similar steps can be followed to those deriving mass continuity:

$$\frac{Dv}{Dt} = \frac{\nabla\cdot\sigma}{\rho} \tag{2.37}$$

Using the quotient rule

$$\frac{Dv}{Dt} = \nabla \cdot \left(\frac{\sigma}{\rho}\right) + \sigma \cdot \left(\frac{\nabla \rho}{\rho^2}\right) \tag{2.38}$$

Integrating each side and multiplying by the kernel function, then linearizing the second term on the right hand side:

$$\int_{\Omega} \frac{Dv}{Dt} W(x - x', h) = \int_{\Omega} \nabla \cdot \left(\frac{\sigma}{\rho}\right) W(x - x', h) + \left(\frac{\sigma}{\rho^2}\right) \int_{\Omega} \nabla \rho W(x - x', h) \tag{2.39}$$

Writing in SPH form and moving the derivatives over to the kernel function:

$$\langle \frac{Dv}{Dt} \rangle = -\sum_{j}^{np} \frac{\sigma_j}{\rho_j} \nabla W_{ij} \frac{m_j}{\rho_j} - \frac{\sigma_i}{{\rho_i}^2} \sum_{j}^{np} \rho_j \nabla W_{ij} \frac{m_j}{\rho_j} \tag{2.40}$$

Simplifying (2.40):

$$\langle \frac{Dv}{Dt} \rangle = -\sum_{j}^{np} m_j \left(\frac{\sigma_j}{{\rho_j}^2} + \frac{\sigma_i}{{\rho_i}^2}\right) \nabla W_{ij} \tag{2.41}$$

2.2.6 Kernel Properties

After the equations are written in SPH form, an interpolating function must be chosen, various properties must be satisfied (see [14]) but the most popular choice is a cubic spline kernel. The smoothing length is normally chosen to be around 1.3 times the particle spacing, which has been shown mainly through trial and error to produce good results. The kernel properties mean that only the particles within the neighbourhood of the central particle need to be considered in the calculation, see Figure 2-2.

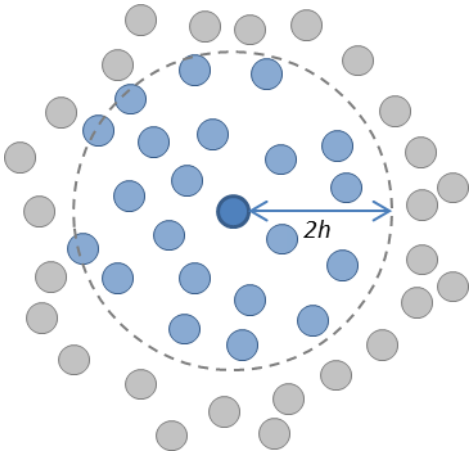

Figure *2-2 - Circle of influence in 2D SPH*

2.2.7 Consistency and Completeness

If the following conditions are satisfied:

$$\int_D W(x)dx = 1 \tag{2.42}$$

$$\int_D x^j W(x)dx = 0\,, 0 \leq j \leq k \tag{2.43}$$

Then the approximation is said to be of order k, and $\langle f(x) \rangle$ will conincide with $f(x)$ for polynomials of order less than k, When using the standard truncated Gaussian type kernels the approximation only hold for k less than or equal to one. This condition is commonly called consistency or completeness condition often used interchangeably.

This led to a correction being applied to the kernel functions as well as the gradient operator to ensure that these conditions are met and that the patch test is passed which is not the case for the conventional SPH method. A full derivation of the method implemented in the MCM code can be found in [13].

2.3 Structure of the SPH code

Now that the main equations have been presented, it is useful to understand how a solution is achieved using the SPH method, the semi discrete equations derived above now require an appropriate time integration scheme, in the MCM code, the central difference (Leapfrog) method is used.. The SPH interpolation is performed at two instances, once on the velocities to calculate the rate of deformation, which is then used to update the density, then once again on the stress tensor in the approximation of the particle acceleration which is in turn used to evolve the velocities and positions. Only the SPH part of the code is described, although it is noted that the method can be coupled with the finite element method through the use of a contact algorithm [15].

2.3.1 Central Difference Time Integration Algorithm

At the beginning of the time integration loop, the positions and time are known at time n, velocity and time-step size are held half a time-step back. The Cauchy stress, density, pressure and internal energy are known at the previous time n-1.

$$x^n, v^{n-\frac{1}{2}}, t^n, \Delta t^{n-\frac{1}{2}}, \sigma^{n-1}, \rho^{n-1}, P^{n-1}, E^{n-1}$$

1. Calculate strain rate

In the first step, the positions are pushed back by half a time-step in order to calculate the strain rate from the velocities, resulting in a strain rate (or rate of deformation at a half time-step back.

$$x^{n-\frac{1}{2}} = x^n - \frac{1}{2} v^{n-\frac{1}{2}} \Delta t^{n-\frac{1}{2}}$$

$$\dot{\varepsilon}^{n-\frac{1}{2}} = f(v^{n-\frac{1}{2}}, x^{n-\frac{1}{2}})$$

2. Update density

The time rate of change of density can be calculated from the rate of deformation, and hence the density can be updated to the current time.

$$\dot{\rho}^{n-\frac{1}{2}} = f(\dot{\varepsilon}^{n-\frac{1}{2}})$$

$$\rho^n = \rho^{n-1} + \dot{\rho}^{n-\frac{1}{2}} \Delta t^{n-\frac{1}{2}}$$

3. Update strength model

The deviatoric stress rate can now be calculated using a constitutive relation, performed of the strain rate, the stress can then be updated to the current time. Objectivity is satisfied by means of the Jaumann rate of the Cauchy stress.

$$\dot{s}^{n-\frac{1}{2}} = f(\dot{\varepsilon}^{n-\frac{1}{2}})$$

$$s^n = s^{n-1} + \dot{s}^{n-\frac{1}{2}} \Delta t^{n-\frac{1}{2}}$$

4. **Update speed of sound.**

The speed of sound is then calculated using the pressure and internal energy at the previous time.

$$c = f(P^{n-1}, E^{n-1})$$

The new time-step can now be calculated from the sound speed.

$$\Delta t_{crit}^{n-\frac{1}{2}} = f(c^{n-1}, l_{crit}^{n})$$

5. **Pressure and Internal energy**

The next step is to update the pressure and internal energy, this is done in an implicit calculation, the pressure at time n is calculated from the internal energy and the density, the pressure is then pushed back by half a step and used to calculate an increment in internal energy, which is then updated to the current time.

$$P^{n} = f(E^{n}, \rho^{n})$$

$$P^{n-\frac{1}{2}} = \frac{1}{2}(P^{n-1} + P^{n})$$

$$\dot{E}^{n-\frac{1}{2}} = f(P^{n-\frac{1}{2}}, \dot{s}^{n-\frac{1}{2}}, \dot{\varepsilon}^{n-\frac{1}{2}})$$

$$E^{n} = E^{n-1} + \dot{E}^{n-\frac{1}{2}}\Delta t^{n-\frac{1}{2}}$$

6. **Solve Momentum equation**

The momentum equation can now be solved to give an acceleration term at time n.

$$a^{n} = f(\sigma^{n}, \rho^{n})$$

At this point the variables can be outputted or the computation terminated if the desired time has been reached, if not the calculation continues

$$x^{n}, v^{n-\frac{1}{2}}, t^{n}, \Delta t^{n-\frac{1}{2}}, \sigma^{n}, \rho^{n}, P^{n}, E^{n}$$

7. **Calculate new time-step and update problem time.**

$$\Delta t^{n+\frac{1}{2}} = scale\ factor\ \times \Delta t_{crit}^{n+\frac{1}{2}}$$

$$t^{n+1} = t^n + \Delta t^{n+\frac{1}{2}}$$

8. **Update velocities.**

The velocity is updated to a half time-step ahead using the acceleration term and the current time-step

$$v^{n+1/2} = v^{n-1/2} + a^n \Delta t^n$$

$$\Delta t^n = \frac{1}{2}(\Delta t^{n-\frac{1}{2}} + a^n \Delta t^n)$$

9. **Update positions.**

Finally the positions can be updated using the updated velocities and time-steps.

$$x^{n+1} = x^n + v^{n+\frac{1}{2}} \Delta t^{n+\frac{1}{2}}$$

At the end of the integration loop the positions are known at the new problem time whereas the velocities are held a half time-step ahead as is standard practice in a central difference scheme.

$$x^{n+1}, v^{n+\frac{1}{2}}, t^{n+1}, \Delta t^{n+\frac{1}{2}}, \sigma^n, \rho^n, P^n, E^n$$

$$n = n + 1$$

2.4 Summary of Chapter Two

The details of the SPH method have been presented and the derivations for the discrete equations of mass and momentum are given. The time stepping scheme used in the MCM code to advance the solution is described.

3 Outstanding Issues

As discussed in chapter two, the SPH method has showed promise as it has developed over the last few decades, however it has still not become the industry standard in numerical modelling. The reason for this is that there are still a number of unanswered questions over the underlying method, which must be addressed.

This chapter provides a literature review of the various attempts at addressing the issues with the SPH method. First, the most important aspects common to numerical methods are introduced, convergence, consistency and stability. A literature review discusses these aspects as they are related to the SPH method, which provides the main motivation for directing effort towards achieving stability in the SPH method throughout the thesis.

3.1 Convergence, Consistency and Stability

A numerical method is said to converge if the approximate solution tends towards the exact solution as the resolution of the numerical model is increased. It is considered an essential property of any numerical scheme that is to be used in engineering analysis, detailed discussions of convergence can be found in many texts on numerical methods [16] [17] [18]. In SPH the choice of kernel type is important for convergence since less expensive kernels can in turn allow more particles to be included in the neighbourhood [19], however it becomes clear that achieving convergence is dependent on more that the method of interpolation used in the calculation.

Generally it is assumed that sufficient conditions for convergence are achieved when the total number of particles tends toward infinity $NP \to \infty$, and the smoothing length tends to zero $h \to 0$, allowing the number of neighbouring particles $nnbr$ to remain fixed. However this has been shown in [20] that this is not the case, and it is also necessary to increase the numbers of neighbours $nnbr \to \infty$ in order to achieve the conditions necessary for convergence. Leaving the number of neighbours fixed whilst changing the smoothing length and the total number of particles introduces and error which does not vanish as $NP \to \infty$ and $h \to 0$. It is also concluded in [20] that fixing the number of particles within the neighbourhood as the total number of particles is increased indicates an inconsistent scheme and leads to slow convergence rates.

The Lax equivalence theorem states that a consistent numerical scheme converges if and only if it is stable [21]. Consistency is also related to the accuracy of the method since for a numerical method to be consistent it must have an order of accuracy greater than zero [22].

Accuracy is the conventional SPH method is severely affected by particle disorder and lacks consistency, this manifests as errors in the force calculation which directly affects the rate of convergence, occurring especially in shear flows [19] Simple ideas to combat these errors such as increasing the number of particles in the neighbourhood have shown to be insufficient in solving these problems [19].

The problems of consistency and accuracy have been addressed by a number of authors, [23] [24], resulting in an SPH method with first order consistency achieved by renormalization of the smoothing terms, this also led to variants of the SPH method being developed which allow restoration of consistency or arbitrary order by means of a correction function. These methods include the element free Galerkin method [25] [26], the reproducing kernel particle method [27] and mesh-less local Petrov-Galerkin method [28]. Consistency has also been investigated in [29] where the truncation terms in the Taylor expansion were examined, showing that only the first order consistent approximation has acceptable convergence properties in the approximation of the first derivative. Convergence of various SPH schemes in one dimension was studied by [30], using first order consistent schemes with uniform and non-uniform particle distributions, providing estimates of the approximation error in both cases.

This leaves stability as the main property which must be satisfied in order to achieve convergence. Although stability of the SPH method has attracted significant interest at Cranfield University resulting in a number of PhD thesis [31] [32] [33] [34] and research papers [24] [35] and reviews [36], stability is still not fully understood, and remains a major topic of interest for researchers.

3.2 Stability of the SPH Method

Within the area of stability, a number of inter related issues arise, such as the tensile instability or particle pairing, zero energy modes, as well as issues with time stepping common to all explicit time integration methods, where stability is conditional on time-step size.

The un-physical clumping together or pairing or particles can be treated successfully by careful choice of interpolating kernel [37], however the same treatment does not work for the tensile instability, showing that different problems can manifest themselves in similar ways even though the underlying cause is quite different.

Tensile instability is named after the state in which it most often occurs, although it is possible, but less likely for it to occur during compression. The normal occurrence of the instability is when, during tension, not enough stress is developed between the particles at close distances which results in an unphysical clumping of the particles, this can look similar to mechanical fracture but has no physical meaning and can occur when modelling perfectly elastic materials.

The SPH method has been written in a total Lagrange formulation [35], which successfully removes the instability and restoring linear completeness and first order consistency, effectively correcting the main shortcomings of SPH. The Total Lagrange form also preserves homogeneity and isotropy of space through Noethers theorem [38] . The total Lagrange form involves a pullback to the reference configuration, this means that the neighbourhood of particles does not change throughout the calculation, therefore a search for neighbouring particles is not required at each time-step, meaning a less computationally expensive solution overall.

These improvements do come at a price however; It becomes impossible to model very large deformations, such as would occur in wave breaking or high velocity impact, which is a major advantage of the conventional form, this is down to the total Lagrange method using a fixed neighbourhood of particles throughout the computation.

Non collocated SPH was investigated by Dyka [39] as a treatment for the tensile instability in 1D, Belytschko further investigated instabilities in SPH separating the instability into two parts, the rank deficiency of the discrete equations and the distortion of the material instability [40]. The latter is the source of the tensile instability; in this case he used a Lagrangian kernel with the additional quadrature points, where stress is calculated. This method removes both of the instabilities that he defined. The stress point method was later extended to two dimensions [24]. The drawback here however is that extension to three dimensions is particularly challenging due to the difficulty in maintaining a full

neighbourhood of particles, particularly for violent fluid motion in which large deformations occur. [24] states that it cannot be guaranteed that in 2D and 3D simulations that when the stress points are moved with an interpolated velocity that there will be a sufficient number of particles of the correct type within the neighbourhood.

Monaghan [41] also attempted to remove the tensile instability by adding an artificial stress to the momentum calculation when the particles begin to move too close to each other, whilst producing a better looking result which removes particle pairing the method lacks physical meaning and is heuristic in nature, however he does note that the instability is especially visible in materials which use an equation of state which allow a negative pressures, although it can also occur in gases where only a positive pressure is possible. The artificial stress correction was later expanded to elastic problems by the same author [42], with further investigations made in PhD theses at Cranfield University [31].

Hicks writes that the instability can be removed through a shifting of the kernel properties in order to change the sign of its second derivative [43], which is important in the stability criteria presented by Swegle [12] who also addressed the problem by using conservative smoothing to control the instability growth [44] [45]. The authors did note however that smoothing in this fashion can smooth out more of the small wave length structures than is desired, although this method does still produce better results than the artificial viscosity method in many cases.

Morris [46] makes an important and interesting point that the tensile instability occurs when using a momentum equation of a type that conserves momentum exactly; performing stability analyses for a number of different forms of the momentum equation he notes that a form that is based on a pressure difference provides a stable solution. He also finds that increasing the order of the kernel towards Gaussian will generally improve stability.

Other attempts have been made to solve the tensile instability problem, notably Morris experimented with various interpolating kernels, which proved successful in some situations [46], Libersky [4] used conservative smoothing which involved the addition of dissipative terms to the solution, which was only successful in a number of specific cases. Chen [47] developed a corrective smoothed particle method (CSPM), which utilised stress points and artificial viscosity to improve stability for 2D plane stress problems.

The first study into tensile instability was published by Swegle [12] in which the instability was related to a negative pressure in combination with the sign of the second derivative of the kernel, which provides the stability criteria relating the sign of the stress to the second derivative of the kernel (see (3.1) and figure 3-1),. Von Neumann stability analyses have been performed by a number of authors including Balsara [48], Ferrarri [49], Swegle [12], and Gourma [32]. Balsara suggests limiting the smoothing length to the inter-particle distance [48], and Ferrari shows that the conventional method is unconditionally unstable. Form (3.1) of the momentum equation is stable; however this formulation is only applicable to fluids and does not deal with the full stress tensor as well as lacking a rigorous derivation.

$$\langle \frac{dv}{dt} \rangle_i = -\sum_{j=1}^{np} m_j \frac{p_j - p_i}{\rho_i \rho_j} \nabla W_{ij} \tag{3.1}$$

$$W''\sigma > 0 \tag{3.2}$$

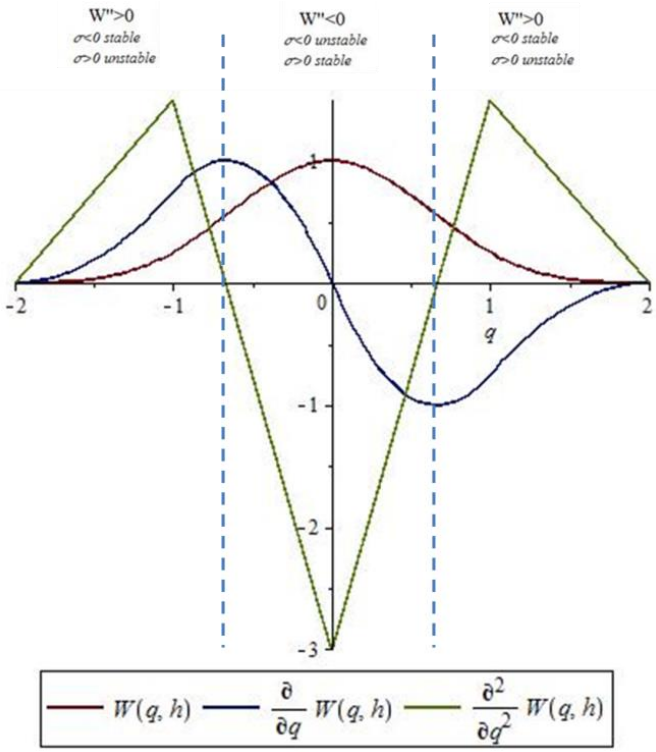

Figure *3-1 – Stability Regime for the Cubic B-Spline Kernel*

3.3 Benchmark Tests Cases for Numerical Stability

Throughout this thesis a number of numerical tests cases will be used to determine the effect of various modifications to the SPH method on the stability properties of the method. The first test case is taken from [12] and is referred to throughout the thesis using the authors name, the Swegle test.

3.3.1 Swegle Test

The test involves a body which is subjected to a uniform initial stress [12], either compressive or tensile, displacement boundary conditions ensure that the particles near to the boundary remain stationary and the initial stress is not relieved. The tests are achieved using the standard B-Spline kernel and no artificial viscosity is included in the calculation. A velocity perturbation of 10E-10 km/s is applied to a single particle at the centre of the body. A compressive stress exhibits no particle motion, however if the initial stress is tensile, unphysical particle motion is observed, the particle begin to clump together and tend to oscillate around single points. The uniform density is lost and the instability causes a sharp spike in the kinetic energy. The deformation of the particles in the Swegle test is demonstrated in Figure 3-2. The kinetic energy is plotted against time in figure 3-3 Figure 3-5, showing the influence of the initial stress levels on the instability growth. The Total Lagrange solution [35] provides a stable solution to the problem (Figure 3-4) where the kinetic energy oscillates close to zero due purely to numerical error. The details of the calculation and the material properties are given in table 1

Number of particles	625
Density	$1g/cm^3$
Smoothing Length	0.12cm
Total Mass	6.25g
Material Type	Fluid
Equation of State	Linear Polynomial
Time-step Size	$0.03\mu s$
Dimensions	2.4cm x2.4cm

Table 1 - Properties for the Swegle Test

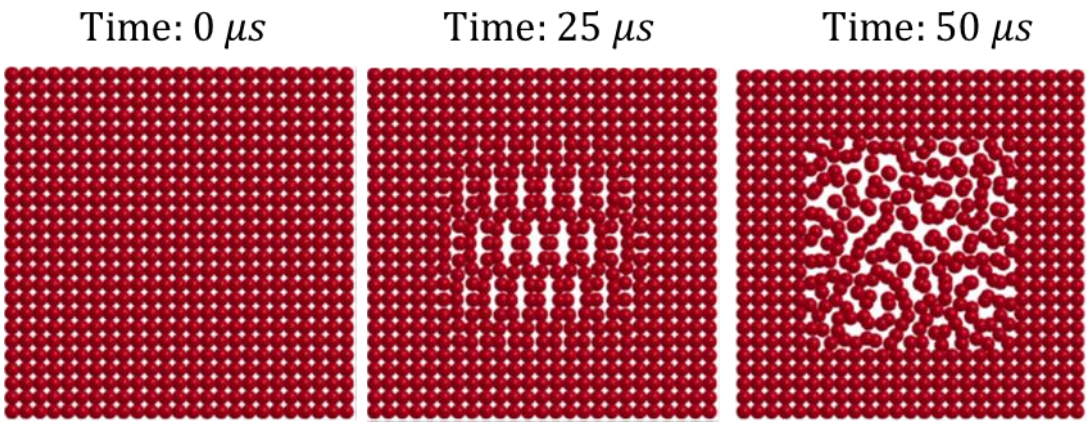

Figure *3-2 Swegle Test for Body Under Initial Tensile Stress*

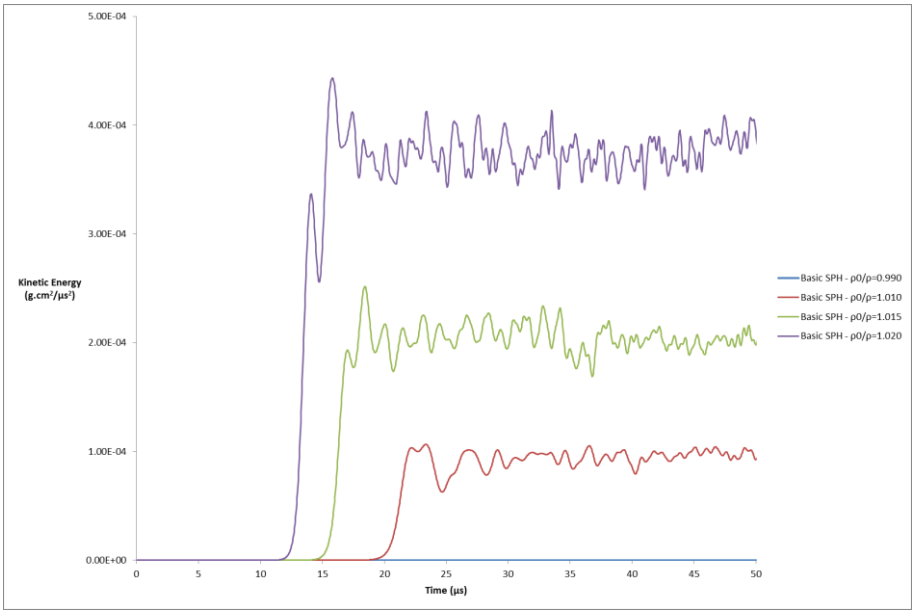

Figure *3-3 Kinetic Energy vs. Time for Various Levels of Initial Stress*

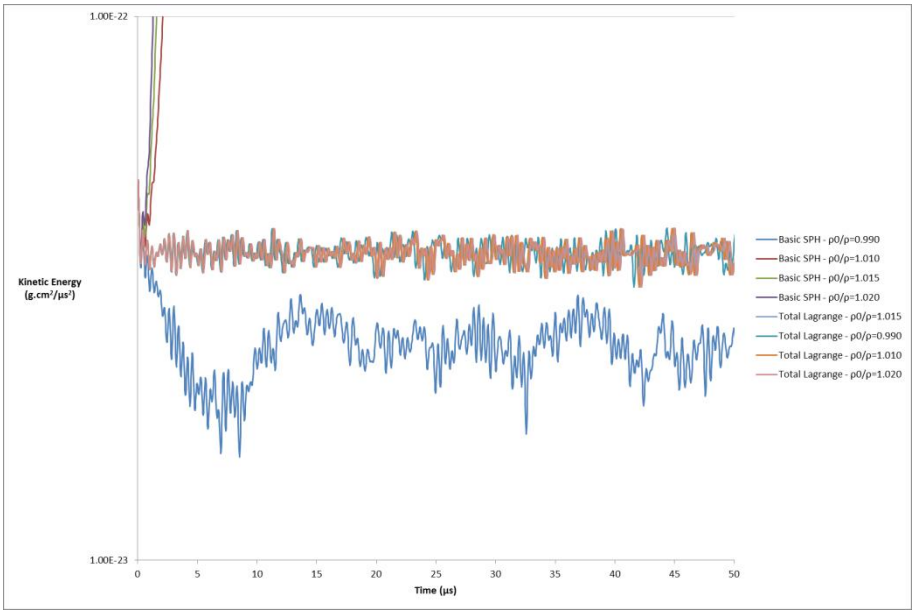

Figure *3-4 Close Up of Total Lagrange Solutions in Swegle Test*

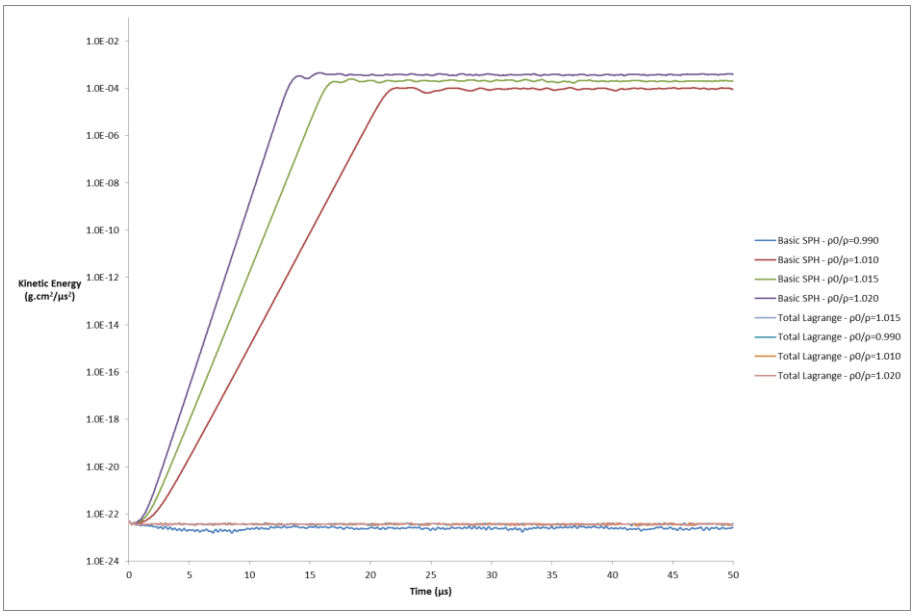

Figure *3-5 Kinetic Energy (Log Scale) vs. Time*

3.3.2 2D Plane Strain Elastic Impact

The second test case involves the purely elastic impact of two solid bodies at a relative velocity of 20m/s. The bodies are modelled with a uniform distribution of SPH particles, when the impact occurs a compressive wave travels along the length of the body, when the compression is relieved the body then goes into tension. With no damping this transition

between compression and tension will continue indefinitely as is shown in the analytical solution (Figure 3-7). The total Lagrange solution is stable and subject only to numerical damping, the basic SPH solution however breaks down when the problem goes into tension as shown in Figure 3-7 and the solution becomes meaningless due to the unphysical deformation that occurs, the manifestation of the instability is again shown as clumping of particles (Figure 3-6). The material is chosen to be rubber since the material properties allow a relatively large time-step size to be used, (compared to something like steel for example), the properties used in the calculation are given in Table 2. The analytical solution is calculated using the elastic wave speed (3.3) and the initial kinetic energy (3.4)

$$c_{solid} = \sqrt{\frac{E(1-v)}{\rho(1+v)(1-2v)}} \tag{3.3}$$

$$E_k = \frac{1}{2}mv^2 \tag{3.4}$$

Number of particles	3200
Density	1200kg/m^3
Smoothing Length	0.03cm
Total Mass	1200kg
Material Type	Elastic
Young's Modulus	1.5E+06 Pa
Poissons Ration	0.49
Dimensions	1mx2m (each body is 1mx1m)

Table 2 Properties for the 2D Plane Strain Problem

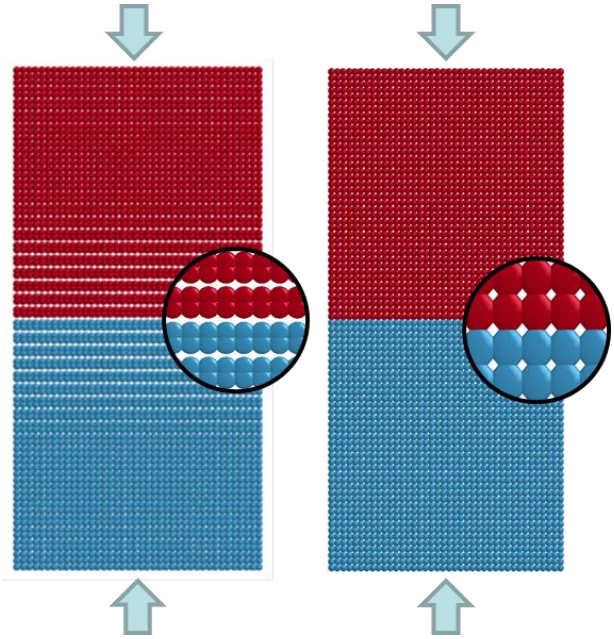

Figure *3-6 - Basic SPH Solution (left) and Total Lagrange Solution (right)*

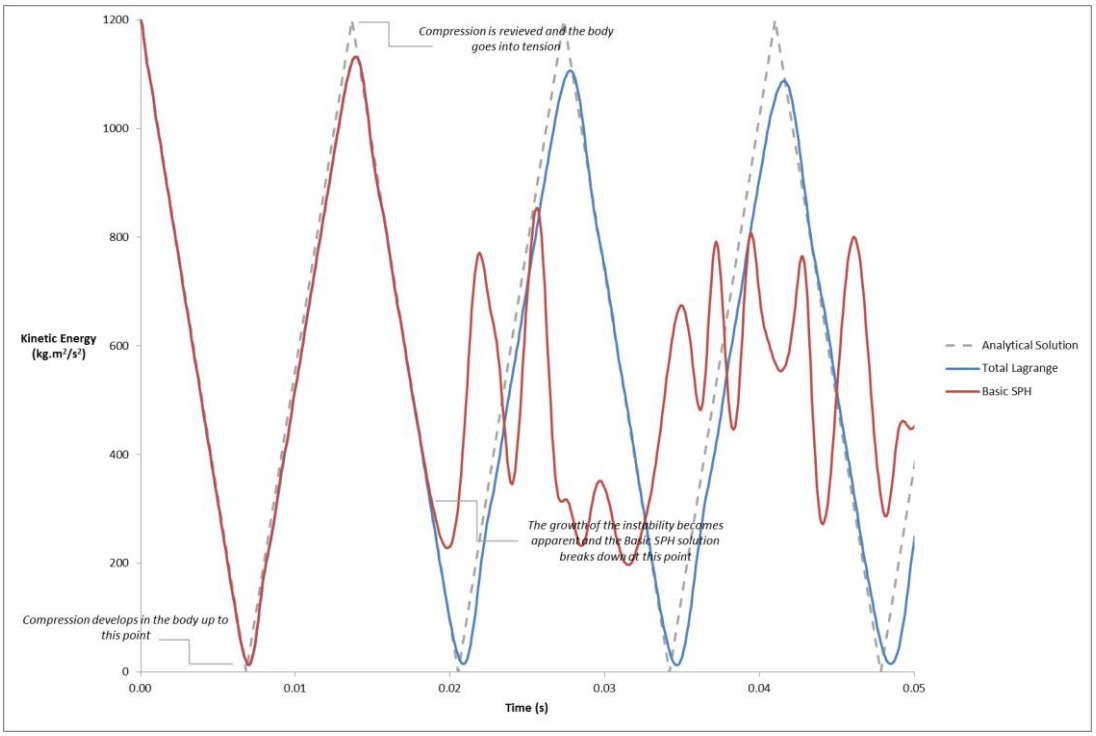

Figure *3-7 Kinetic Energy vs. Time for 2D Plane Strain Problem*

3.4 Motivation for Further Research

Although much effort has been directed toward the study of the stability properties of SPH, the solutions generally involve the solution to a numerical problem rather than the physical process, although such attempts are successful in supressing the instability they are not considered to address the root cause in a rigorous way. The addition of stabilising terms are also not based on a rigorous derivation of the governing equation, an example is the artificial stress, hence the name.

Therefore there are still areas which are not well understood, these areas form the motivation for further study in the later chapters, and are introduced in §3.5.

3.5 A Rigorously Derived SPH Framework

The SPH equations can be derived in a number of ways, it is well known [50] that some formulations work better than other in certain circumstances independent of the choice of interpolating kernel, the basic equations generally involve a heuristic modification in order to preserve conservation properties or to improve accuracy. For example, the most common form of the momentum equation (2.41) is modified in order to maintain symmetry between particle pairs [51] by adding a constant σ^i onto the stress term; ensuring that the forces exerted between two particles are equal and opposite, which is required in order to preserve conservation of linear momentum [52].

A number of derivations and implementations are possible for the SPH equations, various implementations have been tested in [53] concluding that the form of artificial viscosity implemented is of primary importance.

It is unknown what underlying assumptions are being made by these manipulations. As noted in §3.2, some form of the momentum equation show benefits for stability [46] but still lack a rigorous derivation.

The relationship between stability and conservation in SPH is not understood [36]. Lax-Wendroff theorem states that a conservative numerical scheme will converge toward a weak solution of the conservation law (if it does indeed converge), which potentially links conservation with stability and the other numerical properties discussed in §3.1. The summation form (3.5) of the density calculation does conserve mass exactly, however it is

normally beneficial to approximate the continuity equation directly (3.6), especially when contact between two materials occurs

3.6 Density Approximation in SPH

The approximation of density in the SPH method can be achieved in a number of ways, one method is to simply perform a summation over the masses of all particles within the neighbourhood.

$$\langle \rho \rangle_i = \sum_j^{nnbr} (m_j) W_{ij} \tag{3.5}$$

Which satisfies continuity requirements both locally and globally, a second method is to discretize the mass continuity equation which gives a rate form of the density, the SPH form is:

$$\langle \frac{\partial \rho}{\partial t} \rangle_i = \sum_j^{nnbr} (v_j - v_i) \nabla W_{ij} \frac{m_j}{\rho_j} \tag{3.6}$$

The advantage of (3.5)is that volume is conserved exactly, and is simplistic in nature since it gives a direct approximation for the particle density. However the main downside is that material density can become overly smoothed, especially in a case involving material discontinuities or even free surface flows where the density will drop towards the surface of the fluid, [54] [55], leading to oscillations on the surface due to the resulting pressure [55] This often leads to (3.6) being used instead, in this case the initial particle density can be set at the start of the calculation and will only change when relative motion between the particles occurs.

The SPH continuity equation however does not conserve mass exactly, or actually it is more correct to say that it is volume that is not conserved since the particle mass is normally assumed to stay constant throughout the calculation. The continuity equation also involves a modification to ensure that the gradient vanishes for a uniform velocity field, whereby the following relation is discretized rather than the function itself.

$$\frac{\partial f}{\partial x} = \frac{1}{\phi} \left(\frac{\partial (f\phi)}{\partial x} - f \frac{\partial \phi}{\partial x} \right) \tag{3.7}$$

Vignjevic [50] presented a set of SPH equations making the assumption of a moving co-ordinate system ((3.8) and (3.9)), which shows that by making the assumption of a moving referential coordinate system and a moving control volume, as opposed to the fixed referential coordinate system and fixed reference frame which is assumed by the conventional SPH method, a set of equations can be rigorously derived. This provides an explanation of the extra terms in the continuity equation It is also shown in [50] that this new set of equations gives similar results to those achieved using the conventional method. The SPH equations in a moving coordinate system are given in (3.8) and (3.9)

$$\langle\frac{\partial\rho_i}{\partial t}\rangle = \sum_{j=1}^{np}\frac{2\rho_j-\rho_i}{\rho_j}m_j\big(v_j-v_i\big)\nabla W_{ij} \tag{3.8}$$

$$\langle\frac{\partial\boldsymbol{v}_i}{\partial t}\rangle = \sum_{j}^{np}\frac{m_j}{\rho_j}(\boldsymbol{v}_j-\boldsymbol{v}_i)(\boldsymbol{v}_R\cdot\nabla W_{ij}) - \frac{1}{\rho_i}\sum_{j}^{np}(\boldsymbol{\sigma}_i+\boldsymbol{\sigma}_j)\nabla W_{ij}\frac{m_j}{\rho_j} \tag{3.9}$$

The SPH momentum equation is known to perform better when mathematical manipulations are made during the derivation, which essentially involves multiplying the function by an arbitrary function and discretizing, which can be done in such a way that guarantees that Newton's third law is met locally. Again, there is a lack of rigour involved in this approach as the discretization will depend upon the choice of test function.

Morris [46] writes that the tensile instability is especially likely to occur when a form of the momentum equations is used that conserves momentum exactly, which again highlights that the role of conservation is not well understood.

3.7 Comparison of FE and SPH

It is useful to compare various aspects of the SPH method to the finite element method (FEM), although there are fundamental differences in the methods, the finite element method is generally considered well established and is the industry standard for many engineering applications. Several analogies can be made between problems that arise in SPH with those in FEM which have received attention in the past. This comparison can potentially provide potential solutions to SPH issues if adapted correctly.

The conventional finite element method is a grid based method of solving partial differential equations based on the weak formulation of the governing equations, the finite element method makes use of a shape function to interpolate between a set of discrete points, analogies can be made between the shape functions and the interpolating kernel used in the SPH method [56]:

$$N_j(x) = W(x - x_j, h)\frac{m_j}{\rho_j} \qquad 3.10)$$

Detailed texts on the finite element method are widely available and include [57] covering general topics related to the method and [58], [59] which specifically focus on the explicit method.

Some issues that arise in the finite element include volumetric and shear locking, which are the terms used when the displacements calculated by FEM are much smaller than they should be, shear locking occurs when elements are subject to bending, and volumetric locking commonly occurs in incompressible problems. Locking will occur when elements are fully integrated, and can be dealt with by using under-integrated where the element is integrated using only a single point. However under integration in turn can produce hourglass modes which are spurious modes of deformation which produce zero strain energy. There is an analogy between hourglass modes in FEM and zero energy modes in SPH [14].

Hourglass modes can be treated in a number of ways, one possible treatment is through the use of mixed elements, allowing the element to be fully integrated without being subject to volumetric or shear locking. Mixed element method involves the independent interpolation of two or more field variables and is covered in depth in chapter 8 as well as in the literature [57] [59] [60].

3.8 Summary of Chapter Three

A literature review is presented on the issues that are currently outstanding in the SPH method, which require further research effort. Firstly the form of the SPH equations that is most often used in SPH implementations does not come from a rigorous derivation, meaning the underlying assumptions are not well understood. It is also not understood as to whether these underlying assumptions are related to the problems that occur with numerical stability.

4 Capability Study of the SPH method

4.1 Introduction

This chapter is presented in order to demonstrate the capability of the SPH method to solve the class of problems of particular interest as discussed in chapter one. Specifically these problems involve contact between a solid material and a fluid, which is achieved through the use of a coupled SPH-FE method where by solid structures are modelled using FEM and the fluid is modelled using SPH.

4.2 Mixed Kernel Interpolations

Referring to the structure of the SPH algorithm (see §2.3.1) we see that an SPH interpolation is performed at two instances, once on the velocity to update the density, and then again on the stress in the calculation of the acceleration. An initial study into the capability of the SPH method looks at whether using a combination of interpolating kernels can improve the solution. Three kernel functions are chosen, each interpolating function having its particular advantages, the functions are summarised in Table 3, where the value $q = \frac{|x|}{h}$.

Cubic Kernel (Figure 4-2) – This is the standard and most popular choice of kernel function, shown to provide good results in most instances.

Then it is intuitive then to choose one kernel of higher order than the standard choice, and one of lower order, perhaps the most obvious choice here is:

Quadratic Kernel (Figure 4-1) – This kernel always has a positive second derivative which could be useful when dealing with stability criteria.

Quintic (Wendland) Kernel (Figure 4-3) – Again this higher order kernel has shown improved accuracy in a number of cases.

Spline type	$W(r,h)$	$\frac{\partial W(r,h)}{\partial r}$	α_D	
			2D	3D
Quadratic	$\alpha_D\left[\frac{3}{16}q^2-\frac{3}{4}q+\frac{3}{4}\right] \quad 0\le q\le 2$	$\alpha_D\left[\frac{3}{8}q-\frac{3}{4}\right] \quad 0\le q\le 2$	$\frac{2}{\pi h^2}$	$\frac{5}{4\pi h^3}$
Cubic	$\alpha_D\begin{cases}1-\frac{3}{2}q^2+\frac{3}{4}q^3 & 0\le q\le 1\\ \frac{1}{4}(2-q)^3 & 1<q\le 2\\ 0 & q>2\end{cases}$	$\alpha_D\begin{cases}-3q+\frac{9}{4}q^2 & 0\le q\le 1\\ \frac{-3}{4}(2-q)^2 & 1<q\le 2\\ 0 & q>2\end{cases}$	$\frac{10}{7\pi h^2}$	$\frac{1}{\pi h^3}$
Quintic	$\alpha_D\left(1-\frac{q}{2}\right)^4(2q+1) \quad 0\le q\le 2$	$\alpha_D\left(-2\left(1-\frac{q}{2}\right)^3(2q+1)+2\left(1-\frac{q}{2}\right)^4\right) \quad 0\le q\le 2$	$\frac{7}{4\pi h^2}$	$\frac{21}{16\pi h^3}$

Table 3- Summary of Kernel functions and their Derivatives

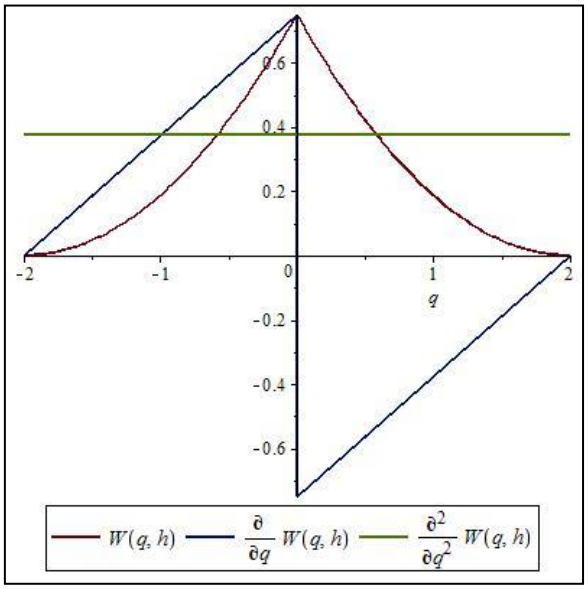

Figure *4-1 – Quadratic Spline and its derivatives*

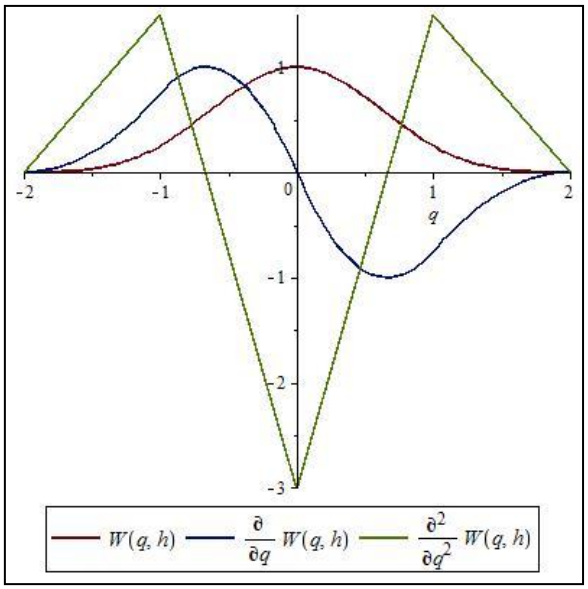

Figure *4-2 – Cubic Spline and its derivatives*

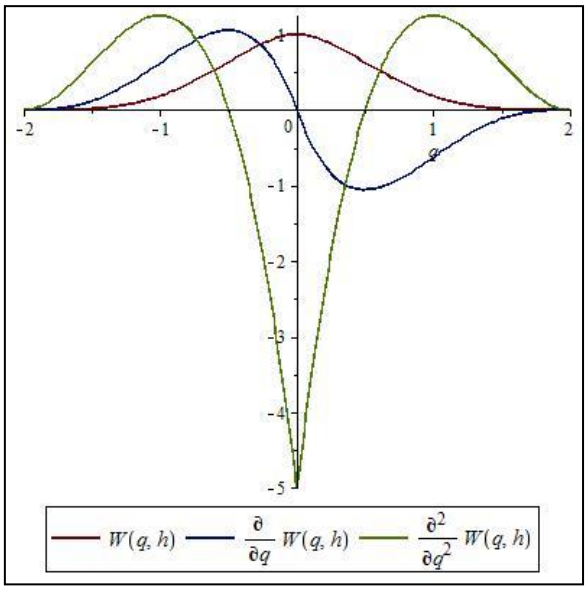

Figure *4-3 – Quintic Spline and its derivatives*

4.2.1 Mixed Velocity - Stress form

When investigating the use of mixed interpolating kernels it makes sense to conduct some simple tests, which are straightforward in SPH, since the SPH interpolation takes place at two instances as described before, it is possible to try a different interpolating function at each stage, here the three SPH kernel are tested in various combinations using the Swegle test, introduced in chapter three

4.2.2 Results

In this initial investigation no combination of interpolating kernels acts to remove the instability, so it therefore seems sensible to look towards other application of mixed kernels within the SPH method.

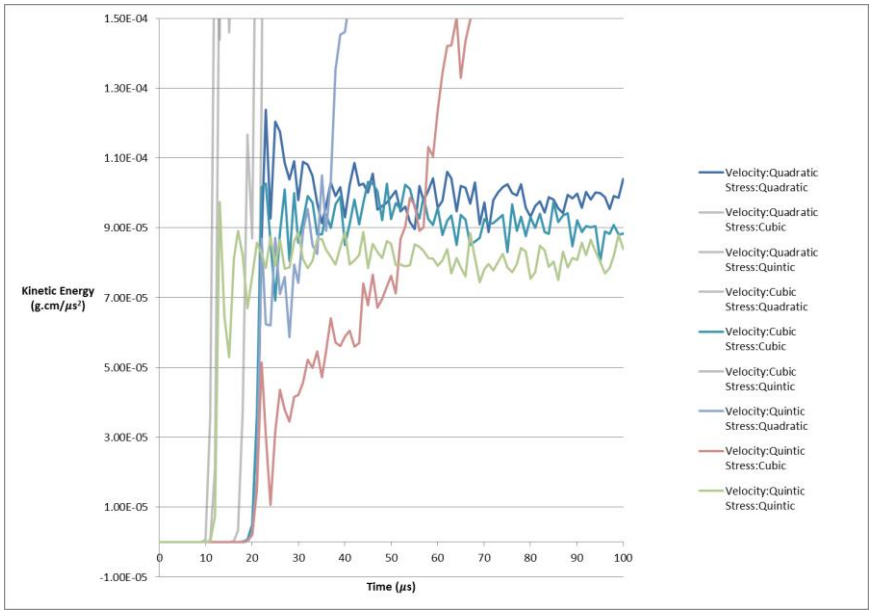

Figure *4-4 – Mixed kernel types for the velocity and stress interpolations*

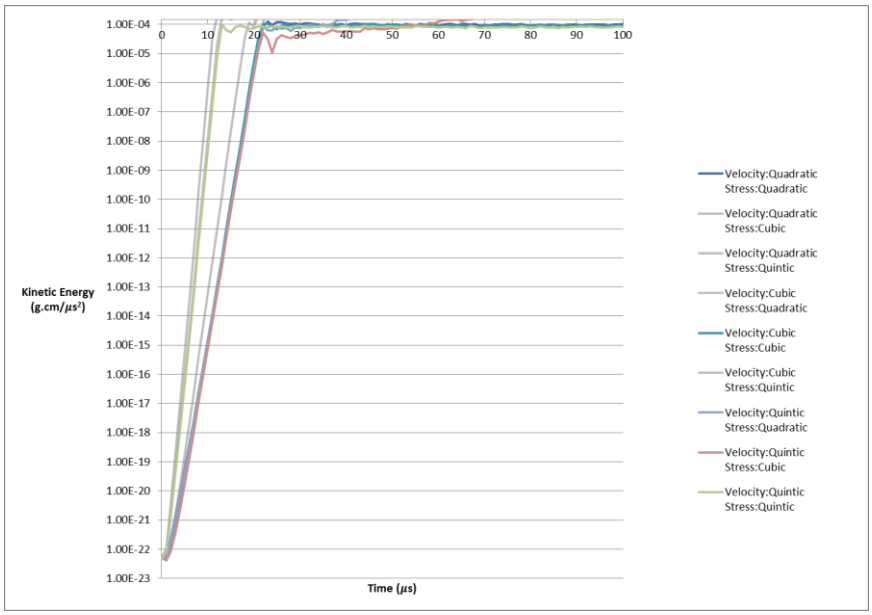

Figure *4-5 - Mixed kernel types for the velocity and stress interpolations (log scale)*

4.3 Mixed Pressure - Stress

The stress tensor can be split into a hydrostatic pressure term and a deviatoric stress term, or normal stresses and shear stresses in solid mechanics terms. it is possible to interpolate these parts separately and then combine them in order to update the particle positions. The justification for this comes from the fact that the stability relies on the second derivative of the interpolating kernel, it may therefore be possible to use a suitable interpolation for the pressure, causing the particle motion to remain physical, but to model the effect of the deviatoric stress differently.

The hydrostatic part of the stress tensor can be written as

$$\begin{bmatrix} -P & 0 & 0 \\ 0 & -P & 0 \\ 0 & 0 & -P \end{bmatrix} \tag{4.1}$$

Where P is the hydrostatic pressure, i.e. the average of the three normal stresses:

$$P = -\sigma_{HYD} = -\frac{\sigma_{11} + \sigma_{22} + \sigma_{33}}{3} \tag{4.2}$$

The deviatoric stress is now what's left after subtracting the hydrostatic stress:

$$\sigma' = \sigma - \sigma_{HYD} \tag{4.3}$$

So the three dimensional stress tensor can be written in two parts as:

$$\boldsymbol{\sigma} = \begin{bmatrix} \sigma_{11} - P & \sigma_{12} & \sigma_{13} \\ \sigma_{21} & \sigma_{22} - P & \sigma_{23} \\ \sigma_{31} & \sigma_{32} & \sigma_{33} - P \end{bmatrix} - \begin{bmatrix} P & 0 & 0 \\ 0 & P & 0 \\ 0 & 0 & P \end{bmatrix} \tag{4.4}$$

Which now means

$$\sigma' = \nabla \cdot \boldsymbol{\sigma} = (\nabla \cdot \boldsymbol{\sigma}') + (\nabla \cdot \boldsymbol{P}) \tag{4.5}$$

Which can be then discretised in the usual way, ending up with:

$$\left\langle \frac{Dv}{Dt} \right\rangle = \left(\sum_{j}^{np} -m_j \left(\frac{\sigma_j'}{{\rho_j}^2} + \frac{\sigma_j'}{{\rho_i}^2} \right) \nabla W_{ij}^{DEV} - \sum_{j}^{np} -m_j \left(\frac{P_j}{{\rho_j}^2} + \frac{P_i}{{\rho_i}^2} \right) \nabla W_{ij}^{HYD} \right) \qquad (4.6)$$

Where in (4.6) a distinction has been made between the SPH kernel function in each case, showing that it would be possible to use a different kernel for each part, producing another form of mixed SPH method.

4.3.1 Results

The graph below shows various kernel variations for the deviatoric and hydrostatic parts of the stress tensor using the elastic impact problem introduced in chapter three, it clearly shows that any combination still results in an unstable solution.

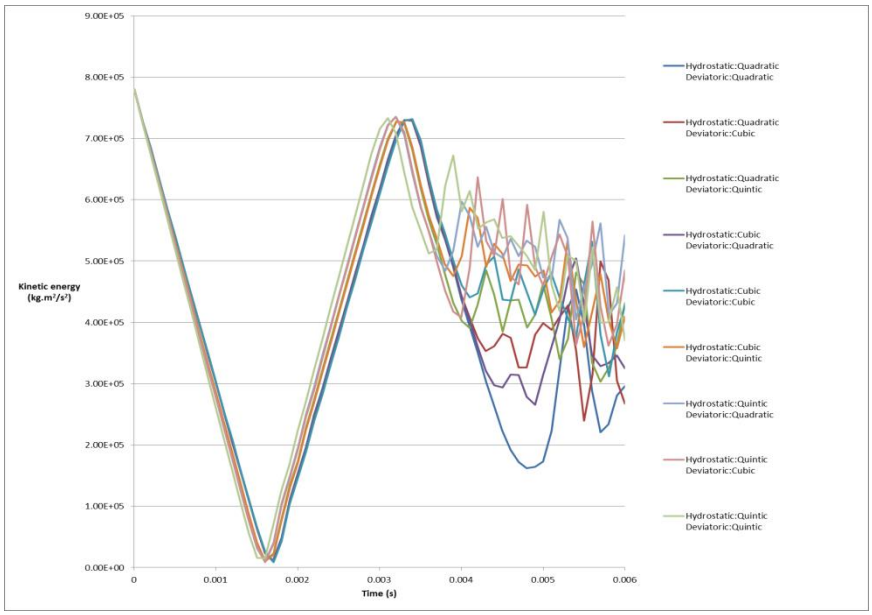

Figure *4-6 – Mixed kernel types for the deviatoric and hydrostatic parts of the stress tensor*

4.4 Vertical Impact of a Cylinder on Water

4.4.1 Introduction

This investigation focuses on the coupled FE-SPH method applied to the hydrodynamic impact of a long rigid cylinder on a large water pool as described in [61], the cylinder has a radius of 20.96cm and the impact velocity is a constant 7.38m/s. This has been modelled as

a 2D problem in SPH and the average pressure on the rigid cylinder is calculated and compared with that of the experiment.

The geometry used in the simulations is shown Figure 4-7.

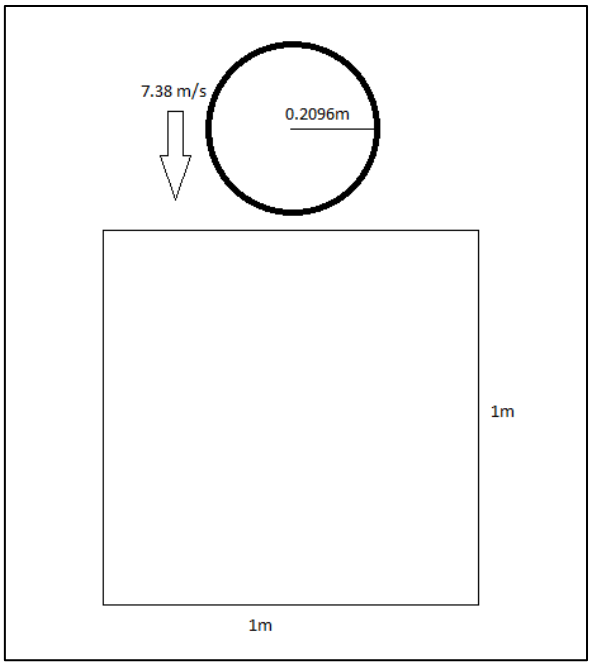

Figure *4-7 Geometry of cylinder impact problem*

The rigid cylinder is constructed from shell elements and the water domain is created using SPH particles, three different particle spacing's have been tested:

Spacing (m)	Particles across cylinder diameter	Time taken to travel distance Δp at 7.38m/s
0.005	41	6.78E-04
0.00375	55	5.08E-04
0.0025	83	3.39E-04

Table 1 - Relationship between particle spacing and diameter of the cylinder

4.4.2 Results

The average pressure is calculated by dividing the total force on the cylinder by the projected area of the cylinder and plotted against time, the time zero is defined as the time at which the cylinder has travelled a distance equal to that between the water and the closest point on the cylinder body, for the SPH results a pressure is detected before the

cylinder has reached the water, this is due to the contact being detected within a distance of twice the smoothing length.

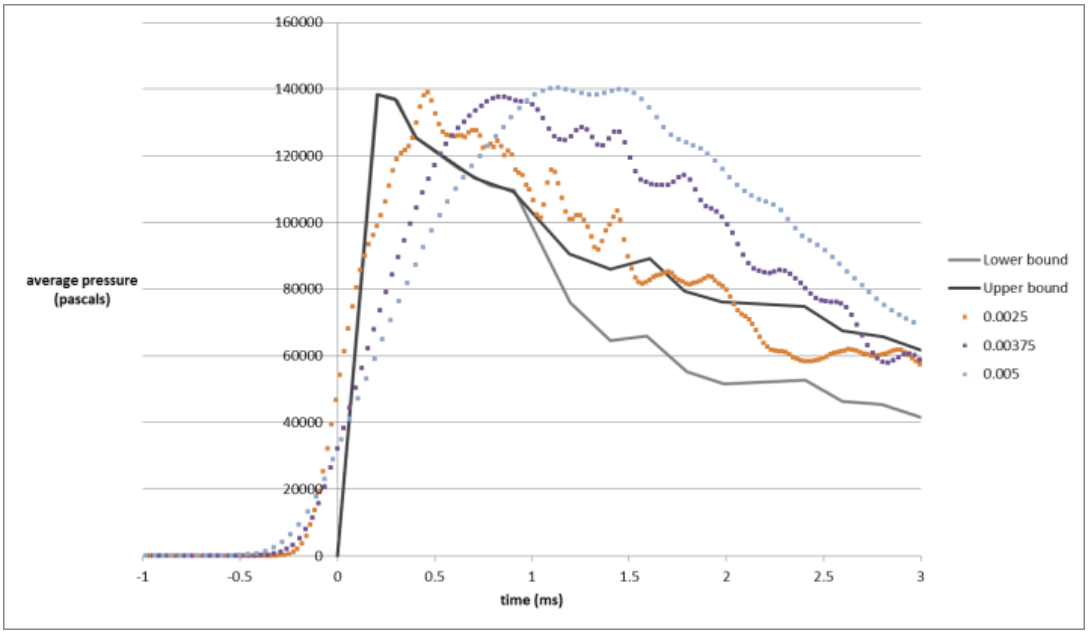

Figure *4-8 - Average pressure acting on the cylinder after impact at time zero*

4.4.3 Discussion

The peak pressure is predicted accurately in all cases, suggesting that particle spacing does not affect the peak pressure acting on the cylinder to a large degree. The results show convergence as the particle spacing decreases, however the resolution required in order to match the experimental results is high, requiring over 80 particles across the diameter of the cylinder. The results of this investigation are promising and therefore the next step is to extend the problem to three dimensions.

4.5 Impact of a Spherical Body on Water

4.5.1 Introduction

In this study, the impact of the Orion space capsule on water is simplified and modelled as a complete sphere that hits the surface of the water. The time histories of accelerations are compared to those recorded in an explicit finite element simulation. See [62] The dimensions of the space capsule are shown below along with the dimensions of the sphere used in the SPH simulations.

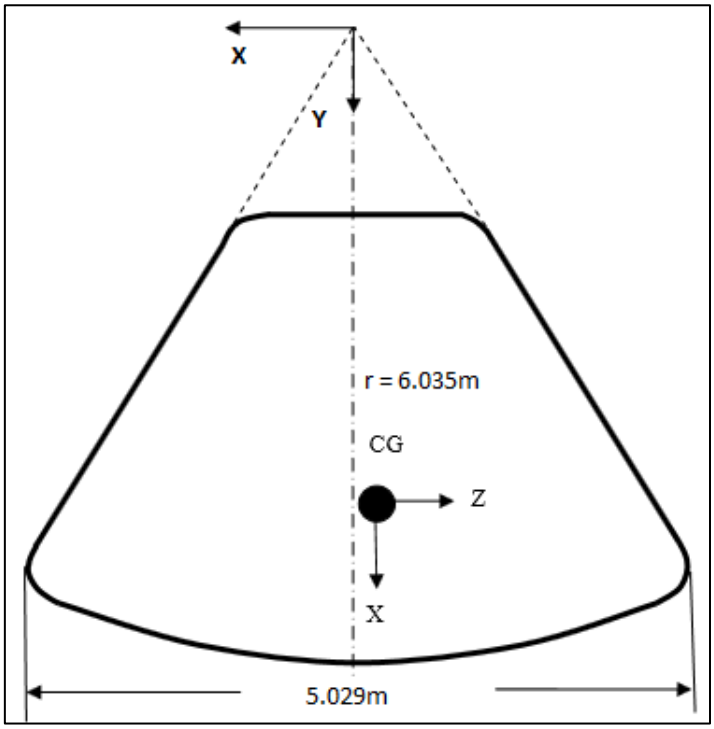

Figure *4-9- Dimensions of the Orion capsule, Source: [62]*

Centre of gravity location (m)	Moment of inertia (kg/m2)
X= -0.0652	I_{xx}= 19363.91
Y= 3.404	I_{yy}= 23622.199
Z= 0.0127	I_{zz}= 20829.95

Table 2. Inertial properties of the sphere

The mass of the space capsule is 7348kg, which is the same mass used for the complete sphere, also the same properties are used for centre of gravity and moments of inertia as [62]above.

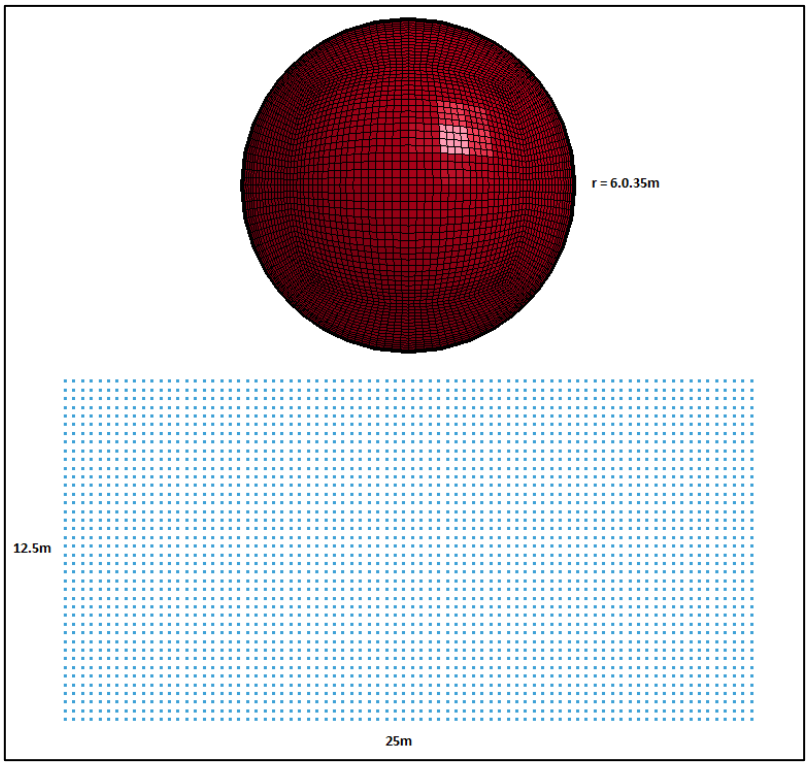

Figure *4-10 - FE-SPH Problem Setup for 3D Sphere Impact*

Referring to the 2d simulations, a particle distance equating to around 40 particles across the diameter of the cylinder was enough to properly predict the peak force acting on the surface. The same is assumed for the 3d case to begin with and the inter particle distance is chosen as 0.3125m. This is approximately equal to the size of each element on the surface of the sphere.

4.5.2 Results

The graph above shows the acceleration, in g's for the finite element simulation as well as basic SPH and basic SPH with gravity applied to the water. The peak acceleration is not predicted accurately in the SPH simulation.

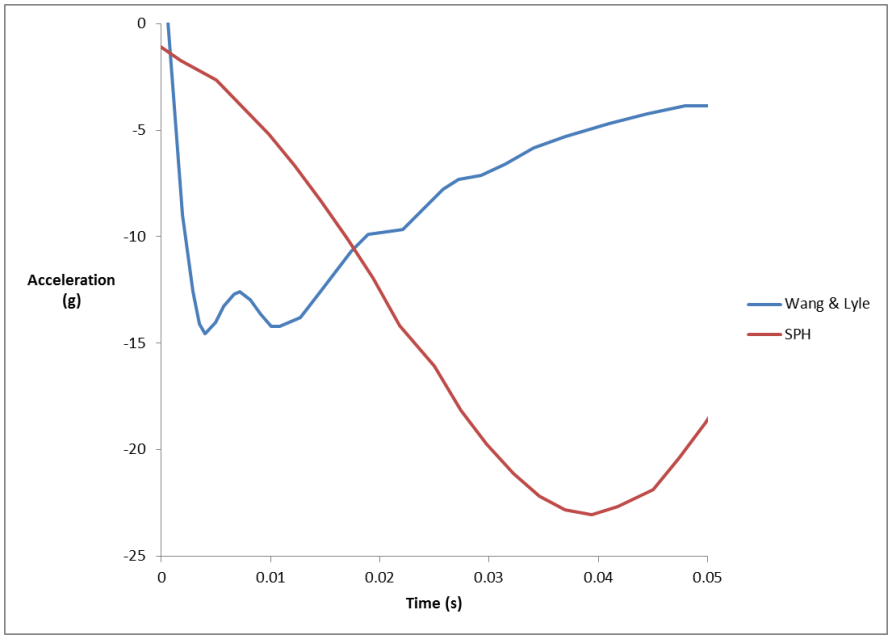

Figure *4-11 - Acceleration time history for sphere impact after impact at time zero*

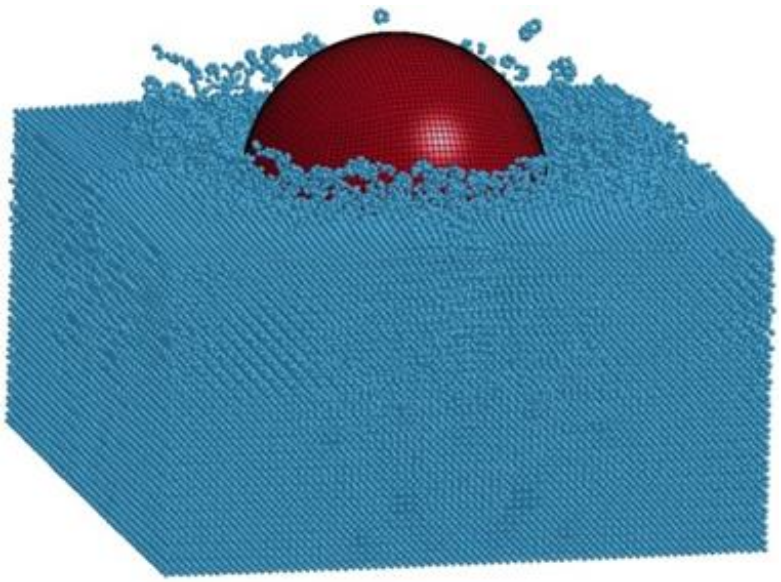

Figure *4-12 Model of the SPH and FE Parts after initial Impact*

4.5.3 Discussion

The promising results seen in the 2D experiments have not been reproduced in 3D and SPH does not provide a close match to the experiment. The reason for the poor accuracy is unknown and requires further investigation.

4.6 Underwater Blast Test

4.6.1 Introduction

The objective of this study is to demonstrate the capability of the coupled SPH-FE method to predict the structural response of a material subjected to loading from underwater blast, this requires the proper calculation of the high pressure gradients in the water as the blast propagates through the domain, and for contact forces to be properly resolved between the fluid and the plate, eventually this has potential to lead to more complex studies such as the modelling of composite sandwich panels subjected to blast [63]. Here we investigate the modelling of the explosive blast and how accurately the peak pressures can be approximated. An accurate prediction of the blast pressure and consequently the structural loads would allow the more complicated composite case to be considered.

4.6.2 2D Simulations

[64] gives the equation for peak pressure reached in an underwater explosion as a function of standoff distance and weight of the explosive charge, the equation is:

$$P = K\left(\frac{W^{1/3}}{R}\right)^{\alpha} \tag{4.7}$$

Where R is the standoff distance is metres and W is the weight of the explosive in kg. K and α are constants determined by the type of explosive, for TNT they are 52.4 and 1.13 respectively.

The explosion in SPH is simulated without modelling the charge directly and instead a large amount of internal energy is concentrated in a small number of particles resulting in a blast wave. The material is water and a Gruneisen equation of state is used to handle the shock wave. According to [65] the total energy of detonation for TNT is 7.403 KJ/cc. This is equivalent to 7403 J/cc = 7.403E+09 J/m^3.

The SPH explosion is simulated in 2D using 9800 particles in a 0.15mx0.15m domain with symmetry planes surrounding the box, the explosive charge is in the bottom left corner, in the case where only an initial energy is specified, it is the same particles that are used.

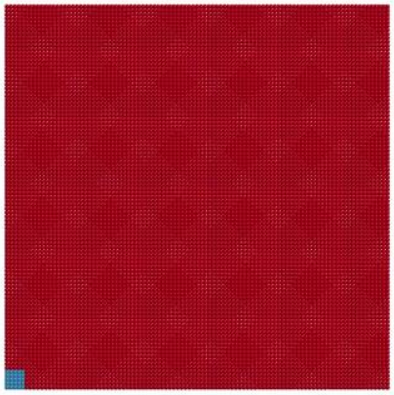

Figure *4-13 - SPH problem setup for 2D underwater blast problem*

The SPH Results are shown in Figure 4-14, the pressure value comes from the pressure interpolated around a point, and choosing the maximum pressure that occurs up to a given time, so since we are dealing with shocks some accuracy might be lost through the interpolation. Figure 4-14shows the blast simulated without directly modelling the charge and a standoff distance of up to 15cm, initial internal energy is 5.9E+09 J/m^3.

4.6.3 2D Results

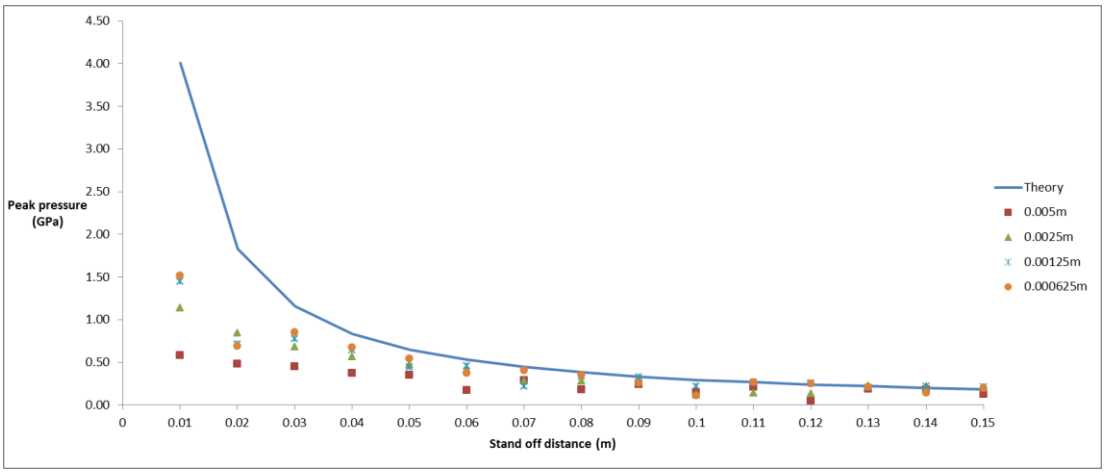

Figure *4-14 - Peak pressures plotted against standoff distance and compared with theoretical results from [64] for varying number of particles across the width of the domain*

4.6.4 Discussion

The peak pressures obtained in the 2D become more consistent with the theoretical results as the stand-off distance increases, this can be expected in this kind of simulation since the sharp rise in pressure immediately next to the blast location requires a much finer

resolution in order to resolve the peak pressure correctly, since the peak pressure are obtained through an SPH interpolation at the specific points, it is particularly difficult to capture the sharp gradient toward the peak. However this test does suggest that it is possible to predict peak pressures to a reasonable degree as long as the point of interest is not too close to the blast location.

4.6.5 3D Simulations

The problem is extended into 3 dimensions, the properties for the test are based on the experiment in [66], in which a steel plate is subjected to loading from underwater explosions and the central deflection of the steel plate is measured. The properties used to simulate the steel plate are given in table 4

Density	7800 kg/m3
Material model	Kinematic/Isotropic Elastic Plastic
Yield Stress	3.0E+08
Youngs Modulus	2.1E+11
Poissons ratio	0.3
Tangent Modulus	1.0E+08

Table 4 - Material Properties used in the Simulations

To simulate the blast in 3D, a domain was created with dimensions 25cm x 30cm x 30cm. This is smaller than the real domain size used in the experiment. The standoff distance remains 15cm. The water is modelled using SPH particles and this time a plate of steel is modelled using FE shells.

a) 150,000 SPH particles .7800 shell elements for the plate (spacing approx. 0.003m).
b) The blast is modelled by assigning a higher internal energy to a cube of 8 SPH particles, 15 cm way from the surface of the plate.
c) Gravity is applied to the water.

d) Contact between the plate and the water is via repulsive force.
e) Thickness of the steel plate is 0.004m
f) According to the experiment, the explosive used has an energy content of 1240 kcal/kg. This equals 5,188,160 J/kg. [66]
g) For this example the explosive quantity used is 0.005kg, therefore has an energy content of 25940.8 J.

In the SPH simulation the energy was assigned for each of the 8 particles as additional particle information, an energy content of 3242.6 J for each particle. The complete model set-up is shown in figure 4-15, where half the domain is transparent to show the centre of the blast location, figure 4-16, shows a typical response of the steel plate after the blast loading.

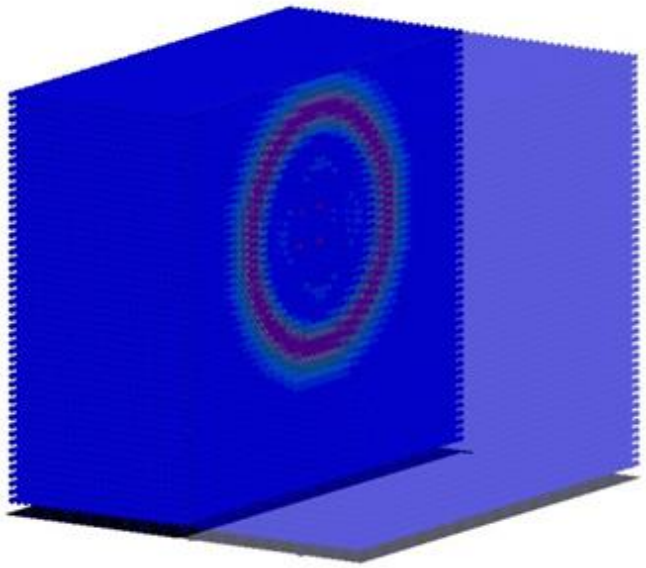

Figure *4-15 - Model Set-up for Underwater Blast, a Short Time after Detonation*

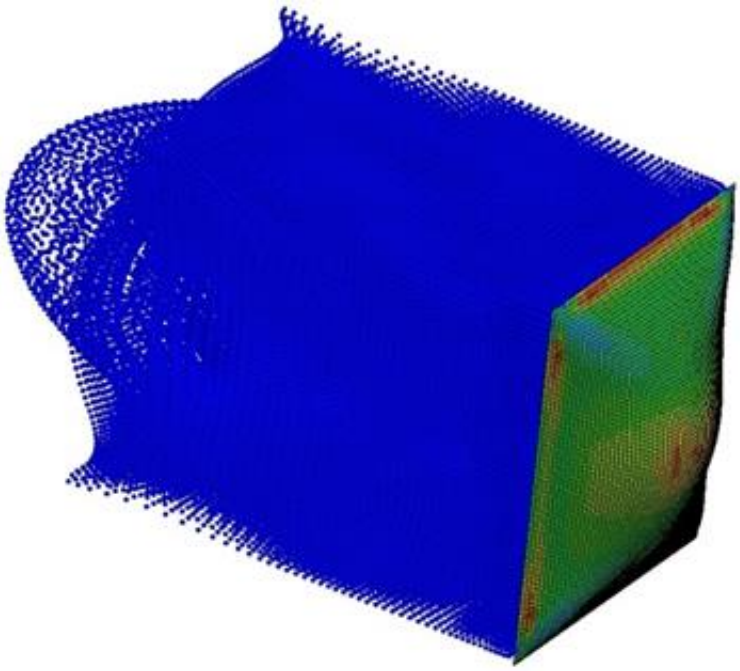

Figure *4-16 - Deformation of Steel Plate after Blast Loading*

4.6.6 Results

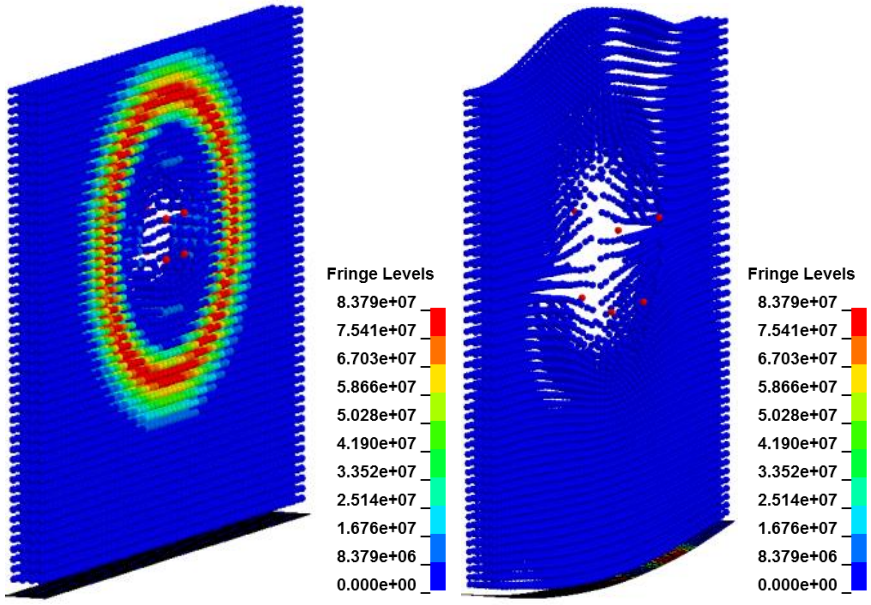

Figure *4-17 - The coupled problem, before (left) and after (right) deformation of the steel plate has occurred*

The experiment provides the deformation at the centre of the plate caused by the blast, see Table 5.

Explosive quantity (g)	Central deflection (mm)
5	12
10	23
15	27
20	32
30	42
40	50
50	58
60	65
70	72
80	rupture

Table 5 - Central Deflection of the Steel Plate for a Range of Explosive Quantities

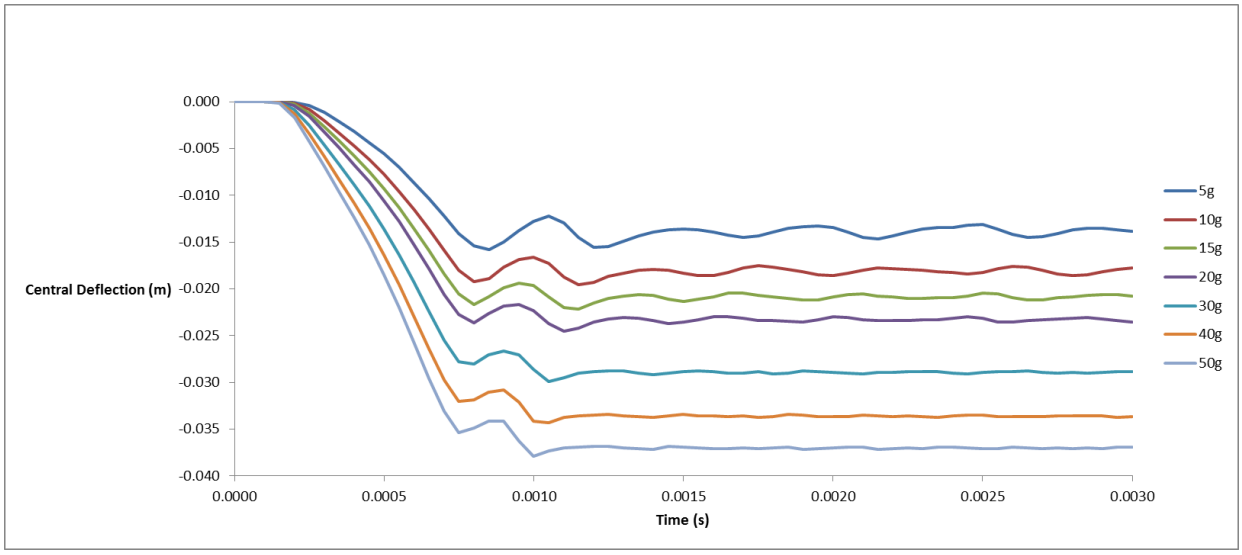

Figure *4-18 - Time history plot of the central deflection of the steel plate for various explosive quantities*

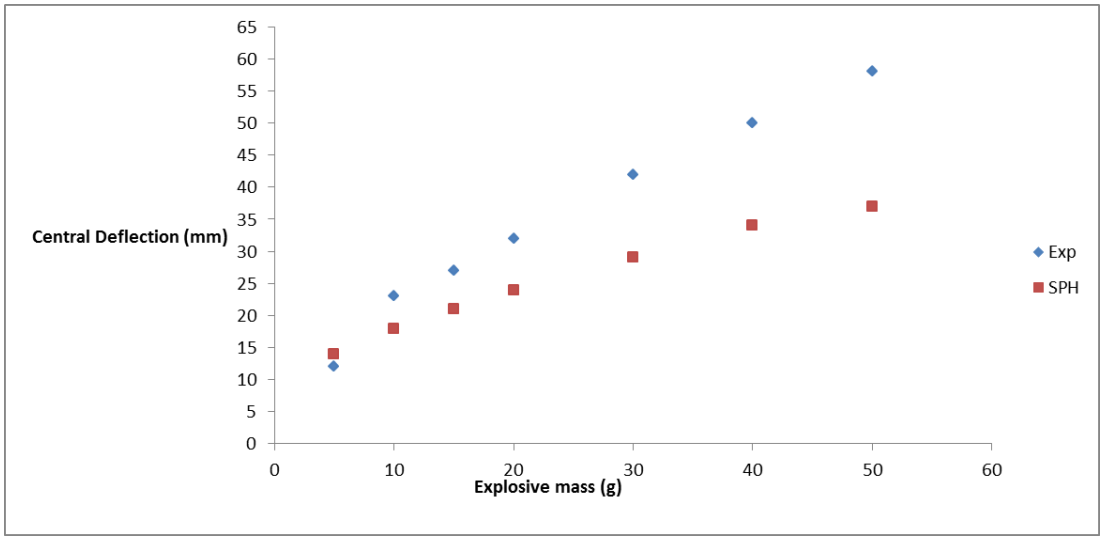

Figure *4-19 – Approximate central deflection of the steel plate for various explosive quantities*

4.6.7 Discussion

Figure 4-18 shows the time history plots of the central deflection of the plate, for various quantities of explosive, these central deflections are then plotted against the experimental result in figure 4-19. SPH tends to under predict the central deflection, which becomes more pronounced as the explosive quantity is increased, however the correct trend is seen and the results are encouraging. Further studies should look at a higher particle resolution in order to understand the convergence of the problem.

4.7 Turbulence Modelling

4.7.1 Introduction

So far the current capability of the SPH method has been demonstrated in this chapter through a series of test problems, the remaining objectives require an in depth knowledge of both the SPH method and the implementation at Cranfield University (MCM), therefore the remainder of this chapter focuses on the development of a relevant improvement to the MCM code in order to achieve the level of understanding required to address the rest of the objectives discussed in chapter one.

The implementation of a turbulence model is an obvious choice, having already been developed in SPH form but not currently part of the MCM code. Turbulence will always

come into the discussion of fluid motion and is considered a critical aspect of fluid modelling. Therefore it is considered that this project will provide an improvement to the code that may also be relevant for future applications.

Various turbulence models have been successfully implemented with SPH with good results including Monaghan [6] who devised a turbulence model specifically for SPH. The success of the particular turbulence model depends largely on the type of problem. For free-surface flows, López, Marivela and Garrote [67] used the $k-\varepsilon$ model to simulate the hydraulic jump problem, achieving good results but at a computation time that is almost doubled compared to that of basic SPH. Violeau and Issa [7] used a number of one and two equation models including $k-\varepsilon$, explicit algebraic Reynolds stress model (EARSM) and LES. Again satisfactory results were achieved for the collapse of a water column, the author of [7] advises that the standard $k-\varepsilon$ is appropriate for practical environmental and industrial applications, however also states that it may be inappropriate for very complex free-surface flows. It is also stated that LES can be very computationally expensive when used with SPH.

Another problem that has been investigated using the $k-\varepsilon$ turbulence model is that of the breaking wave [8] the results of which matched well with experimental data.

The conclusions made by the above authors imply that the $k-\varepsilon$ turbulence model is the best choice of model to implement in the MCM program. The $k-\varepsilon$ model has been shown to perform well in free shear problems [68]where the pressure gradients are small, making it a good choice of turbulence model for the MCM code, given that SPH is particularly useful for modelling free surface flows.The $k-\varepsilon$ has been well validated with SPH and also produces good results in many practical applications as well as being fairly simplistic, although it would be sensible to take into account the conclusions made by Violeau and Issa [7] when considering very complex free surface flows where the distortions are very large.

4.7.2 $k-\varepsilon$ Model and RANS Equations

This turbulence model is a "two equation" model, which means that two extra transport equations are introduced in order to represent the turbulent properties of the flow, which can then be used to close the RANS equations. In this case the new transported variables

are the turbulent kinetic energy k which determines the energy in the turbulence. The other quantity, ε determines the scale of the turbulence.

For a turbulent flow, the RANS equations separate the average and the fluctuating parts of the flow quantity, e.g. $\boldsymbol{v}$, by way of Reynolds decomposition:

$$v(\boldsymbol{x},\boldsymbol{t}) = \bar{v}(\boldsymbol{x},\boldsymbol{t}) + v'(\boldsymbol{x},t) \tag{4.8}$$

Where $\bar{v}$ represents the mean and the v' represents the fluctuation and $\boldsymbol{x} = (x, y, z)$

Starting with the incompressible momentum equation, without any body-force term

$$\boldsymbol{v}_t + \boldsymbol{v}\cdot\nabla\boldsymbol{v} = -\frac{1}{\rho}\nabla P + v\Delta\boldsymbol{v} \tag{4.9}$$

Substituting the velocity and pressure quantities with the sum of mean and fluctuating parts as in (1)

$$(\overline{\boldsymbol{v}} + \boldsymbol{v}')_t + (\overline{\boldsymbol{v}} + \boldsymbol{v}')\cdot\nabla(\overline{\boldsymbol{v}} + \boldsymbol{v}') = -\frac{1}{\rho}\nabla(\overline{\boldsymbol{P}} + \boldsymbol{P}') + v\Delta(\overline{\boldsymbol{v}} + \boldsymbol{v}') \tag{4.10}$$

Expanding the dot product terms

$$\begin{aligned}(\overline{\boldsymbol{v}} + \boldsymbol{v}')_t + \overline{\boldsymbol{v}}\cdot\nabla\overline{\boldsymbol{v}} + \overline{\boldsymbol{v}}\cdot\nabla\boldsymbol{v}' + \boldsymbol{v}'\cdot\nabla\overline{\boldsymbol{v}} + \boldsymbol{v}'\cdot\nabla\boldsymbol{v}' \\ = -\frac{1}{\rho}\nabla(\overline{\boldsymbol{P}} + \boldsymbol{P}') + v\Delta(\overline{\boldsymbol{v}} + \boldsymbol{v}')\end{aligned} \tag{4.11}$$

Then taking averages of all terms

$$\begin{aligned}\overline{(\overline{\boldsymbol{v}} + \boldsymbol{v}')_t} + \overline{\overline{\boldsymbol{v}}\cdot\nabla\overline{\boldsymbol{v}}} + \overline{\overline{\boldsymbol{v}}\cdot\nabla\boldsymbol{v}'} + \overline{\boldsymbol{v}'\cdot\nabla\overline{\boldsymbol{v}}} + \overline{\boldsymbol{v}'\cdot\nabla\boldsymbol{v}'} \\ = -\nabla\overline{(\overline{\boldsymbol{P}} + \boldsymbol{P}')} + v\Delta\overline{(\overline{\boldsymbol{v}} + \boldsymbol{v}')}\end{aligned} \tag{4.12}$$

Then using the following relations:

$$\overline{\overline{(\overline{\boldsymbol{v}}+\boldsymbol{v}')_t}} = \overline{(\overline{\boldsymbol{v}})} + \overline{\boldsymbol{v}_t{}'} \tag{4.13}$$

$$\overline{\overline{(\overline{\boldsymbol{v}})}} = \overline{\boldsymbol{v}} \tag{4.14}$$

$$\overline{\boldsymbol{v}_t{}'} = 0 \tag{4.15}$$

$$\overline{\overline{\boldsymbol{v}} \cdot \nabla \boldsymbol{v}'} = 0 \tag{4.16}$$

$$\overline{\boldsymbol{v}' \cdot \nabla \overline{\boldsymbol{v}}} = 0 \tag{4.17}$$

$$\overline{\overline{\boldsymbol{v}} \cdot \nabla \overline{\boldsymbol{v}}} = \overline{\boldsymbol{v}} \cdot \nabla \overline{\boldsymbol{v}} \tag{4.18}$$

The RANS momentum equation can finally be simplified to

$$\overline{\boldsymbol{v}}_{\boldsymbol{t}} + \overline{\boldsymbol{v}} \cdot \nabla \overline{\boldsymbol{v}} = -\frac{1}{\rho} \nabla \bar{P} + v \Delta \overline{\boldsymbol{v}} - \nabla \overline{\boldsymbol{v}' \boldsymbol{v}'} \tag{4.19}$$

Which also can be written as in Violeau and Issa, [7] as:

$$\frac{D\overline{\boldsymbol{v}}}{Dt} = -\frac{1}{\rho} \nabla \bar{P} + v \Delta \overline{\boldsymbol{v}} + \frac{1}{\rho} \nabla \cdot (\rho \boldsymbol{R}) \tag{4.20}$$

where ρ = density; t = time; $\mathbf{u}$ = velocity; P = pressure; $\mathbf{g}$ = gravitational acceleration; ν= kinematic viscosity of laminar flow and $\boldsymbol{R}$= Reynolds stress:

$$\boldsymbol{R} = \begin{pmatrix} \overline{\boldsymbol{v}_1{}'\boldsymbol{v}_1{}'} & \overline{\boldsymbol{v}_1{}'\boldsymbol{v}_2{}'} & \overline{\boldsymbol{v}_1{}'\boldsymbol{v}_3{}'} \\ \overline{\boldsymbol{v}_1{}'\boldsymbol{v}_2{}'} & \overline{\boldsymbol{v}_2{}'\boldsymbol{v}_2{}'} & \overline{\boldsymbol{v}_2{}'\boldsymbol{v}_3{}'} \\ \overline{\boldsymbol{v}_1{}'\boldsymbol{v}_3{}'} & \overline{\boldsymbol{v}_2{}'\boldsymbol{v}_3{}'} & \overline{\boldsymbol{v}_3{}'\boldsymbol{v}_3{}'} \end{pmatrix} \tag{4.21}$$

Assuming the Reynolds stress is modelled through the traditional Boussinesq eddy viscosity assumption.

$$R = \frac{2}{3}k\boldsymbol{I} - 2\nu_T S \tag{4.22}$$

Where R $= \frac{\overline{v'v'}}{2}$, S is the mean rate of strain and ν_T is the eddy viscosity.

The relationship between turbulent viscosity, turbulent kinetic energy, k and turbulent dissipation rate ε, is established such that:

$$\upsilon_T = c_d \frac{k^2}{\varepsilon} \tag{4.23}$$

The rate of change of k and ε is given by the following equations, governing the diffusion transport, and production of turbulent kinetic energy:

$$\frac{Dk}{Dt} = P - \varepsilon + \nabla \cdot \left[\left(\nu + \frac{\nu_T}{\sigma_k} \right) \nabla \mathrm{k} \right] \tag{4.24}$$

$$\frac{D\varepsilon}{Dt} = \nabla \cdot \left(\frac{\nu_T}{\sigma_\varepsilon} \nabla \varepsilon \right) + c_{1\varepsilon} \frac{\varepsilon}{k} P_k - c_{2\varepsilon} \frac{\varepsilon^2}{k} \tag{4.25}$$

$$P_k = \nu_T \left[2 \left(\frac{\partial u}{\partial x} \right)^2 + 2 \left(\frac{\partial v}{\partial y} \right)^2 + 2 \left(\frac{\partial u}{\partial x} + \frac{\partial v}{\partial y} \right)^2 \right] \tag{4.26}$$

Note that in (4.26), u and v now refer to the x and y components of the velocity vector.

4.7.3 SPH RANS Equations

Again, following Violeau and Issa, [7], the SPH equation for momentum in RANS form can be written as:

$$\frac{d\overline{\boldsymbol{v}}_a}{dt} = -\sum_b m_b \left(\frac{\bar{p}_a}{\rho_a^2} + \frac{\bar{p}_b}{\rho_b^2} - \frac{\mu_{Total,a} + \mu_{Total,b}}{\rho_a \rho_b} \frac{\overline{\boldsymbol{u}}_{ab}}{r_{ab}^2} \boldsymbol{r}_{ab} \cdot \right) \nabla_a W_{ab} \tag{4.27}$$

Where;

$$\mu_{Total,a} = \rho_a (\upsilon_a + \upsilon_{T,a})$$

$$\mu_{T,a} = \rho_a C_\mu \frac{k_a^2}{\varepsilon_a}$$

$$P = -\boldsymbol{R}:\boldsymbol{S} = -R_{ij} S_{ij}$$

$$P = \upsilon_T S^2$$

$$S = \sqrt{2\boldsymbol{S}:\boldsymbol{S}}$$

S being the scalar mean rate of strain.

The Reynolds averaged pressure, $\bar{p}$ can still be estimated from the usual equation of state. But k and ε will need to be calculated at each time step:

$$\frac{dk_a}{dt} = P_a - \varepsilon_a - \sum_b m_b \frac{\mu_{k,a} + \mu_{k,b}}{\rho_a \rho_b} \frac{k_{ab}}{r_{ab}^2} \boldsymbol{r}_{ab} \cdot \nabla_a W_{ab} \tag{4.28}$$

$$\frac{d\varepsilon_a}{dt} = \frac{\varepsilon_a}{k_a} (C_{\varepsilon,1} P_a - C_{\varepsilon,2} \varepsilon_a) + \sum_b m_b \frac{\mu_{\varepsilon,a} + \mu_{\varepsilon,b}}{\rho_a \rho_b} \frac{\varepsilon_{ab}}{r_{ab}^2} \boldsymbol{r}_{ab} \cdot \nabla_a W_{ab} \tag{4.29}$$

Where;

$$\mu_{k,a} = \mu_a + \frac{\mu_{T,a}}{\sigma_k} \tag{4.30}$$

$$\mu_{\varepsilon,a} = \mu_a + \frac{\mu_{T,a}}{\sigma_\varepsilon} \tag{4.31}$$

And $C_{\varepsilon,1}, C_{\varepsilon,2}, C_\mu, \sigma_\varepsilon, \sigma_k$ are constants and μ_a is the dynamic viscosity.

4.7.4 Implementation

The main changes to the procedure will be in the momentum equation, viscosity terms are evaluated between particles, for example averaged flow quantity $\overline{\boldsymbol{u}}_{ab}$ therefore changes will be made to the momentum equation.

Also only moving fluid particles will be considered capable of becoming turbulent, other particles will be evaluated in the normal way (basic SPH).

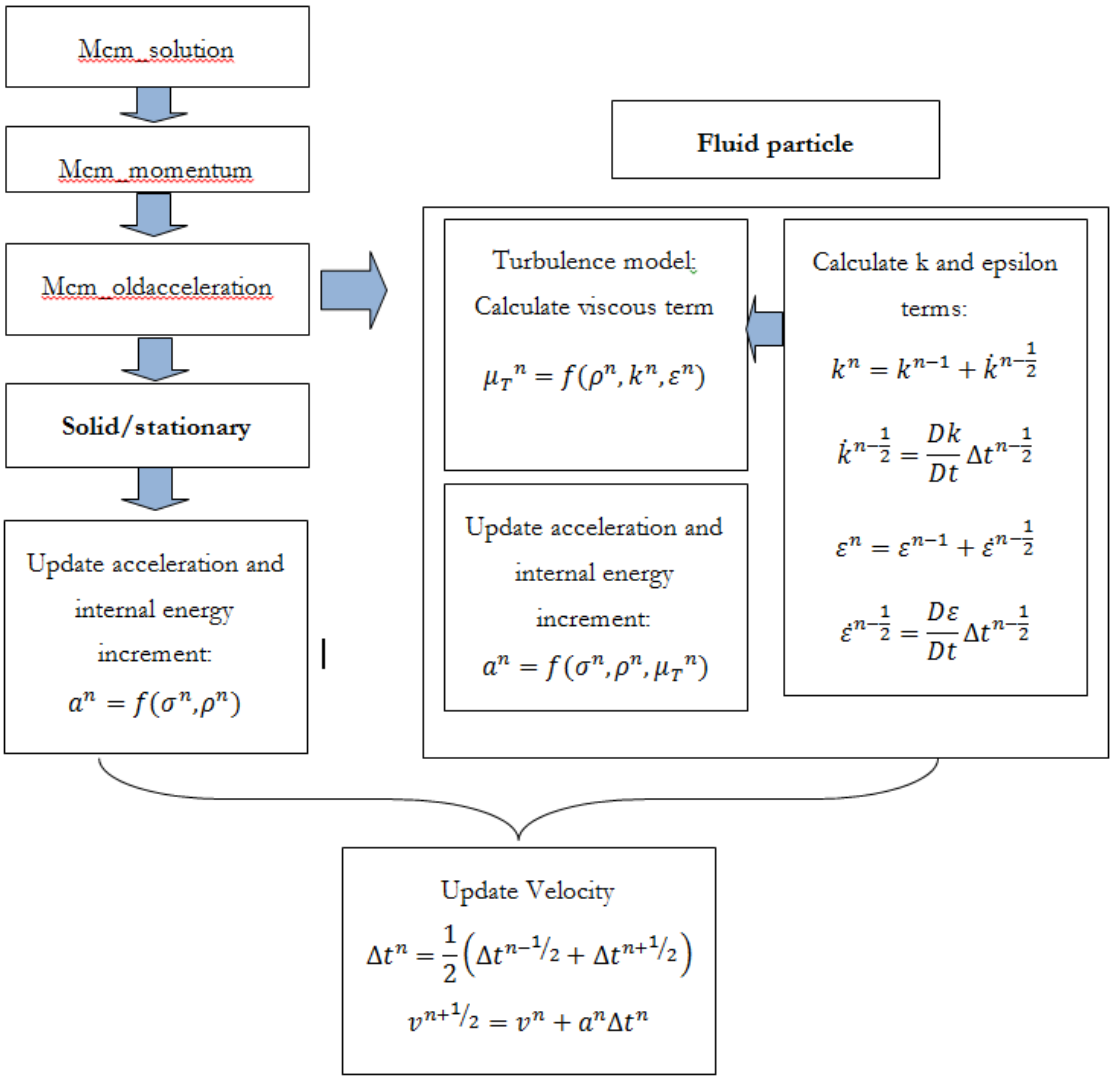

4.7.5 Verification

The aim here is to verify that the implementation of the turbulence model, this means that we must show with high confidence that the model is built properly is accordance with the mathematical specifications. Note that the concern is not yet to validate the model, i.e. to show that physically meaningful results are achievable.

The verification procedure should normally involve a thorough debugging of the code, some investigations performed in order to make this process easier involve comparison of some of the turbulent quantities with those from other accurate methods. Therefore it becomes easier to see where errors in the implementation are present. Some of these tests are presented below.

The test case used is that of a 2D dam-break problem, which involves a column of water which is suddenly released or exposed to gravity, the problem involves a complex free surface flow involving wave breaking and highly turbulent flow. The problem is well studied both experimentally and with CFD, a schematic of the problem is shown below. Other test problems have been used to validate and verify turbulence models such as the hydraulic jump problem with results widely available in literature [69], [70], [71]however many such problems require inflow or periodic boundary conditions which at the time of writing this thesis were not available in the MCM code. The dam break problem was chosen as an alternative test case which exhibits similar free shear flow, which as discussed in §4.7.1 provides a problem well suited to the $k-\varepsilon$ model.

To model this problem in SPH, symmetry planes are used to model the solid walls and the water column is made up of 10,000 SPH particles with a smoothing length of 1.3 times the particle distance, the density of the water is assumed to be 1000kg/m^3. The Murnagan equation of state is used [72] and the fluid is considered weakly compressible.

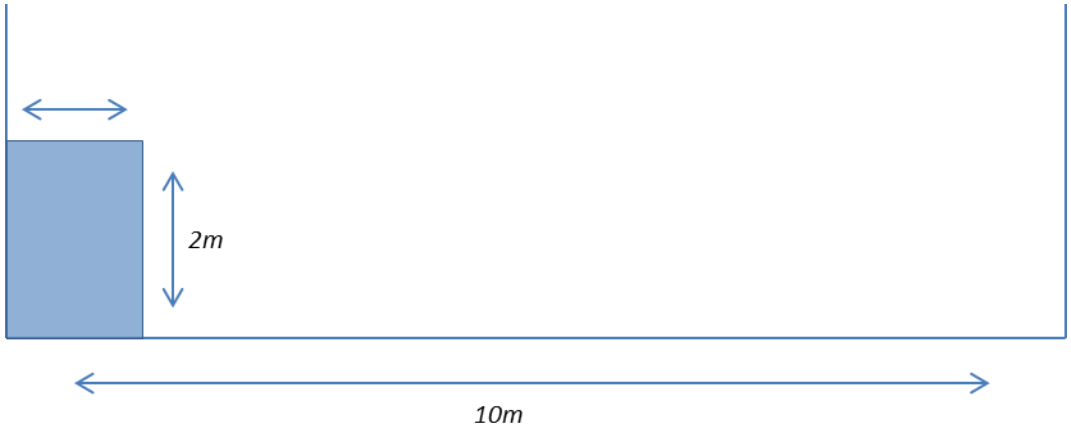

Figure *4-20 - 2D Dam-break setup*

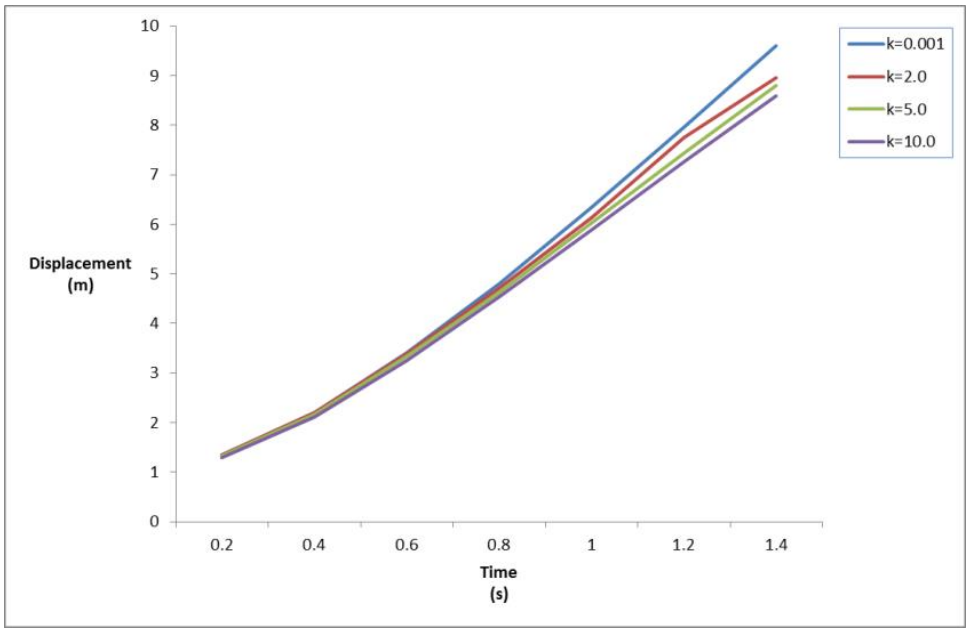

Figure *4-21 -Position of the wave front for different initial conditions for turbulent kinetic energy – k*

A simple comparison of the effect that the initial conditions have on the speed at which the column of water collapses can be seen in Figure 4-21. If the initial value of turbulent kinetic energy is increased, then this has the effect of slowing the progression of the water, the measurement here is taken at the position of the maximum horizontal displacement of the wave, i.e. the position of the dotted line in Figure 4-22. The effect of the turbulence model on the free surface can be seen in Figure 4-24.

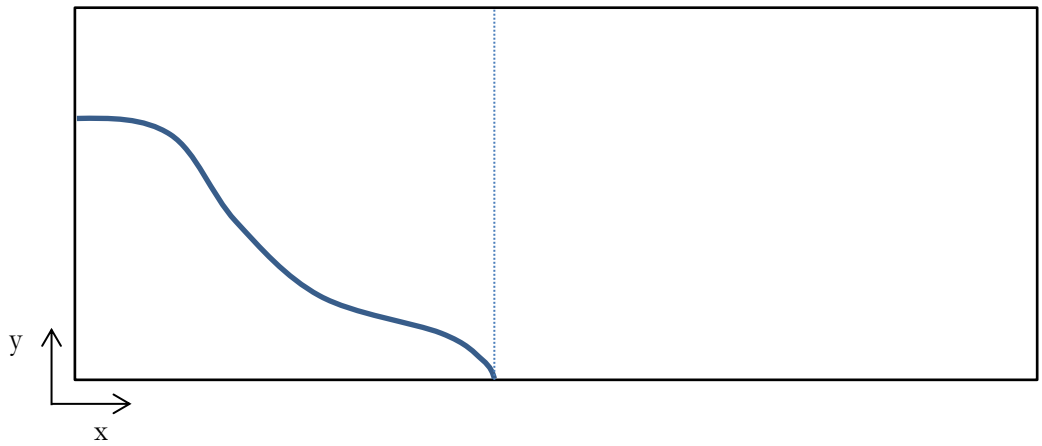

Figure *4-22 Schematic showing the position of the wave front for the dam break test case*

Although the initial values for k are not necessarily providing physically meaningful results, the test is only to see the effect on the simulation, however this effect can be interpreted as follows; the turbulent viscosity is directly dependant on the value of k. Therefore a higher turbulent viscosity will slow the flow down, mimicking the effect of a higher viscosity close to the wall.

This first simple test shows that the turbulence model is having the correct effect on the flow, however we wish to further increase confidence in the mathematical soundness of the implementation. Next an investigation was carried out which compared the turbulent values directly with those from an alternative method, namely volume of fluid. This method is considered to be accurate when used for a transient fluid problem. Therefore if the turbulence model in the SPH code can be seen to produce the same effect, then we can be sure that the implementation is correct.

The dam-break problem was solved using the volume of fluid method in Fluent, the dimensions of the domain were the same as in the SPH model, The Fluent model is assumed to provide a realistic solution to the dambreak problem. Similar problems have been modelled in Fluent and validated, including using the volume of fluid method coupled with the k epsilon turbulence model [73].

First, however it is important to understand the differences between the two methods in order to know whether it would be reasonable to expect identical results. The most fundamental difference between the two methods is that the volume of fluid method (VOF) belongs to the class of Eulerian method characterised by a fixed grid. SPH however

as discussed in previous section is a mesh-less method, therefore to compare the two methods is difficult, in particular it is difficult to identify a particular point.

With this being said, although it may be unreasonable to expect identical results, the trend at least should be similar, this way we can see if the turbulence model is acting as it should. We can expect turbulent kinetic energy to be dissipated slowly as the flow slows down after the initial effect of the dam breaking, also a sharp increase should be seen after the fluids impact with the wall.

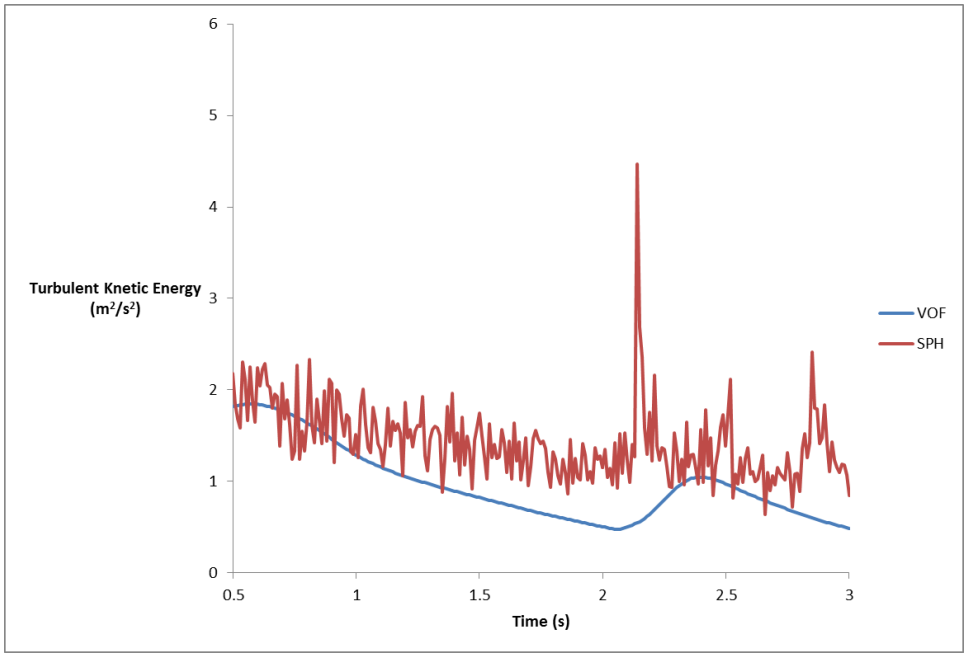

Figure *4-23 - Comparison of SPH and Volume of Fluid method, time history of turbulent kinetic energy at a fixed point in the domain*

Figure 4-23 shows a comparison between an SPH simulation and a solution obtained using the volume of fluid method in Fluent, in this test a point was chosen just above the floor at y = 0.1 in the centre of the box (x=2) here the values for turbulent kinetic energy were tracked through time. The aim here is to make a quantitative verification of the turbulence model, however it is important to note the difficulties in making such a comparison between two different methods.

The main problems lie in choosing the same point for the interpolation in both types of simulation, the VOF method taking an Eulerian approach and SPH, Lagrangian. Also since

the flow would be slightly different in each simulation is it impossible to say that we are tracking the same point of the flow.

Nevertheless, despite these issues it is encouraging to see that the slope of the SPH approximations fit to a reasonable extent with that of the VOF results. The SPH results to exhibit a lot of noise (which is expected in SPH simulations) and greatly overestimate the peak in kinetic energy seen at around 2.1 seconds, although overall it can be seen that the two simulations behave in roughly the same manner.

One important point to note when analysing these results is the noisiness that can be seen in the SPH solution, in particular the spike in turbulent kinetic energy at around 2 seconds, this could potentially be caused by interpolation errors at the particular point that was measured, which could potentially be large due to the highly non-uniform particle distribution at this point in the calculated due to the violent crashing of the wave after impact with the wall. This 'noise' is something that is typical in SPH solutions and the turbulence model is not the cause, possible fixes such as XSPH can be used to smooth the solution if necessary.

A qualitative comparison is shown in Figure 4-24 and **Error! Reference source not found.** which shows significant breakup of the particles in the conventional SPH case. The similarities between the VOF model and the $k-\varepsilon$ SPH model are clear, and confirm that the addition of the turbulence model to the SPH code does produce improved results.

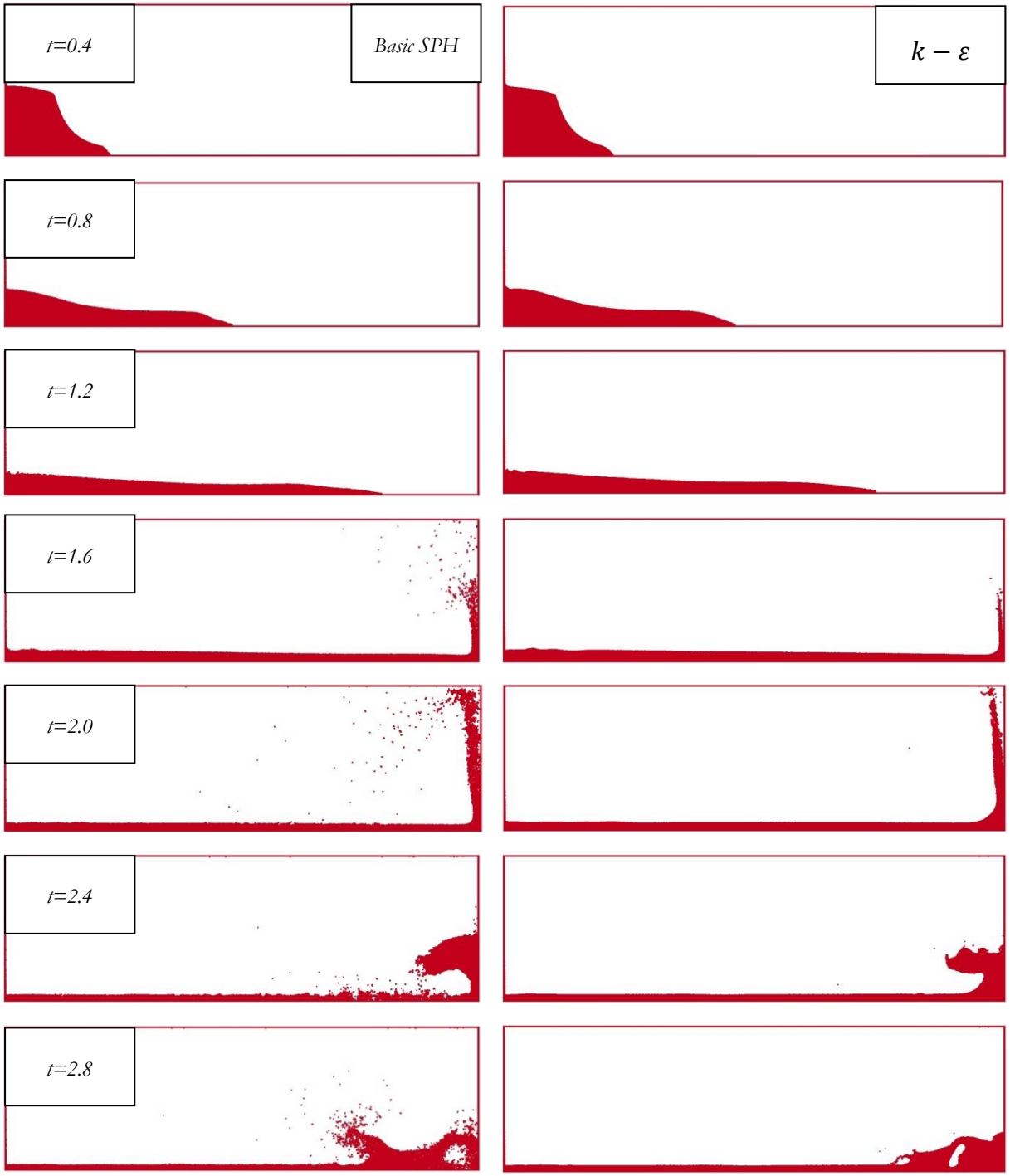

Figure *4-24 – Effect of turbulence on the dam-break problem, Basic SPH vs. $k-\varepsilon$ SPH*

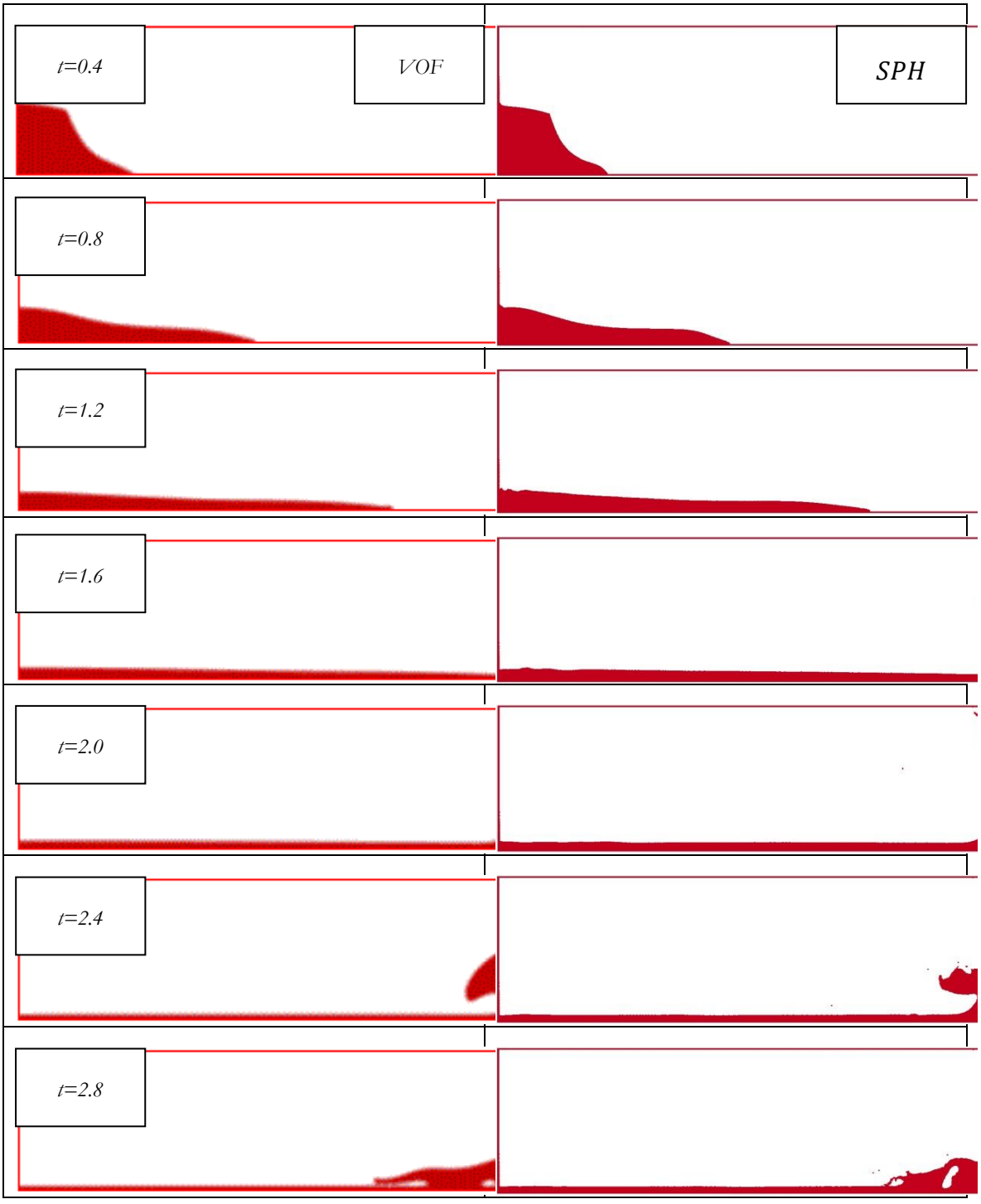

Figure 4-25 *Effect of turbulence on the dam-break problem, VOF (Fluent) vs.* $k-\varepsilon$ *SPH*

4.7.6 Discussion

An important and relevant improvement is implemented in an SPH framework, serving to build an in depth knowledge of the SPH method and the MCM code. The turbulence model is implemented and tested for the dam-break problem, providing results that are consistent with the presence of turbulence, the model is verified against results from FLUENT using the volume of fluid method, showing the same trends in the magnitude of the turbulent kinetic energy, although the SPH results show much more noise, which is expected from the method and is not due to the turbulence model.

4.8 Summary of Chapter Four

The current capability of the SPH method as a solution to engineering problems has been demonstrated in a number of test cases which show how the SPH method can be coupled with FEM for a full fluid structure interaction solver. Furthermore, a relevant improvement to the MCM code has been implemented and tested allowing wider class of problem to be investigated.

5 Modelling Lateral Contact Forces in SPH

5.1 Introduction

Real world problems in engineering will more often than not involve the interaction between two or more different materials or objects, this could be a solid material interacting with a fluid such as a pipe flow scenario, or two solid materials interacting such as in metal forging or machining. It is clear therefore that the ability to model the forces that develop between different materials is an important part of any engineering analysis code.

Previous work at Cranfield University [74] [15] [75] led to the development of a contact algorithm which resolves the forces between two SPH materials, this SPH-SPH contact algorithm is fundamental to the coupled approach which allows contact forces to be resolved between FE and SPH materials, by allowing the SPH particle to interact with all the FE nodes in its support radius, meaning the SPH particle spacing can be larger than the FE spacing between nodes, which is not the case for previous contact algorithms using surface to surface type contact.

The SPH-SPH contact algorithm as it stands only calculates the normal force between two bodies and does not account for lateral forces, some lateral forces do develop since the algorithm is dependent on the relative particle spacing of the two surfaces, this erroneous force should tend to zero as the spacing is refined.

The calculation of lateral forces between materials allows for a wider class of problem to be solved, for example high speed fluid flow produces shear forces against the wall, and strong frictional forces develop in machining applications.

The question is raised as to whether the contact algorithm currently implemented in MCM [15], is also suitable for resolving lateral forces between materials based on their relative velocities and coupling with a FE structural model. The development of a contact algorithm for the modelling of friction forces is identified as an appropriate method for answering this question.

5.2 A Penalty Stiffness Contact Algorithm

SPH is commonly coupled with FEM to allow reaction forces to be resolved between fluid and structure. [76], [77] and has been applied to problems such as high velocity impact [78] [79], as well as bird-strike [80] and aircraft ditching [81]. The foundation for the contact algorithm developed at Cranfield university [82], comes from first resolving contact between two SPH bodies [74] [15] [83]. In this work a penalty stiffness approach (in which contact is represented by linear springs between particles. Therefore stiffness here is referring to spring stiffness) is modified [15] to allow for friction forces, which to date is not found in any of the literature. The method remains the same in the calculation of interpenetration and of the normal contact force between two surfaces, once the contact force is calculated it is then rotation into the tangential plane and scaled according to a friction force algorithm. In this work the method is verified in 2D and then used to investigate a more complex and challenging 3D problem on steel forging.

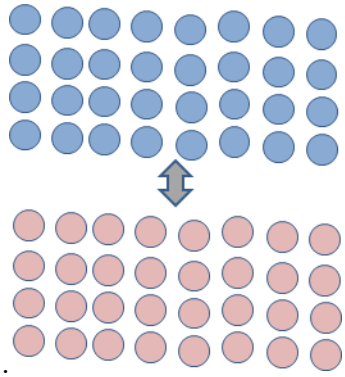

Figure *5-1 - Contact forces between two SPH bodies*

Contact between two bodies in SPH has received significant attention in recent years and was first addressed properly through the use of a penalty force to enforce contact conditions between materials [74] [75] , Figure 5-1. This formulation worked in 1D and 2D, although zero energy modes were often excited during impact. Later by the same authors, a frictionless contact algorithm was developed [15], whereby contact was imposed through the use of a contact potential when detected.

The latter approach is based on the repulsive force developed by Monaghan [84] and is the method used throughout this chapter for materials in contact; for a full derivation of the

contact force see [85]. The fact that a body force can be described as the gradient of a potential [86] is the basis for this type of contact force and is applied in the same way.

5.3 A Friction - Contact Algorithm

This contact force has successful been applied in SPH but at present does not account for frictional forces between materials. The direction of the friction force is defined as the being on the plane normal to the resultant contact force vector, and in a direction opposite from the relative velocity of the two materials.

The direction of the frictional force can be calculated as follows given the resultant contact force vector and a vector of relative velocity $f_{contact}$ and v_{AB}. The direction of friction is found by taking the projection of the relative velocity onto the plane that is orthogonal to the contact force (see Figure 5-2). This can be done by removing the part of the velocity vector that is orthogonal to the plane.

The orthogonal vector to the plane is simply $f_{contact}$ which is known, the component of v_{AB} which lies in the direction of $f_{contact}$ is

$$\frac{f_c(f_c \cdot v_{AB})}{\|f_c\|} \tag{5.1}$$

This can then be subtracted from v_{AB} to give the direction of the frictional force

$$v_{AB} - \frac{f_c(f_c \cdot v_{AB})}{\|f_c\|} \tag{5.2}$$

This can be rearranged slightly to give a more convenient form, which is called the triple cross product

$$v_{AB}\|f_c\| - f_c(f_c \cdot v_{AB}) = v_{AB}(f_c \cdot f_c) - f_c(f_c \cdot v_{AB}) = f_c \times (f_c \times v_{AB}) \tag{5.3}$$

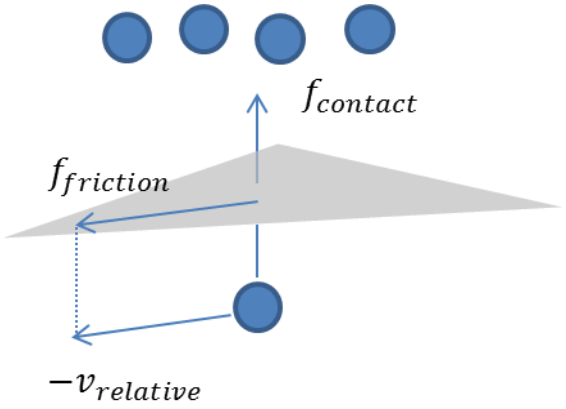

Figure *5-2 Plane tangential to normal contact force between two SPH bodies*

The calculation to find the direction of the tangential force, i.e. orthogonal to the normal force and opposite to the direction of relative motion of the two bodies, is:

$$\frac{f_c \times (f_c \times v_r)}{\|v_r\|} = \frac{f_c(f_c \cdot v_r) - v_r(f_c \cdot f_c)}{\|v_r\|} \qquad (5.4)$$

Where f_c is the normal force and v_r is the relative velocity vector, and $\|v_r\|$ is the magnitude of the relative velocity vector.

5.4 Implementation

The use of friction models in solid mechanics is well understood and a number of friction models have been developed with varying complexity, many FEM friction models are based on the Coulomb formulation.

A friction model must have the capability to resolve friction forces of two bodies in relative motion as well as when there is no relative motion, therefore two coefficients of friction are defined;

The static coefficient of friction – The coefficient of friction at rest, governing the force required for relative motion to occur.

The coefficient of kinetic friction – governs the force generated between two bodies in relative motion.

In practice the coefficient of friction at rest is often higher than that of kinetic friction; however for simplicity the same value is used in both cases in the SPH model, choosing the

same parameters in the LS-DYNA models ensures consistency between the problems being tested.

This method is adopted from the LS-DYNA approach, it prevents a frictional force being applied that would cause the body to begin moving when it should remain still due to static friction.

5.4.1 LS-DYNA Friction Model

As stated above the LS-DYNA friction model is based on a Coulomb formulation, which is well understood and used widely in numerical codes, it will therefore form a basis for the SPH model and allow tests to be run against FE models to compare the way in which the models work.

The LS-DYNA friction model is described by the following steps:

1. Firstly the yield force is calculated

$$F_y = \mu |f_n|$$

   Where F_y is the yield force, μ is the coefficient of friction and f_n is the normal contact force, the physical meaning of this is the maximum force that can develop between the two surfaces before slippage occurs.

2. Next the incremental movement of the slave node is calculated.

$$\Delta e = r^{n+1}(\xi_c^{n+1}, \eta_c^{n+1}) - r^{n+1}(\xi_c^{n}, \eta_c^{n})$$

3. Where Δe is the incremental movement, $\left(\xi_c\ , \eta_c\ \right)$ are the coordinates of the slave node at the contact point at time n or $n+1$ and r is the displacement.

4. The trial force is then updated

$$f^* = f^n - k\Delta e$$

   Where k is the interface stiffness, the term $k\Delta e$ is the force required to produce the incremental movement Δe, therefore f^* now represents the force required to bring the relative movement to rest over a single time-step.

5. The friction force is then updated for the next time-step

$$f^{n+1} = f^* \text{ if } |f^*| \leq F_y$$

$$f^{n+1} = \frac{F_y f^*}{|f^*|} \text{ if } |f^*| > F_y$$

This step prevents slippage occurring in the wrong direction, and accounts for the frictional forces which occur when the objects are at rest.

5.4.2 SPH Implementation

The SPH implementation follows the same methodology, and is equivalent to the LS-DYNA model, since the mass is assumed to be constant the acceleration is used rather than the force, this then allows the acceleration to be updated after the contribution from the normal force has been applied. The only other difference is in step 2, which replaces steps 2 and 3 in the LS-DYNA implementation, but has the same physical meaning.

1. Calculate the yield force

   $A_y = \mu |a_n|$

2. The trial force is calculated, the relative velocity in the direction of slippage (i.e. perpendicular to the normal force and in the direction of the frictional force) is represented by the term $v_r \cdot a^n$

   Dividing this term by the time-step results in the acceleration that will bring the relative motion to zero over that time-step.

   $$a^* = \frac{v_r \cdot a^n}{\Delta t}$$

3. The friction force is then updated for the next time-step

   $a^{n+1} = a^* \text{ if } |a^*| \leq A_y$

   $a^{n+1} = \frac{A_y a^*}{|a^*|} \text{ if } |a^*| > A_y a^{n+1} = \frac{A_y a^*}{|a^*|} \text{ if } |a^*| > A_y$

5.5 Numerical Results

To test the friction model the total Lagrange formulation is chosen for the SPH solver, the total Lagrange formulation is discussed in chapter three. This choice reduces uncertainties

in the SPH results, since the method is stable and well understood, see the discussion on stability of the Eulerian method in chapter three. Therefore conclusions can be made purely on the validity of the friction model and whether it correctly mimics the behaviour of the LS-DYNA implementation.

Two test cases are identified; the first is a 2D example which demonstrates how the friction model works for two bodies at rest, in the transition to relative motion.

The second case is a 3D metal forging problem, which is a complex real world problem in which strong frictional forces develop between the machining tools and a metal billet.

5.5.1 2D Block Sliding on an Flat Plane

To test the friction model, a simple problem in 2D is modelled and compared against an analytical solution. A block is placed at rest on a flat plane, which is then inclined gradually over time. This is a suitable problem to examine the transition between the frictional forces produced between the two bodies at rest and in relative motion, since the block remains at rest until the incline on the plane reaches a critical angle at which time the block begins to slide. The velocity of the block can be recorded and compared with the analytical solution

For a block starting at rest on a flat plate which is inclined from 0 to 45 degrees over a period of one second. For friction coefficients ranging from 0 (frictionless) to 1, the analytical functions for displacement, velocity and acceleration are plotted in Figure 5-4 - Figure 5-6. The dotted line indicates the angle at which the block begins to slide. The same coefficient of friction is used for both the static and the dynamic regimes. The schematic is shown in Figure 5-3

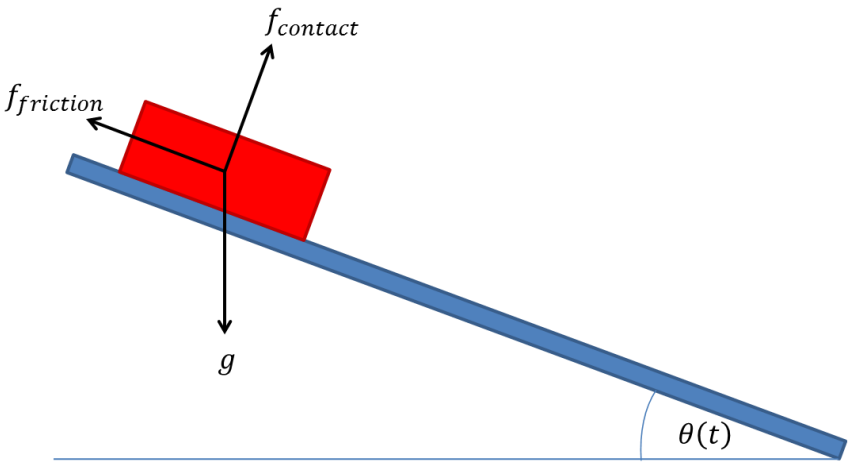

Figure *5-3 - Sliding block on an inclined plane*

The angle of the incline changes linearly with time, the normal component of the acceleration can be expressed as in (5.5), noting than a linear increase in the angle does not equate to a linear acceleration.

$$9.81 \cdot cos\big(\theta(t)\big) - 9.81 \cdot \mu \cdot cos\big(\theta(t)\big) \tag{5.5}$$

The velocity at a particular angle of inclination can then be written directly by integrating the expression for acceleration between an angle of zero and the angle of interest.

$$\begin{aligned} &\int_0^{\theta_0} \left[9.81 \cdot cos\big(\theta(t)\big) - 9.81 \cdot \mu \cdot cos\big(\theta(t)\big)\right] d\theta \\ &\qquad = \left(-9.81 \cdot sin\big(\theta(t)\big) + 9.81 \cdot \mu \cdot sin\big(\theta(t)\big) + C\right)\Big|_0^{\theta_0} \\ &\qquad = \left(-9.81 \cdot sin\big(\theta(t)\big) + 9.81 \cdot \mu \cdot sin\big(\theta(t)\big)\right) \end{aligned} \tag{5.6}$$

The angle of friction at rest (i.e. the angle which when exceeded, causes the block to slip and relative motion to develop between the block and the plate) can be found by equating the normal force and the frictional force:

$$9.81 \cdot cos\big(\theta(t)\big) = 9.81 \cdot \mu \cdot sin\big(\theta(t)\big) \quad (5.7)$$

$$tan^{-1}(\mu) = \theta_s \quad (5.8)$$

Which shows the angle at rest is only dependant on the coefficient of friction.

This shows that for a friction coefficient of one the angle of friction at rest is 45 degrees and hence the line remains flat in Figure 5-4 to Figure 5-6.

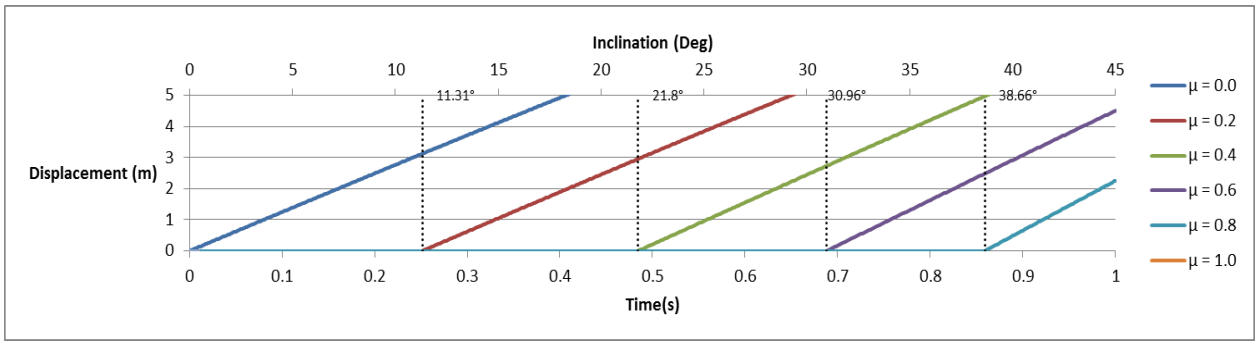

Figure *5-4 – Analytic result for displacement vs. time for a range of friction co-efficients, slippage angle shown as dotted line*

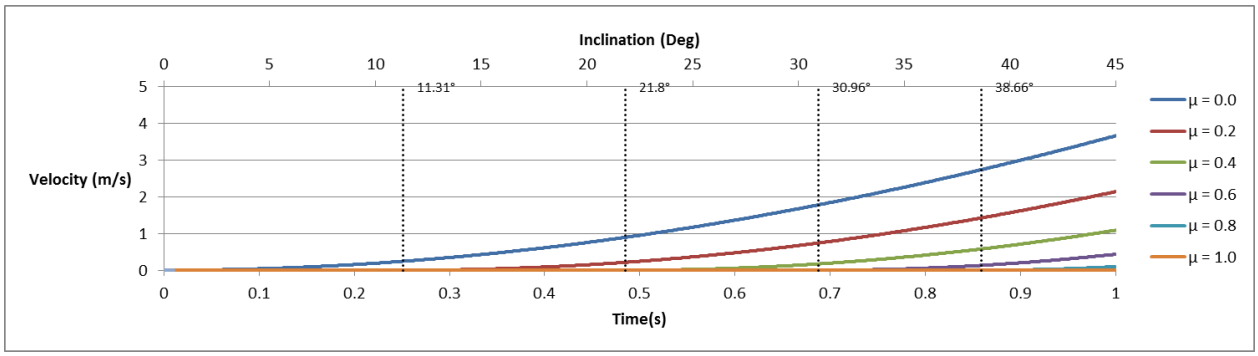

Figure *5-5 - Analytic result for velocity vs. time for a range of friction co-efficients, slippage angle shown as dotted line*

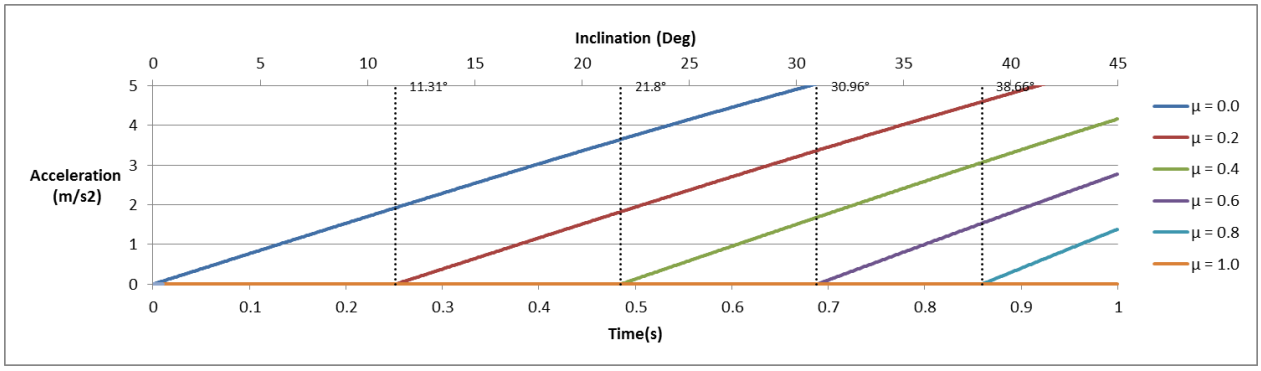

Figure 5-6 - *Analytic result for acceleration vs. time for a range of friction co-efficients, slippage angle shown as dotted line*

5.5.2 Results

The slipping block is performed in SPH with the block and the plate defined as the separate materials, the block is essentially rigid. The numerical model is made up of a flat plate and a smaller block, the block and plate are both made up of SPH particles and use the same particle spacing. The tilting of the plate is simulated by applying a body force to the block which changes over time; displacement boundary conditions are applied to the plate to prevent any movement. The thickness of the plate is made up of three rows of SPH particles which ensure that the neighbourhood of contact particles is full; therefore the thickness of the plate varies with particle spacing. The test properties are described in table 6 the material properties are identical for the block and the plate.

Density	7800 kg/m3
Particle spacing	0.005m, 0.0025m, 0.00125m, 0.000625m
Smoothing length	0.00650m, 0.00325m, 0.001625m, 0.0008125m
Youngs Modulus	2.1E+11
Poissons ratio	0.3
Length of Plate	0.5m
Formulation	Total Lagrange

Table 6 - Properties for the Numerical Tests for Friction

A load curve is applied to the block which mimics the tilting of the plate from flat to 45 degrees over the period of 1 seconds, the acceleration in the horizontal and vertical direction is shown in figure 5-7 and figure 5-8.

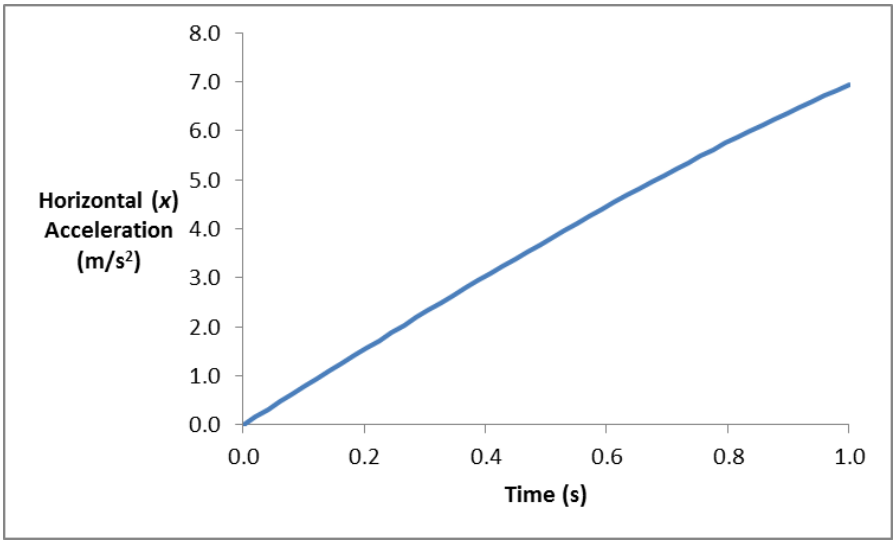

Figure *5-7 Load Curve for Horizontal Component of Acceleration*

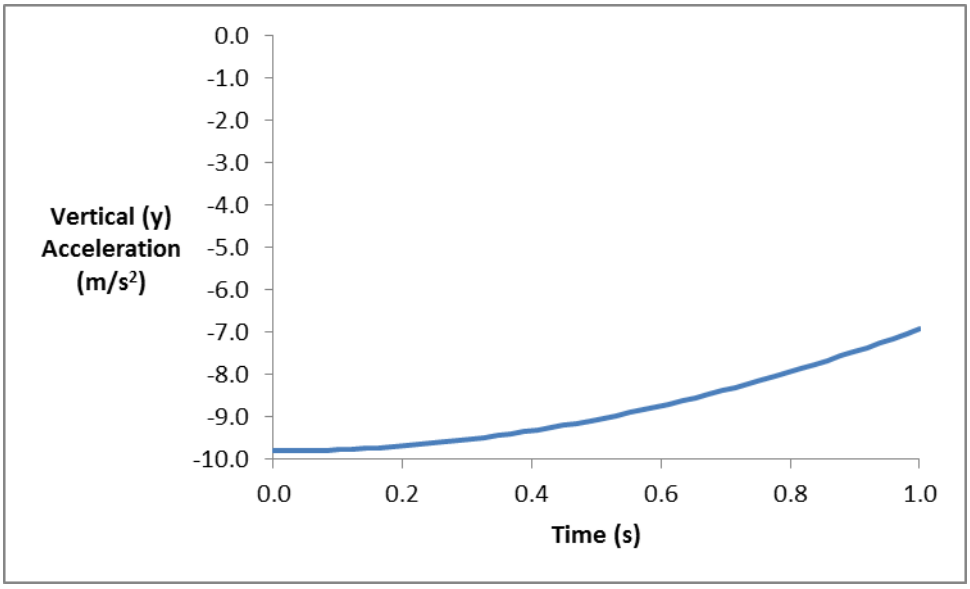

Figure *5-8 Load curve for Vertical Component of Acceleration*

The most straightforward comparison can be made by comparing the velocity of the block to the analytical solution. The velocity is calculated from the total momentum of all particles that make up the block. The time at which slippage should occur is displayed as a dotted line in the figure 5-10 to figure 5-13.

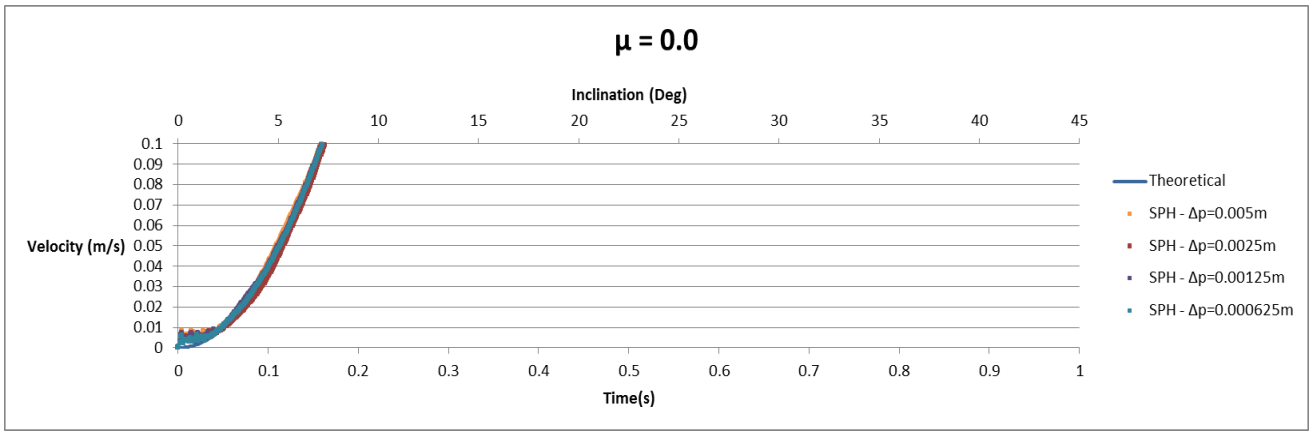

Figure *5-9 – SPH vs. Analytical velocity for various particle spacings for* $\mu = 0$

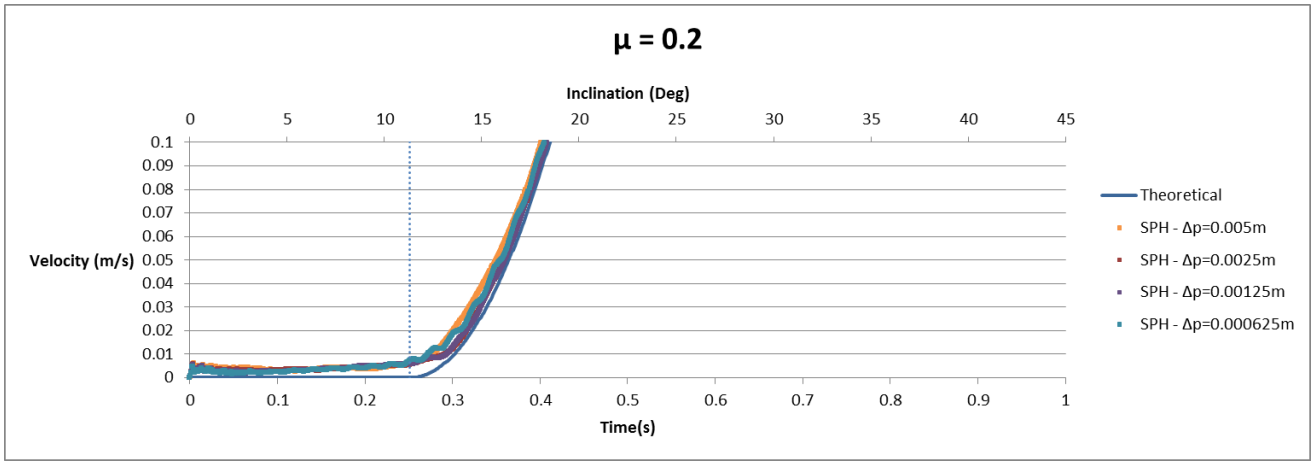

Figure *5-10 - SPH vs. Analytical velocity for various particle spacings for* $\mu = 0.2$

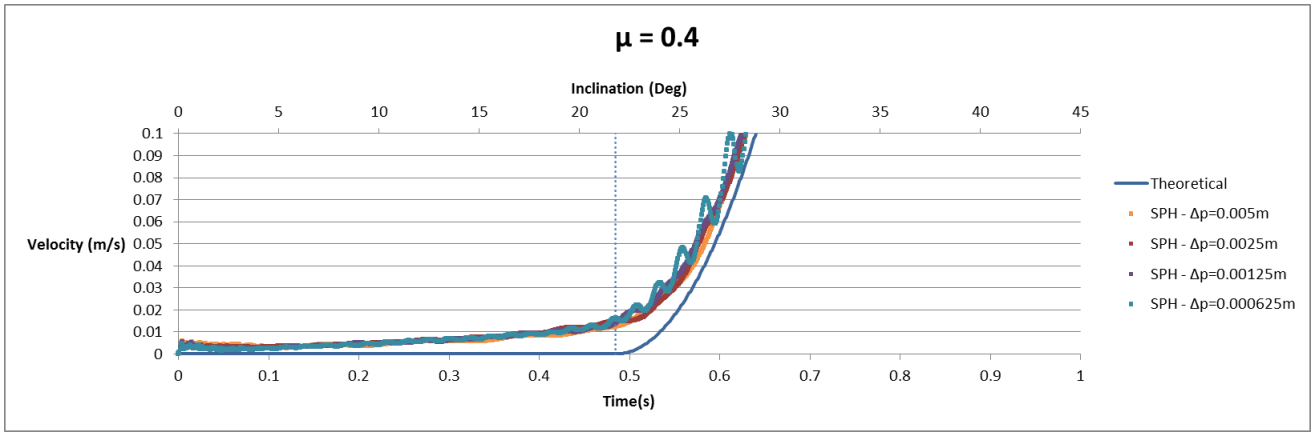

Figure *5-11 - SPH vs. Analytical velocity for various particle spacings for* $\mu = 0.4$

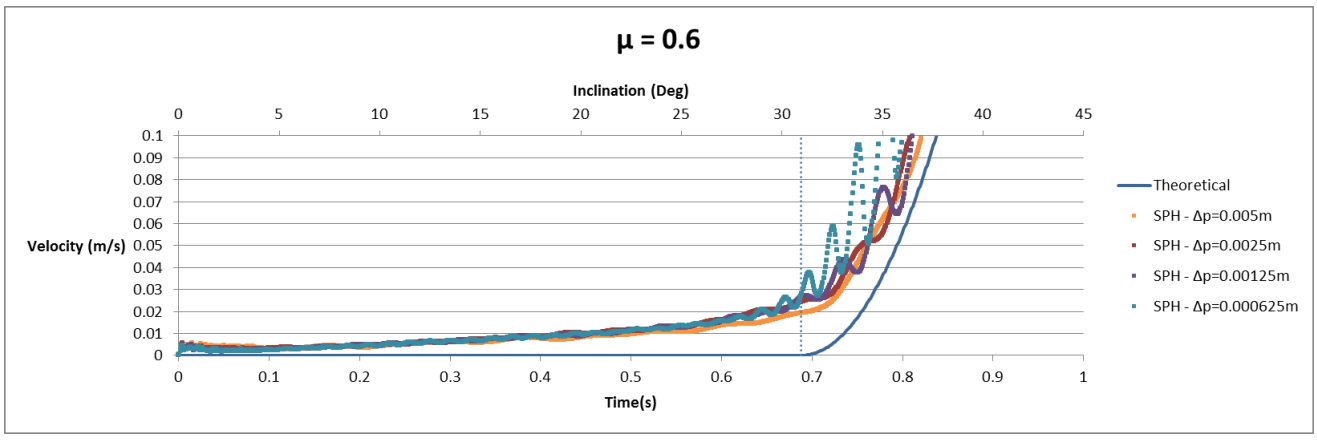

Figure *5-12 - SPH vs. Analytical velocity for various particle spacings for* $\mu = 0.6$

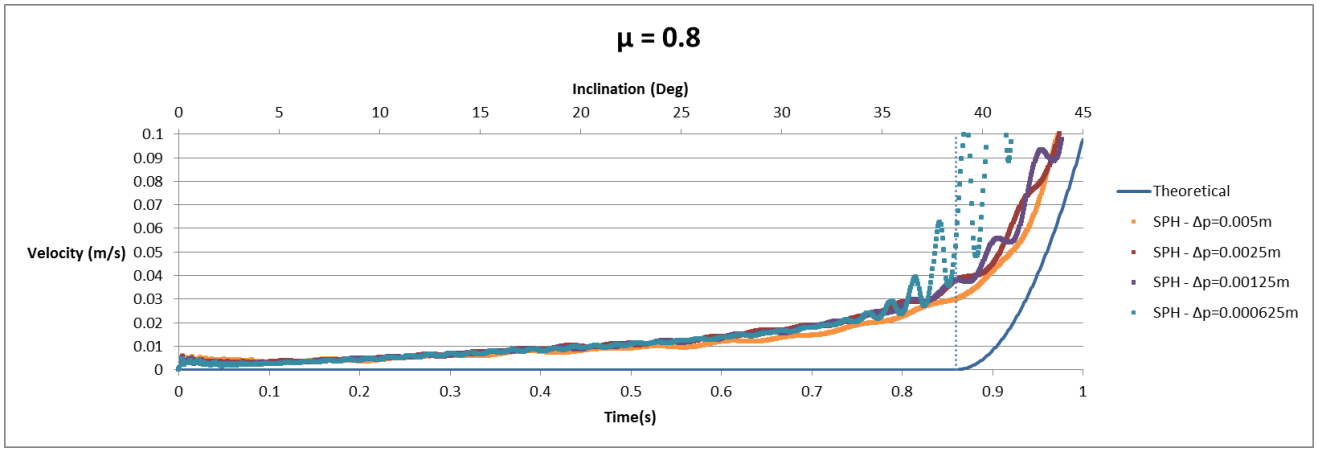

Figure *5-13 - SPH vs. Analytical velocity for various particle spacings for* $\mu = 0.8$

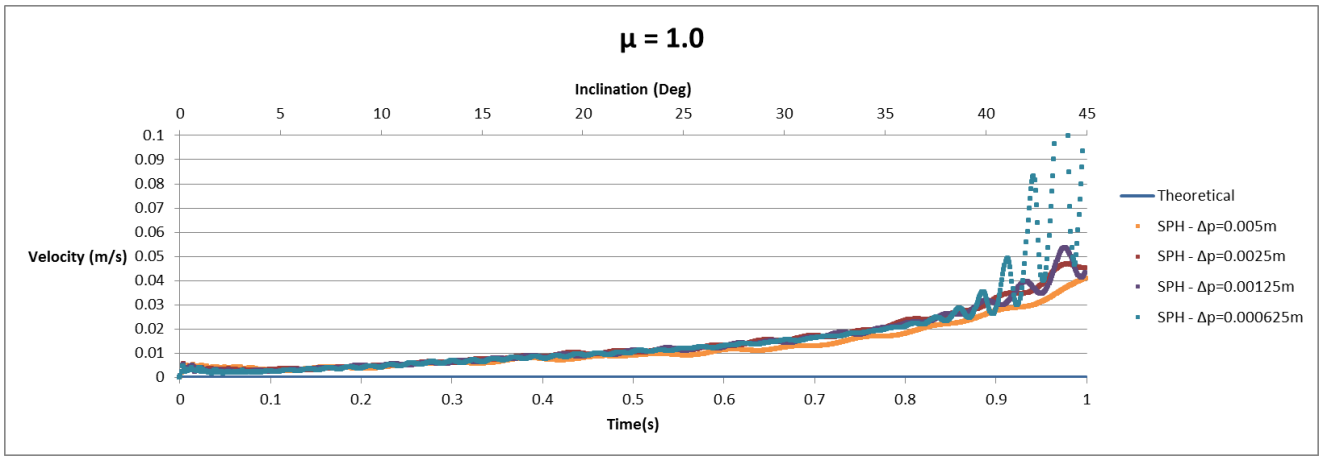

Figure *5-14 - SPH vs. Analytical velocity for various particle spacings for* $\mu = 1.0$

The is a small degree of slippage when the block should remain at rest, for context, the $\mu = 1.0$ case should not slip at all but moves by about 1cm over the one second period. This indicates that an improved model for the initial stick could be developed, however this is left for further work as the main interest is for friction occurring when bodies are in relative motion.

Also, the velocity begins to fluctuate as the particle spacing is refined, this appears to be because the block begins to tilt forward more in the refined cases resulting in some motion in the normal direction which then corrects itself producing a 'bouncing' effect, see Figure 5-15 to Figure 5-17.

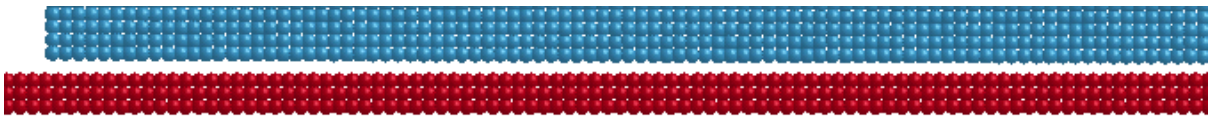

Figure *5-15 Contact between the sliding block and plate at time t=0.7*

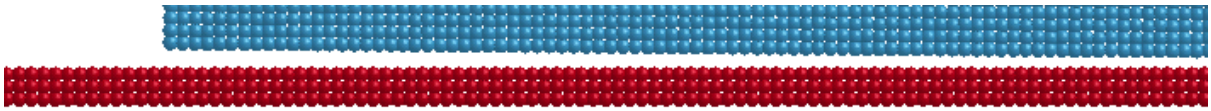

Figure *5-16 Contact between the sliding block and plate at time t=0.8*

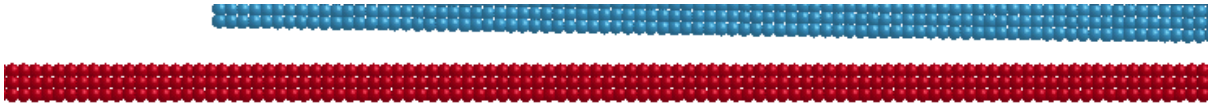

Figure *5-17 Contact between the sliding block and plate at time t=0.9*

5.5.3 3D Metal Forging

The forging problem has been identified as a test problem since it allows the friction model to be tested independently of other model features since the barrelling effect (shown in Figure 5-18) that is described in this section occurs as a direct consequence of the frictional forces that develop between the machining parts and the cylindrical billet.

Forging is a manufacturing process involving the shaping of metal using localised compressive forces. From a computational standpoint this is complex problem involving a number of challenges, large deformations occur as the metal is compressed, and heat transfer and friction become significant factors governing the success of the computation. In this work the goal is to investigate the suitability of the SPH friction algorithm for such problems. More detail on the forging process and simulation can be found in [87]. The particular problem of interest here is the upsetting of a steel billet.

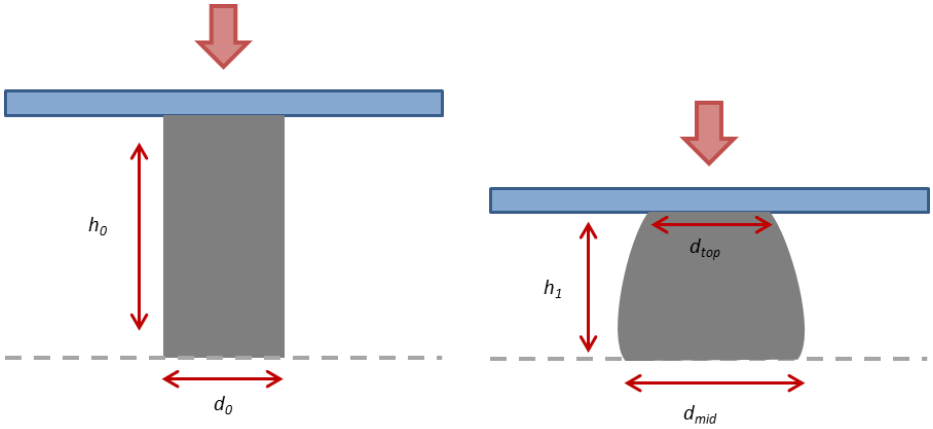

Figure *5-18 – Schematic for 3D metal forging problem*

As the cylinder is compressed a barrelling effect is observed, which is caused by frictional forces at the contact surfaces. The greater the friction, the more barrelling is seen, a perfectly frictionless surface would allow the cylinder to maintain a uniform diameter throughout the forging process.

Material properties

Density	7800 kg/m^3
Young's Modulus	2.1E+11 Pa
Poissons Ratio	0.3
Yield Stress	2.5E+08 Pa
Tangent Modulus	2.1E+10
Material Type	Kinematic/Isotropic Elastic Plastic

Table 7 – Material properties for steel used in the simulation

SPH Properties

Particles	6680 (Quarter of the cylinder)
Smoothing Length	0.005m
Formulation	Total Lagrange

Table 8 – SPH options used for the 3D forging simulation

The material properties selected are typical of steel, although a large variety of metals can be used in forging and machining, the materials in this case are considered to be representative of the type of materials used. The real world problem will generally involve heat transfer as well as deformation of the materials, for simplicity only elastic / plastic deformation is considered, the main reason for this being that the interest of in the testing of the friction model, so it is desirable to introduce as few uncertainties as possible into the testing procedure.

5.5.4 Results

The deformation of the cylinder is measured at specific points relating to the reduction in the height of the cylinder, the mid radius and the top radius are measured, which is consistent with analysis of metal forging problems. The total forging force is plotted along

with a percentage difference between that forging force with friction and that without friction, the rationale being that the forging force grows so rapidly that observing the forging force alone does not demonstrate the differences between the SPH and FEM results properly.

Also the force required to deform the cylinder is recorded and compared to the same force that would be required if friction was not present, this method shows the direct consequence of friction in the forging process with regards to the extra force that is required, in real world terms this is important since the limits of the machinery as well as lubrication methods must be well understood. The forging force is also plotted directly for the SPH and FEM models, although because the growth rate is so large more can be learnt from the plots of the force ratios, however these plots do provide an understanding of the magnitude of the forces involved, again this is important when assessing the limits of the machinery that is used.

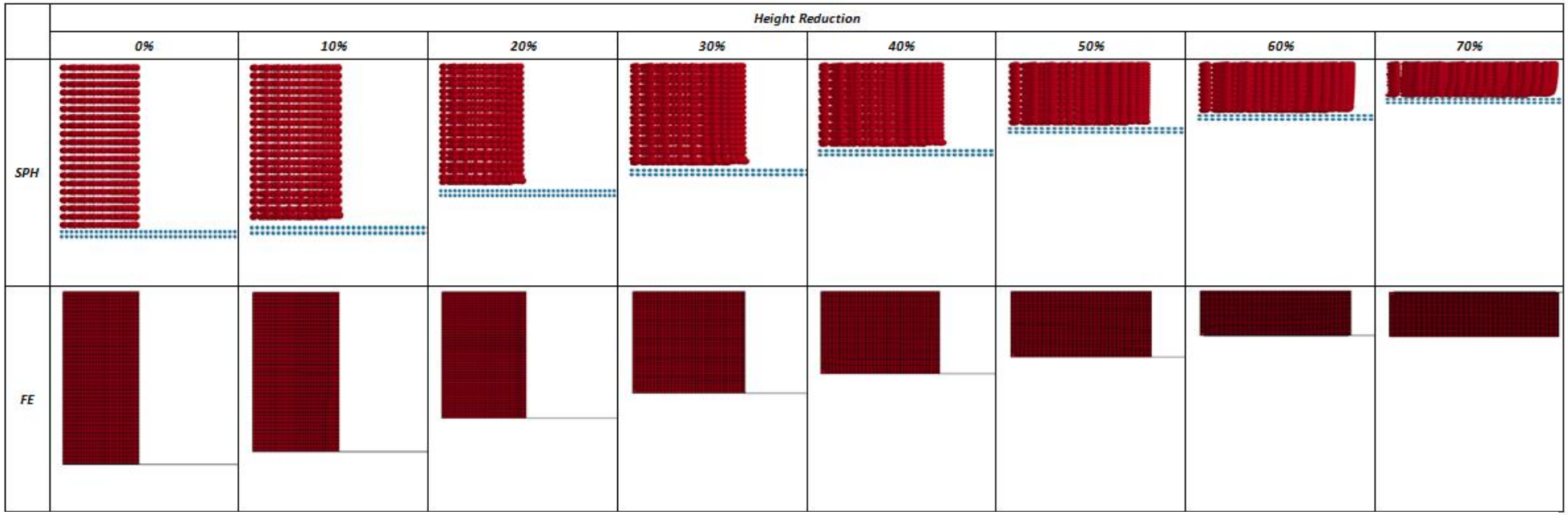

Figure 5-19 – *Height reduction vs. material deformation for* $\mu = 0.0$

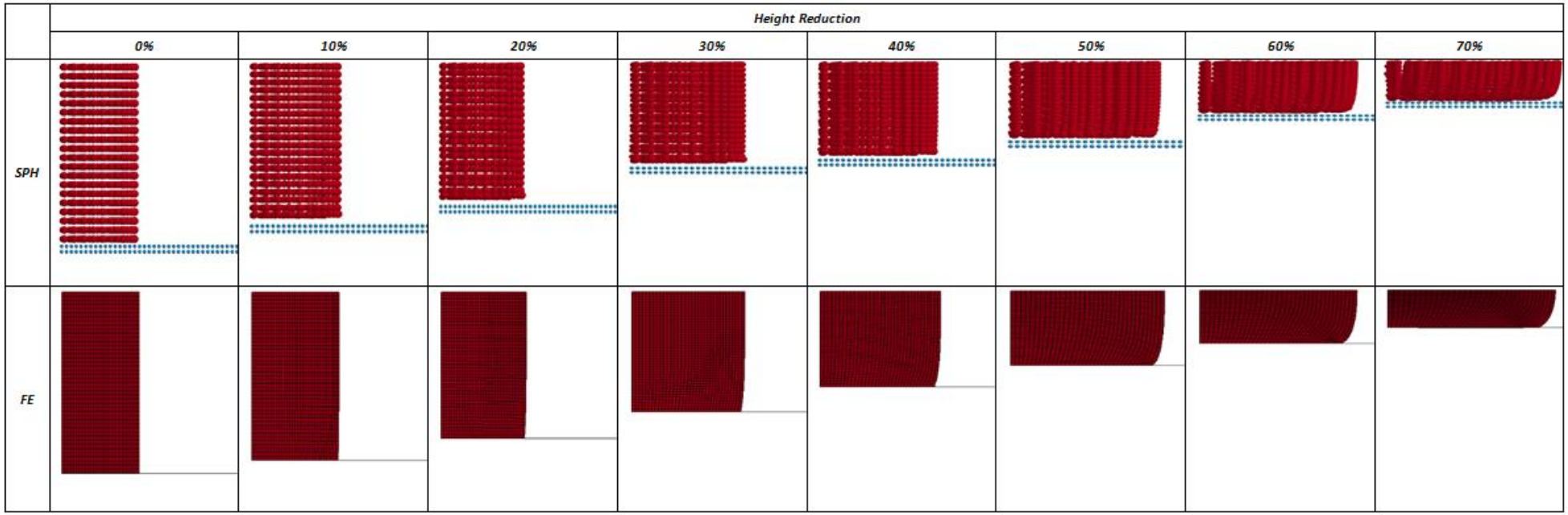

Figure 5-20 - *Height reduction vs. material deformation for* $\mu = 0.1$

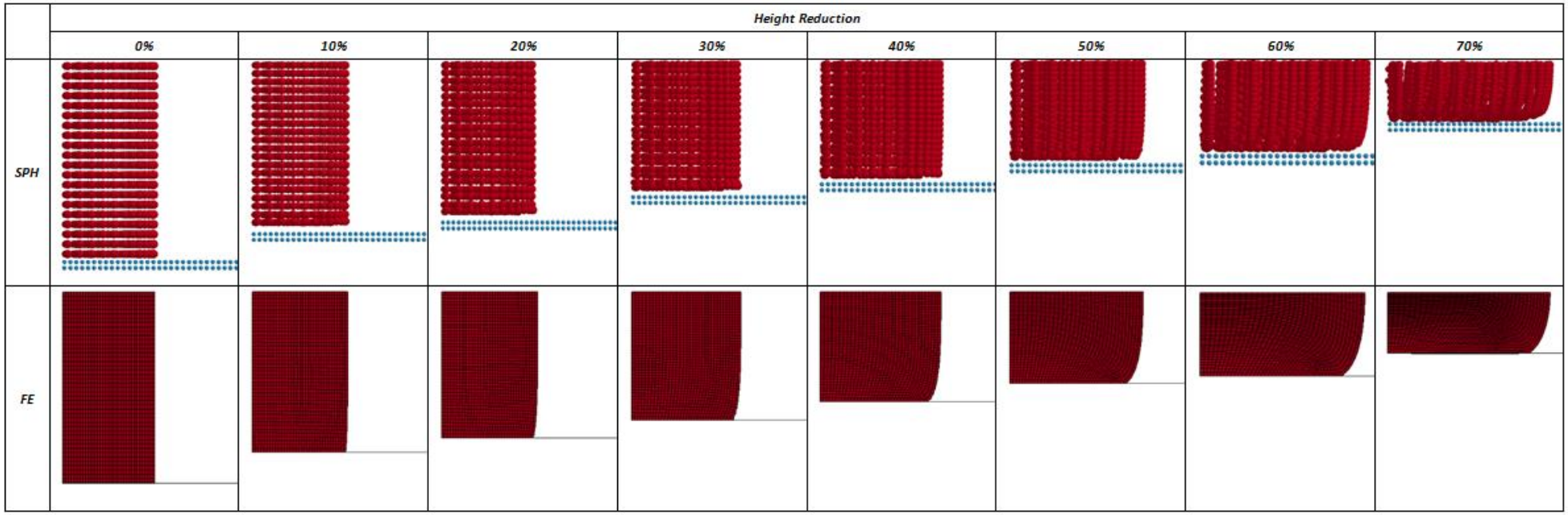

Figure 5-21 - *Height reduction vs. material deformation for* $\mu = 0.2$

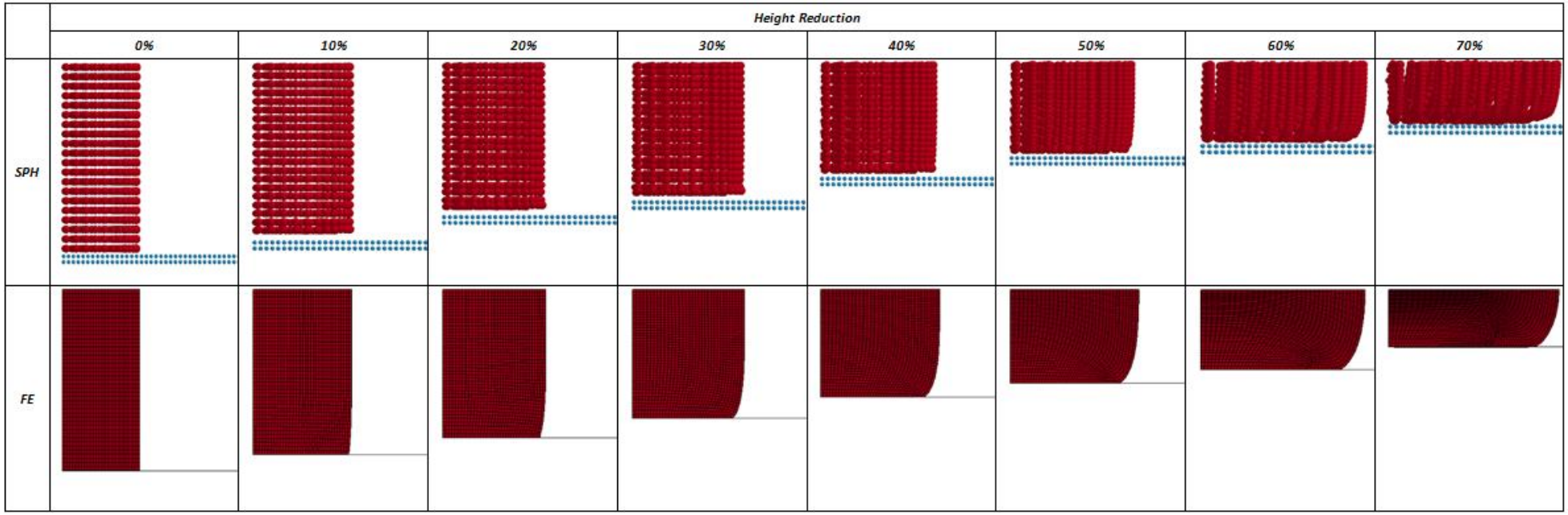

Figure 5-22 - *Height reduction vs. material deformation for* $\mu = 0.3$

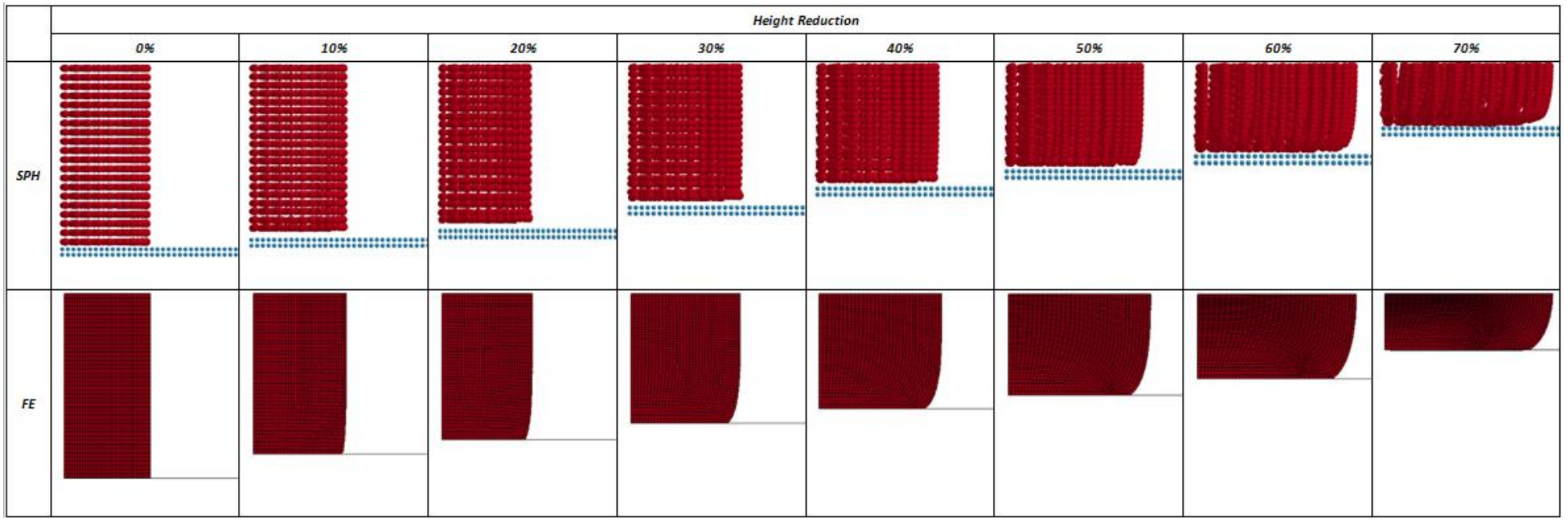

Figure 5-*23* - *Height reduction vs. material deformation for* $\mu = 0.4$

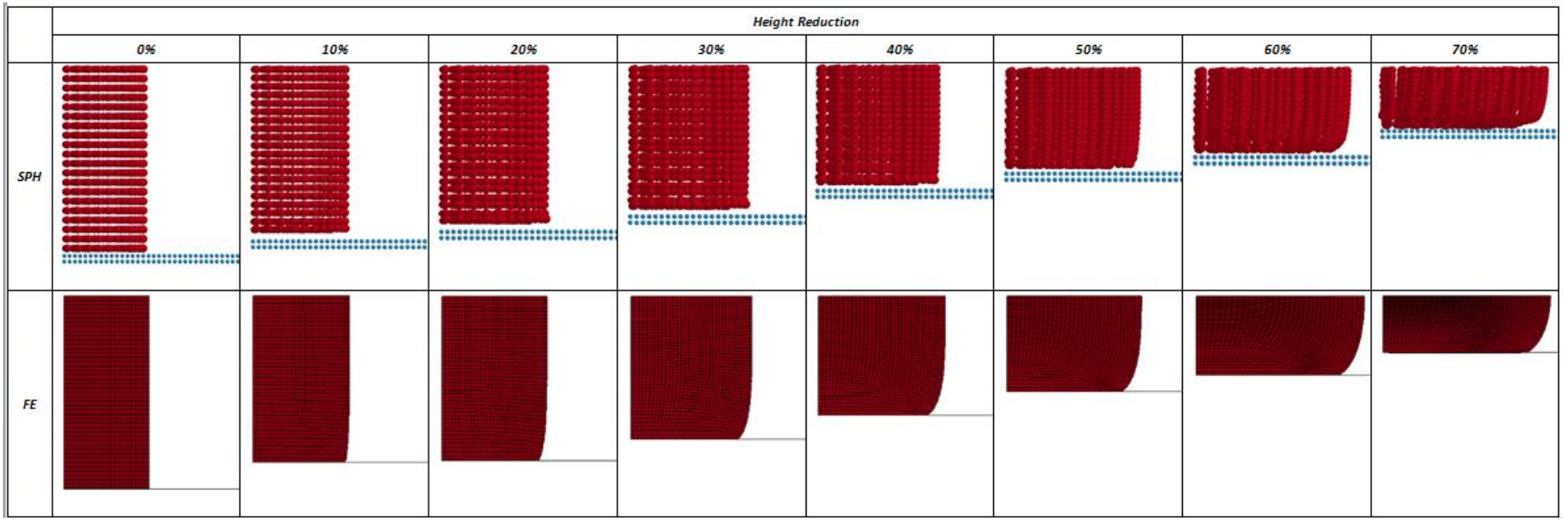

Figure 5-24 - *Height reduction vs. material deformation for* $\mu = 0.5$

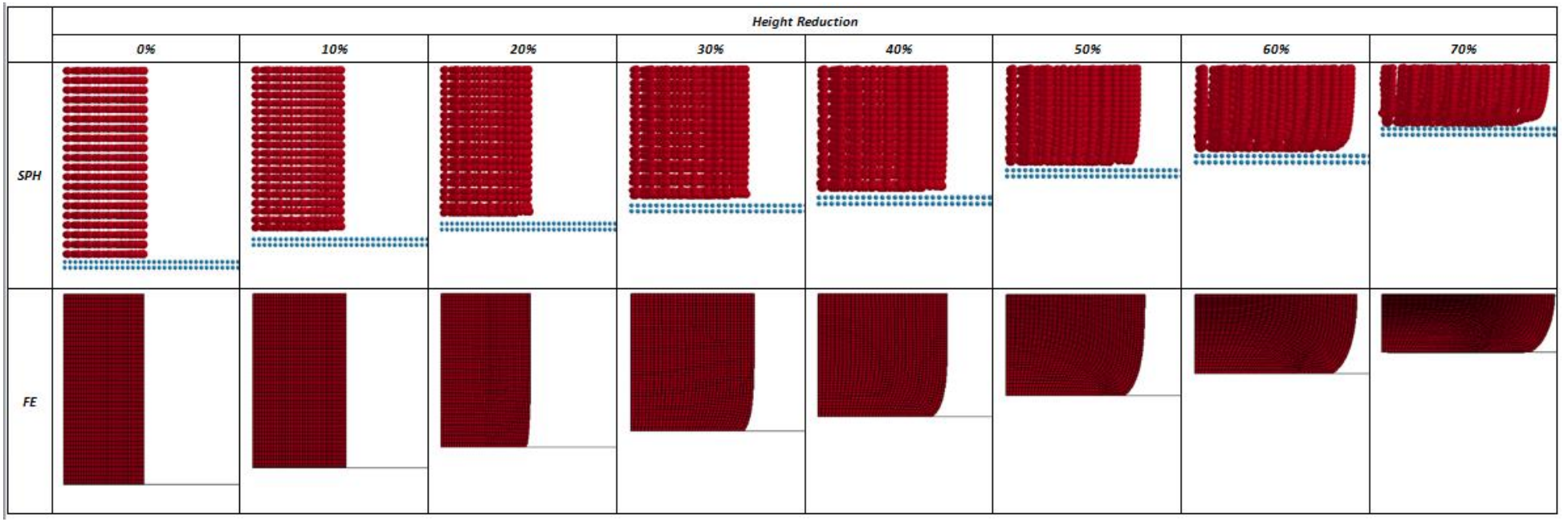

Figure 5-25 - *Height reduction vs. material deformation for* $\mu = 0.6$

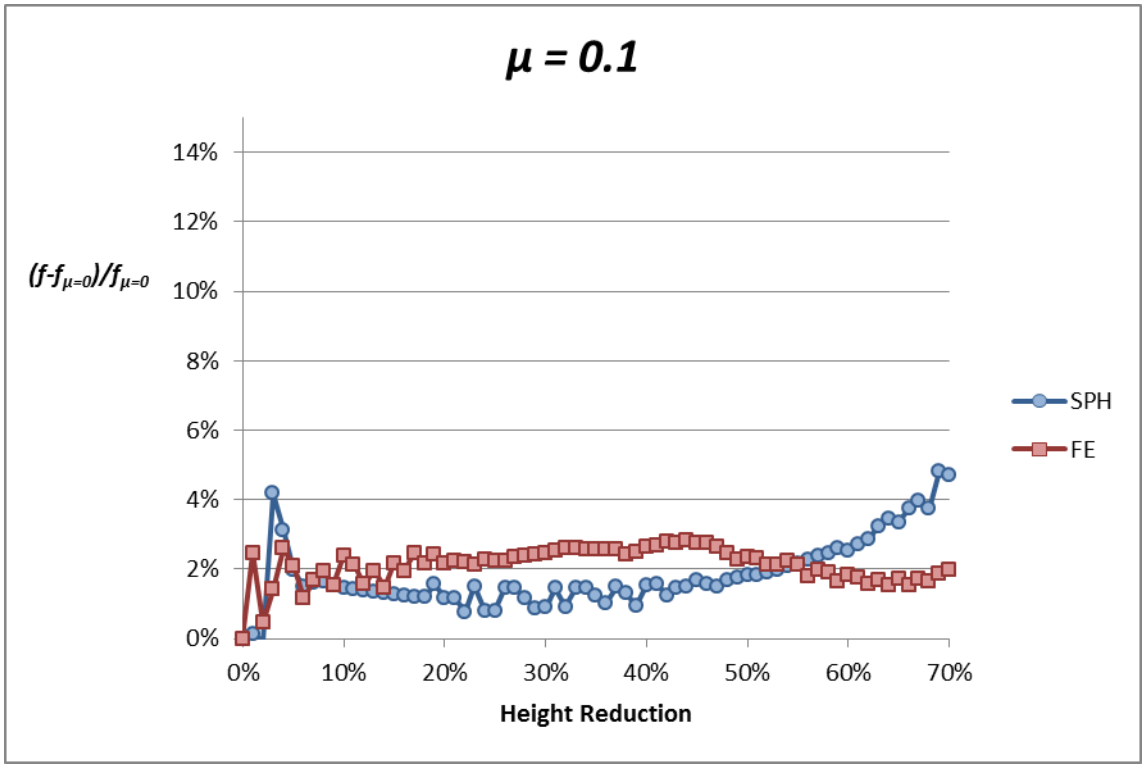

Figure 5-26 – *Ratio of forging force for* $\mu = 0.1$ *to frictionless forging forc*

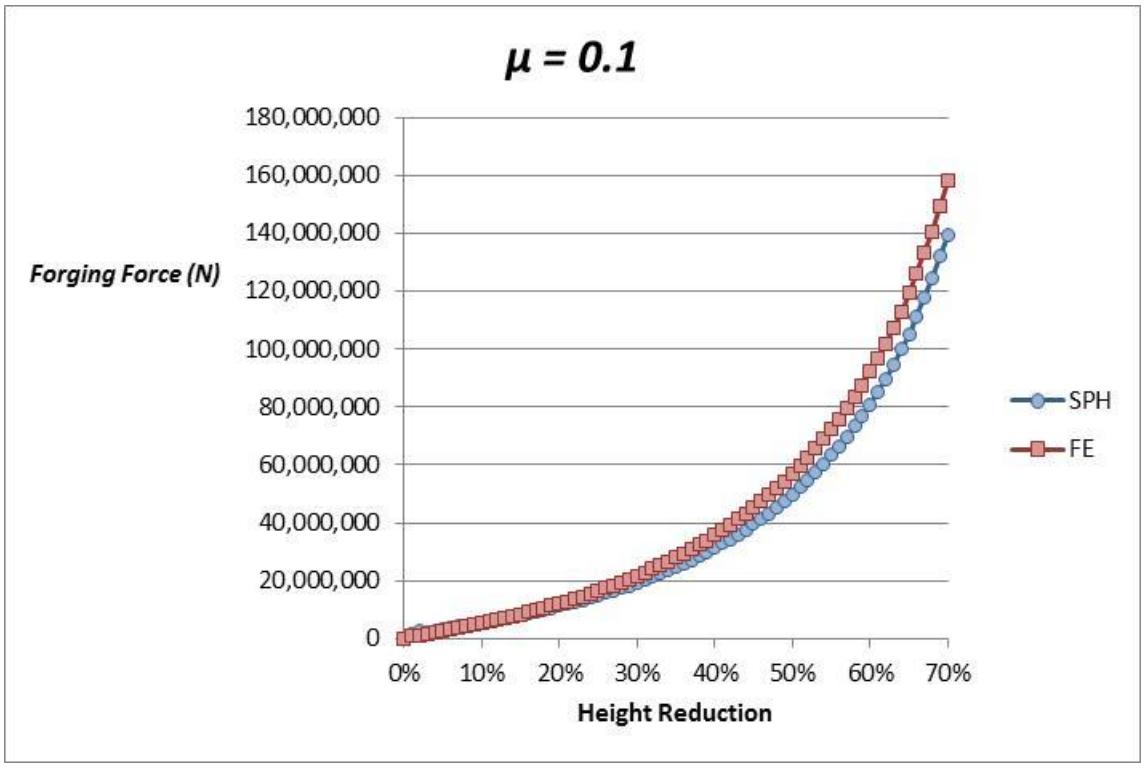

Figure 5-27 – *Forging force for* $\mu = 0.1$

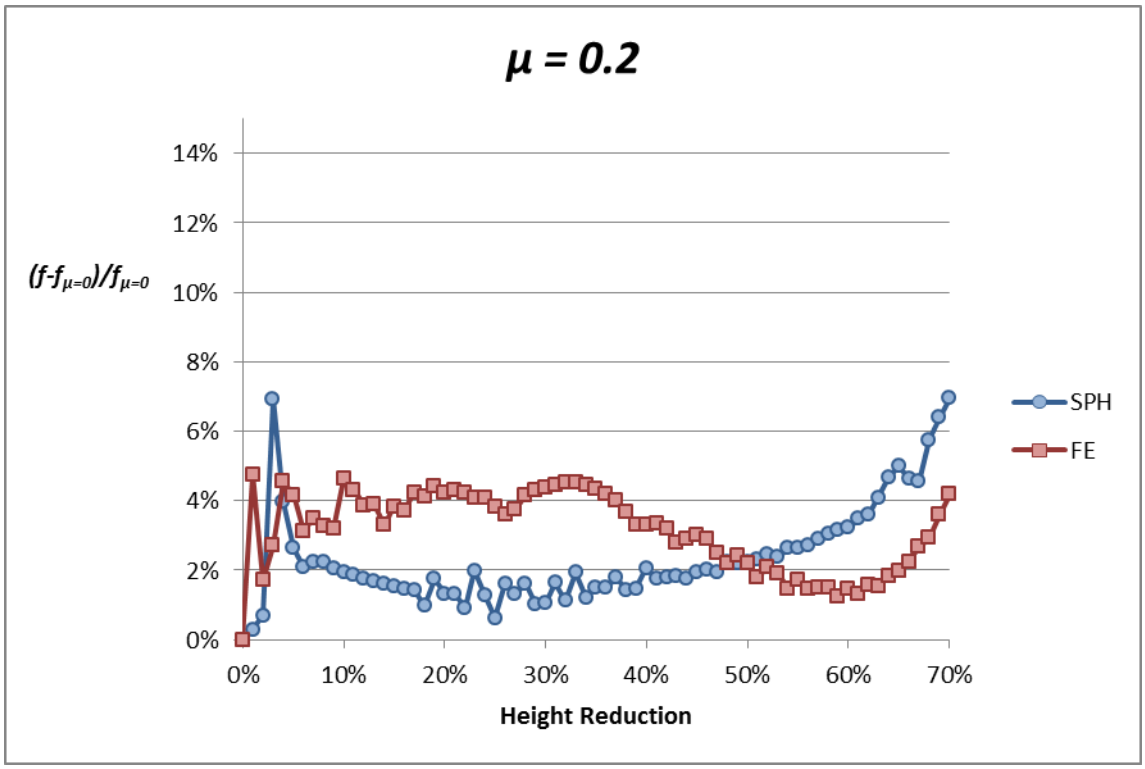

Figure *5-28 - Ratio of forging force for* $\mu = 0.2$ *to frictionless forging force*

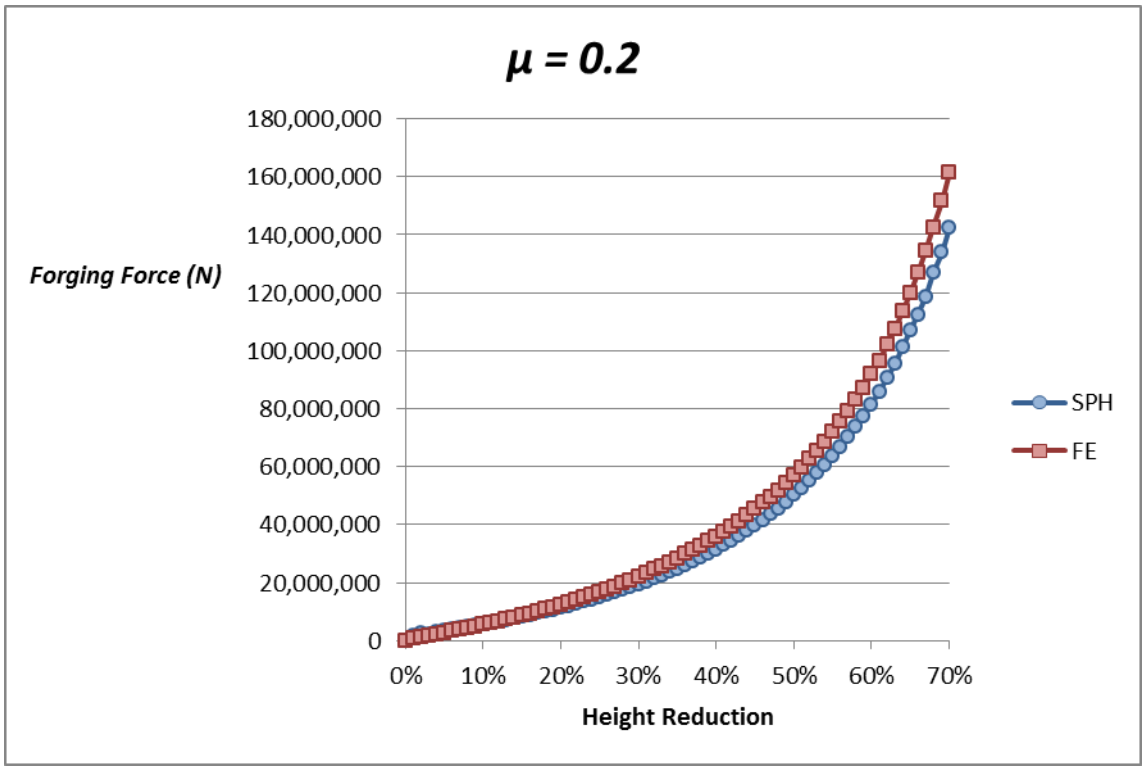

Figure *5-29 - Forging force for* $\mu = 0.2$

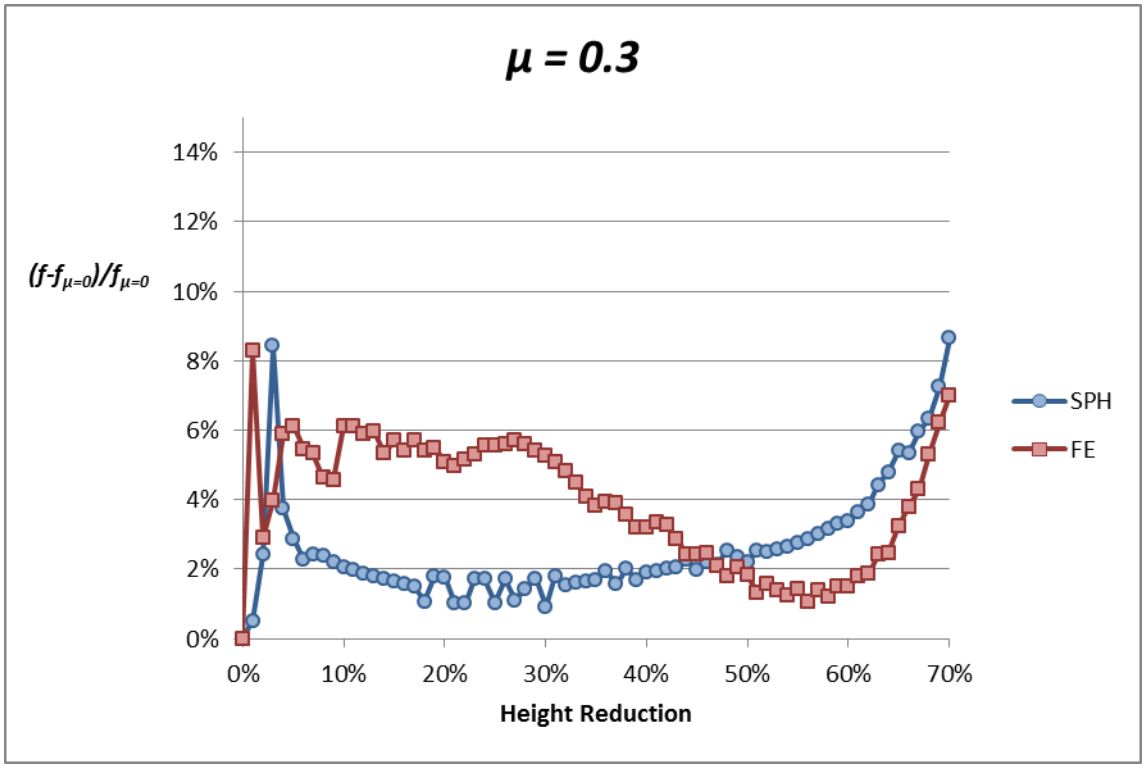

Figure *5-30 - Ratio of forging force for* $\mu = 0.3$ *to frictionless forging force*

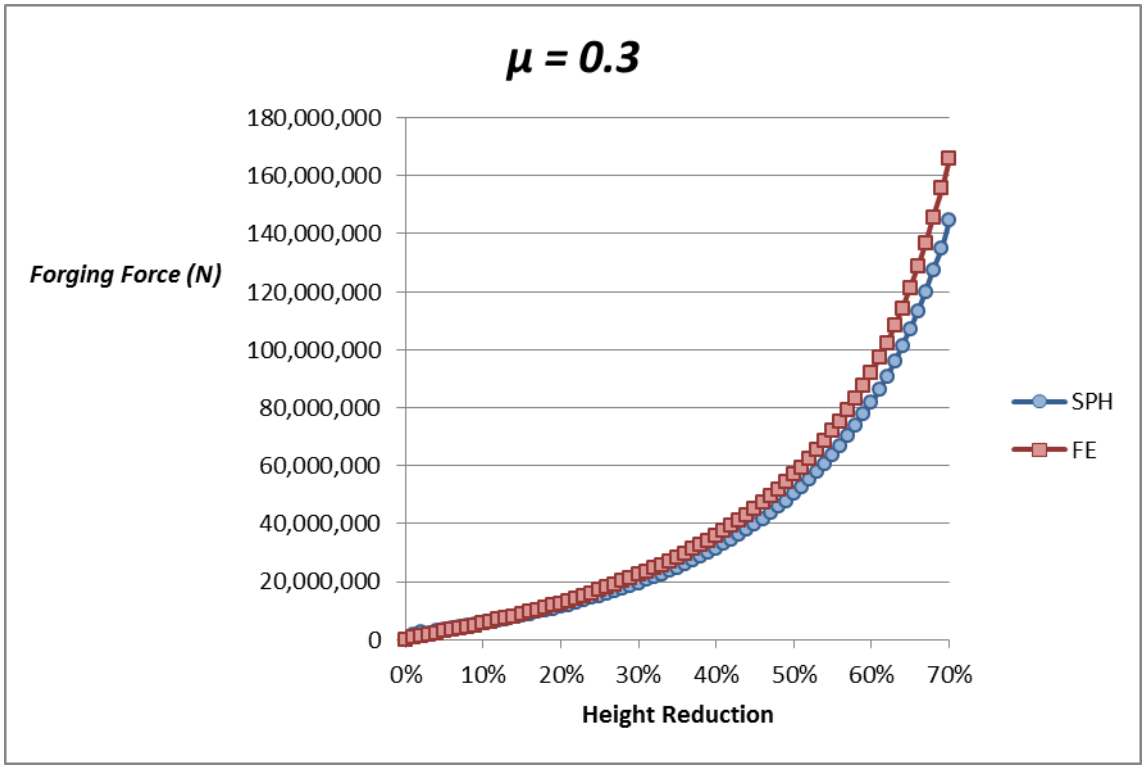

Figure *5-31 - Forging force for* $\mu = 0.3$

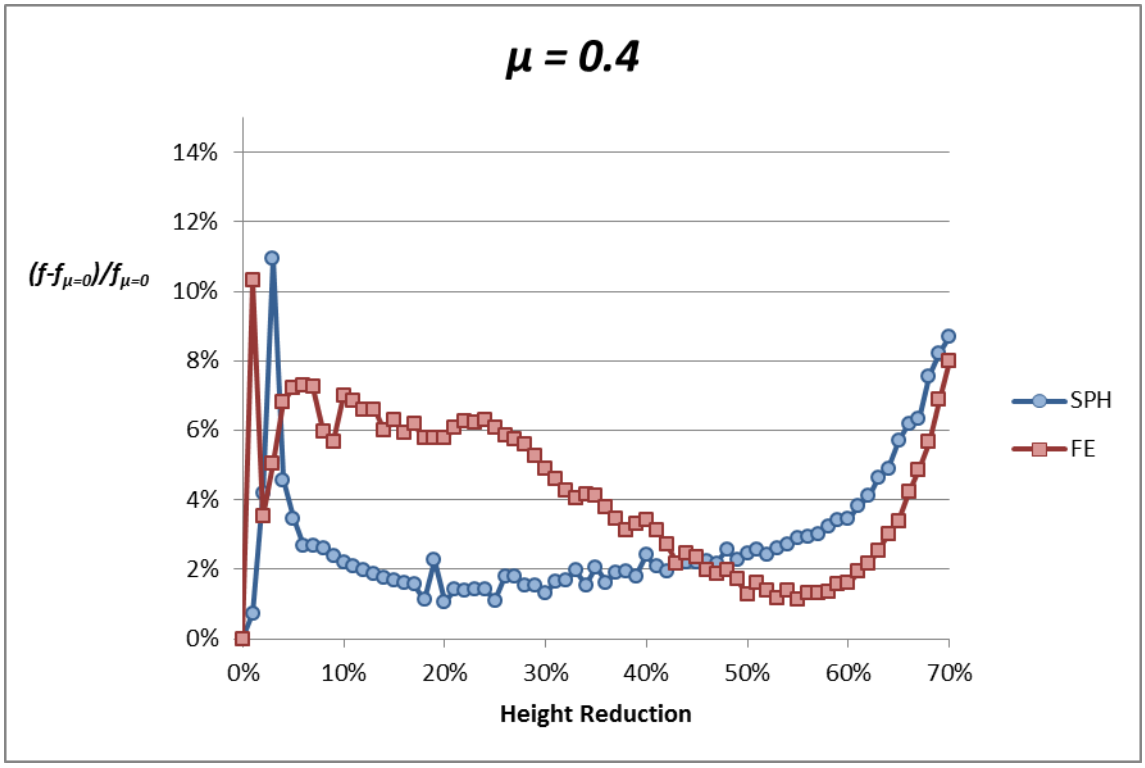

Figure 5-*32Ratio of forging force for μ=0.4 to frictionless forging force*

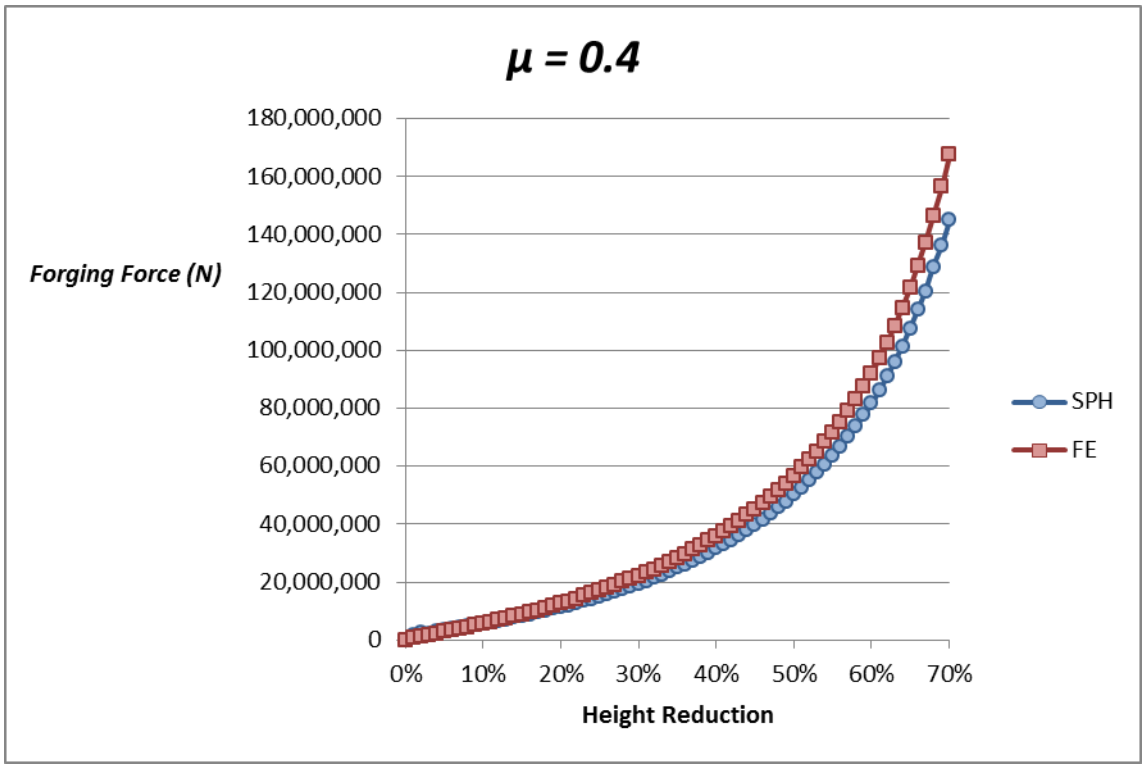

Figure *5-33 - Forging force for* $\mu = 0.4$

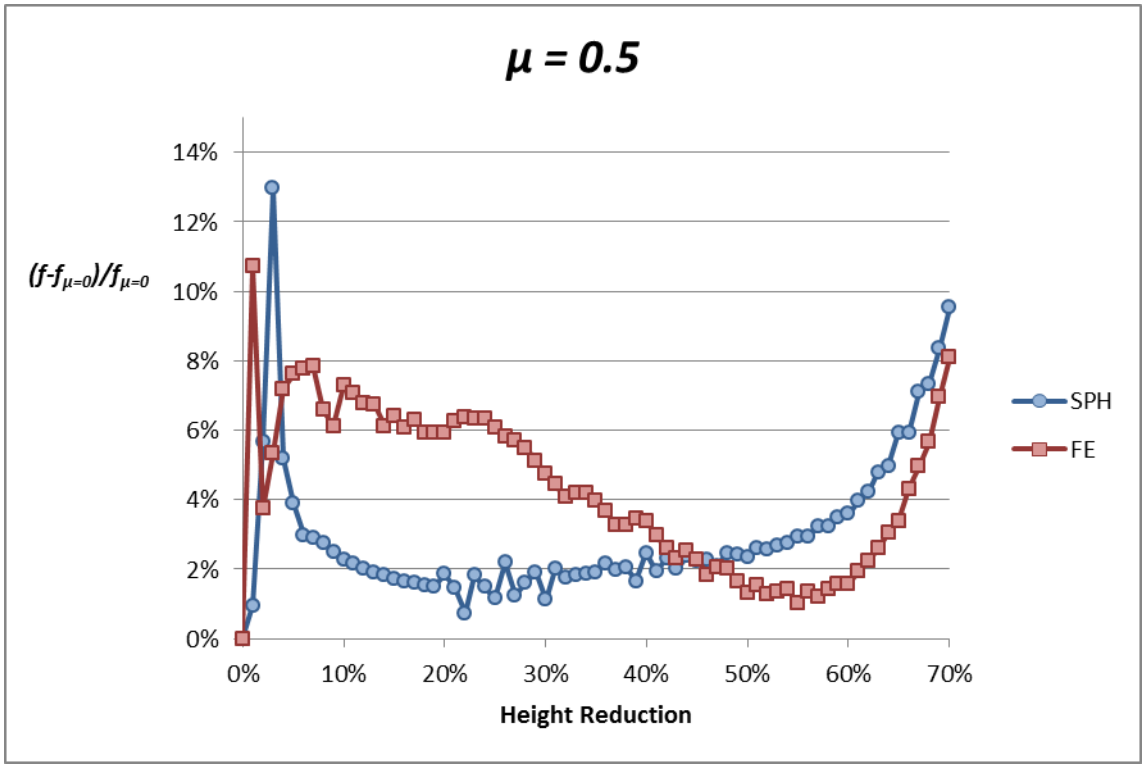

Figure *5-34 - Ratio of forging force for* $\mu = 0.5$ *to frictionless forging force*

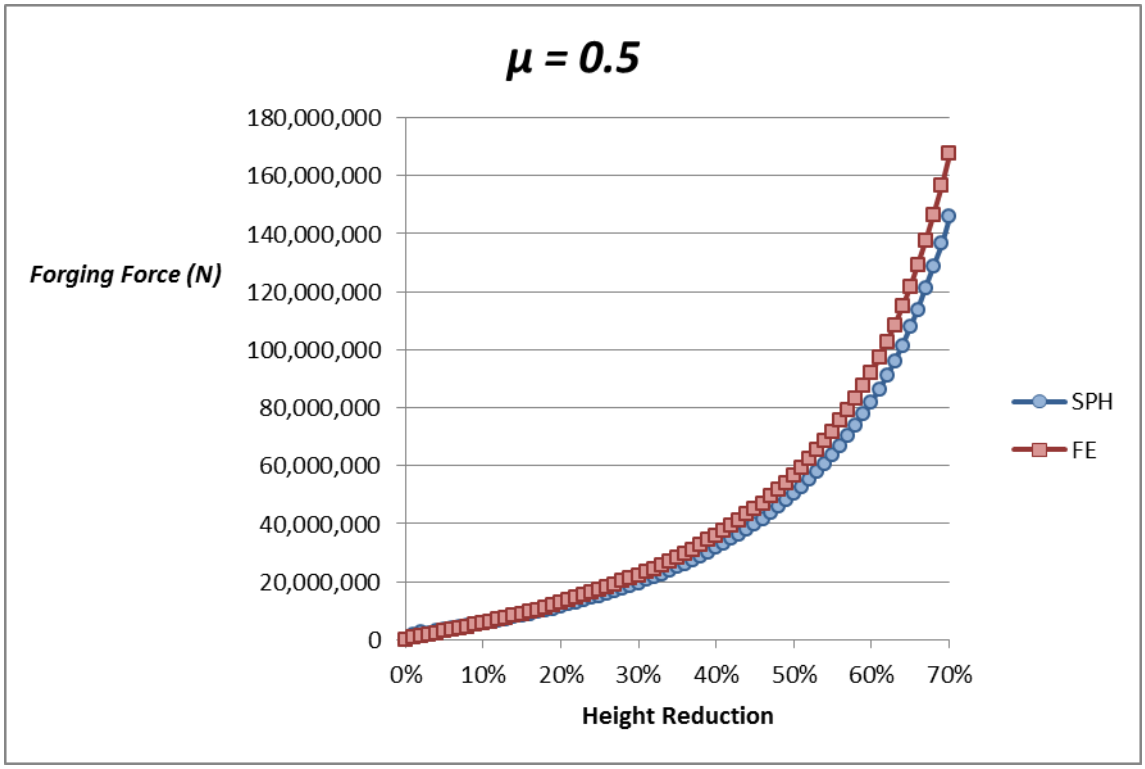

Figure *5-35 - Forging force for* $\mu = 0.5$

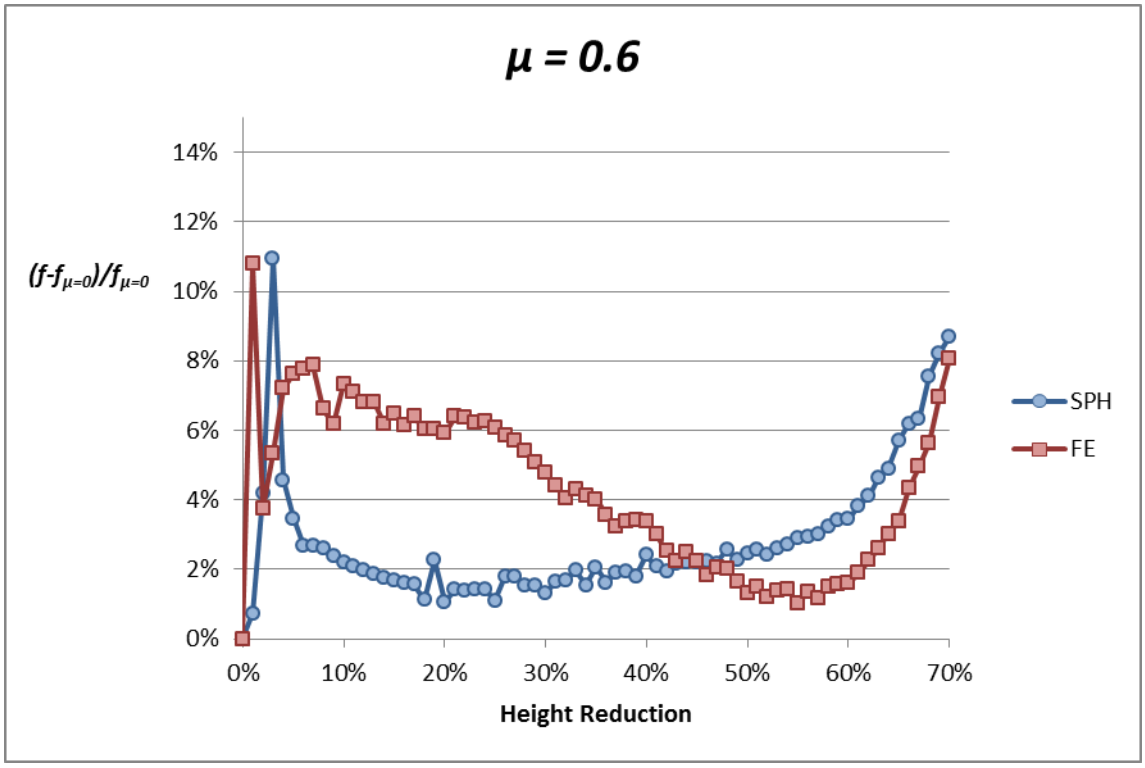

Figure *5-36 - Ratio of forging force for* $\mu = 0.6$ *to frictionless forging force*

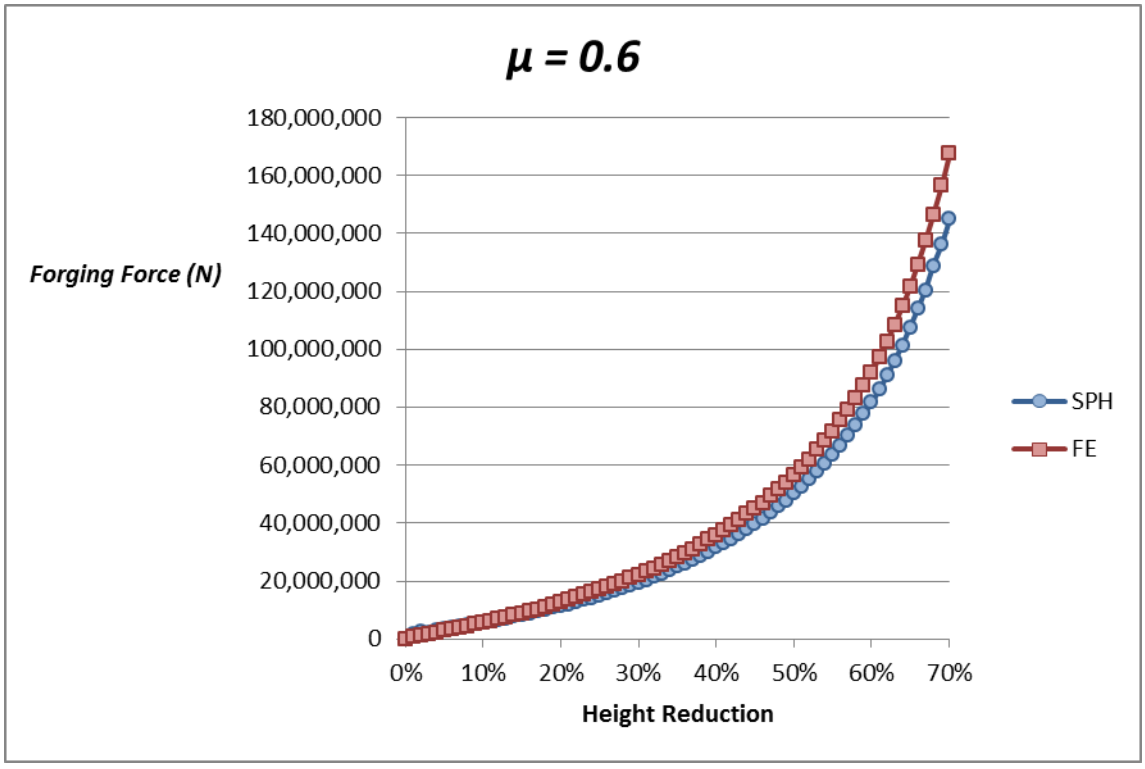

Figure *5-37 - Forging force for* $\mu = 0.6$

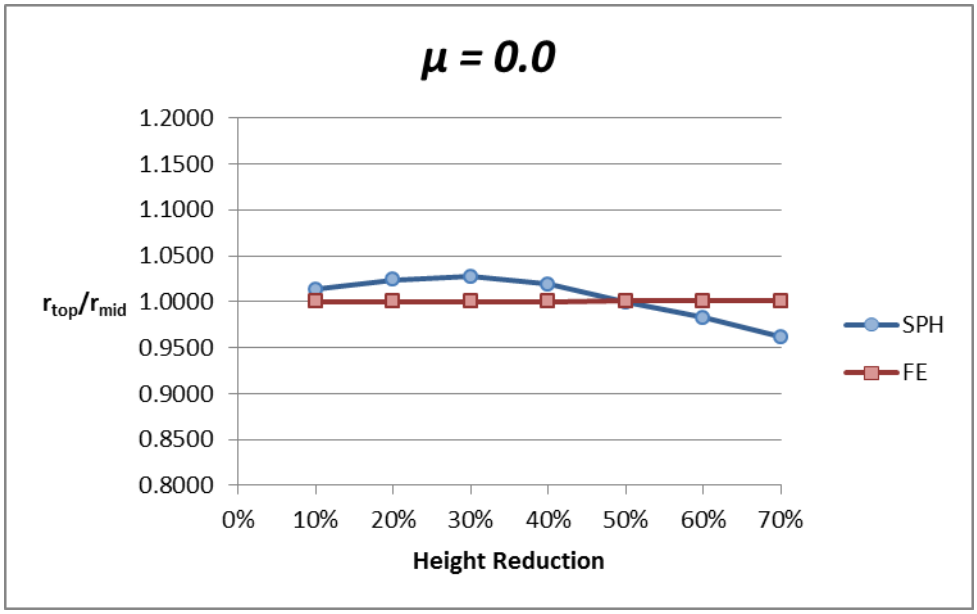

Figure *5-38 – Ratio of top radius to barrelled mid radius for* $\mu = 0.0$

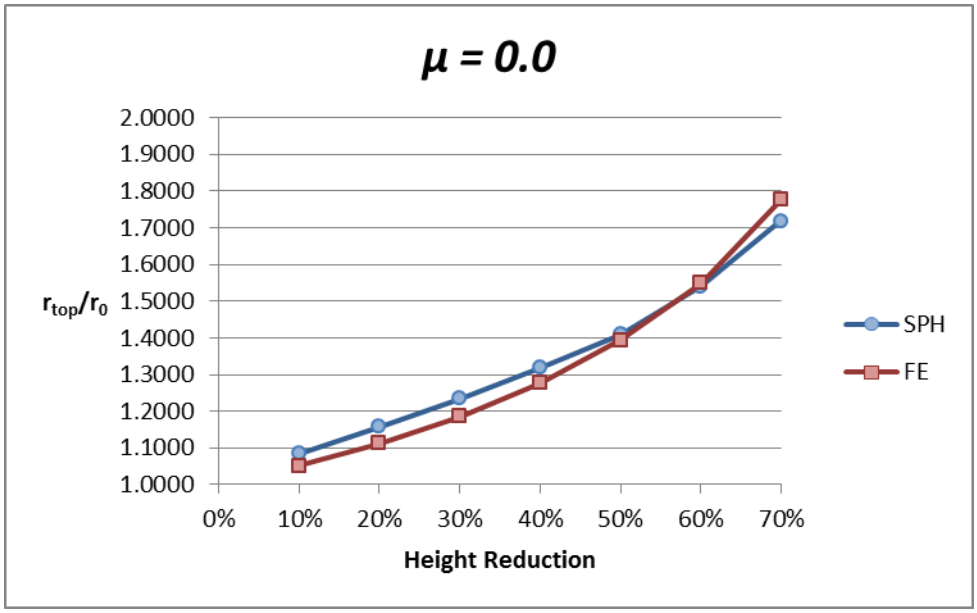

Figure *5-39 - Ratio of top radius to initial top radius for* $\mu = 0.0$

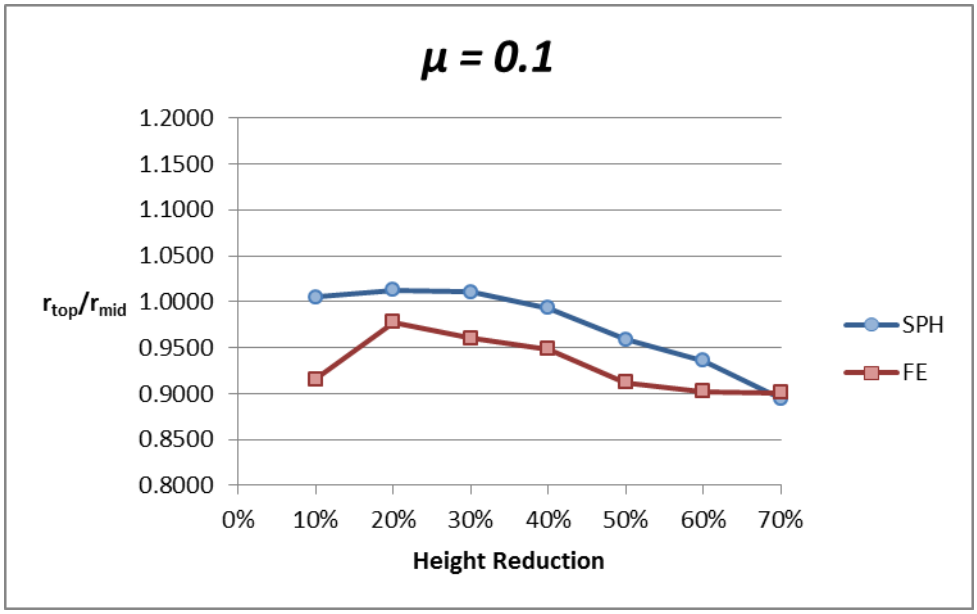

Figure *5-40 - Ratio of top radius to barrelled mid radius for* $\mu = 0.1$

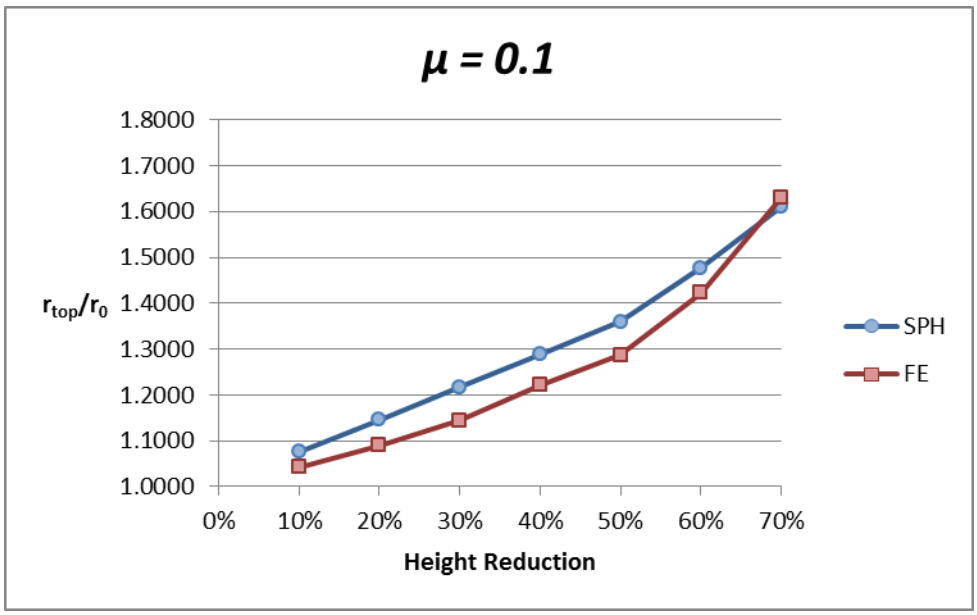

Figure *5-41 - Ratio of top radius to initial top radius for* $\mu = 0.1$

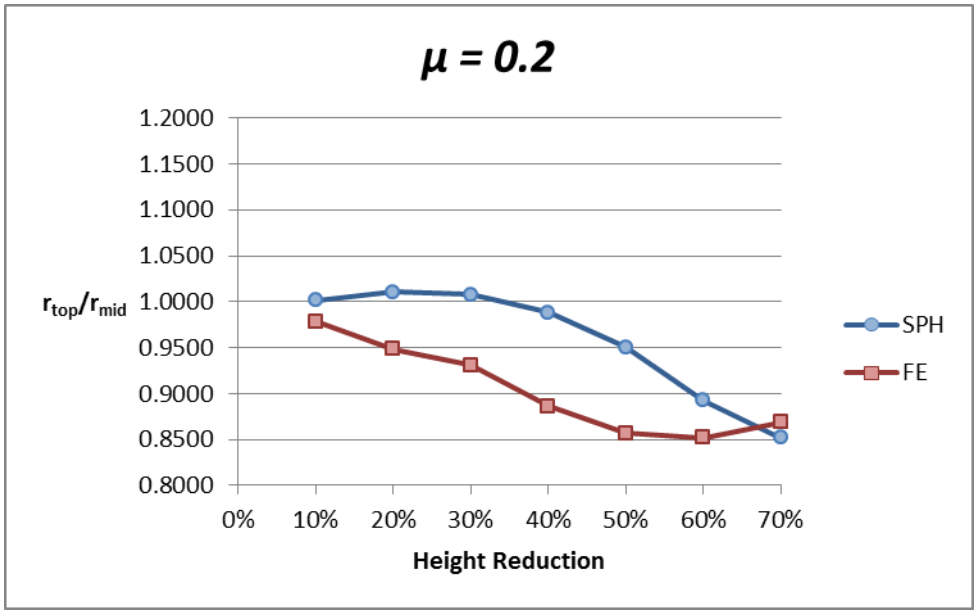

Figure *5-42 - Ratio of top radius to barrelled mid radius for* $\mu = 0.2$

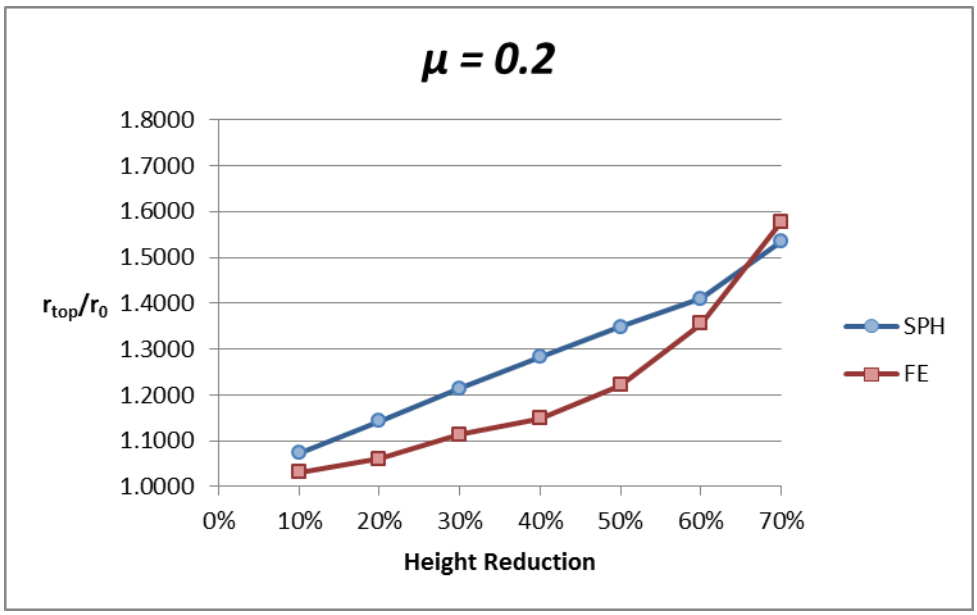

Figure *5-43 - Ratio of top radius to initial top radius for* $\mu = 0.2$

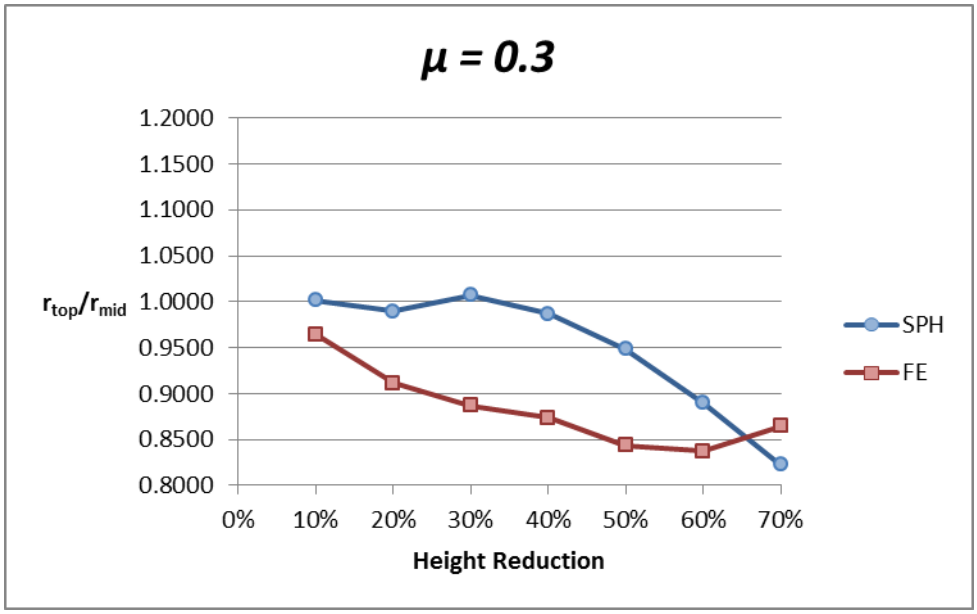

Figure *5-44 - Ratio of top radius to barrelled mid radius for* $\mu = 0.3$

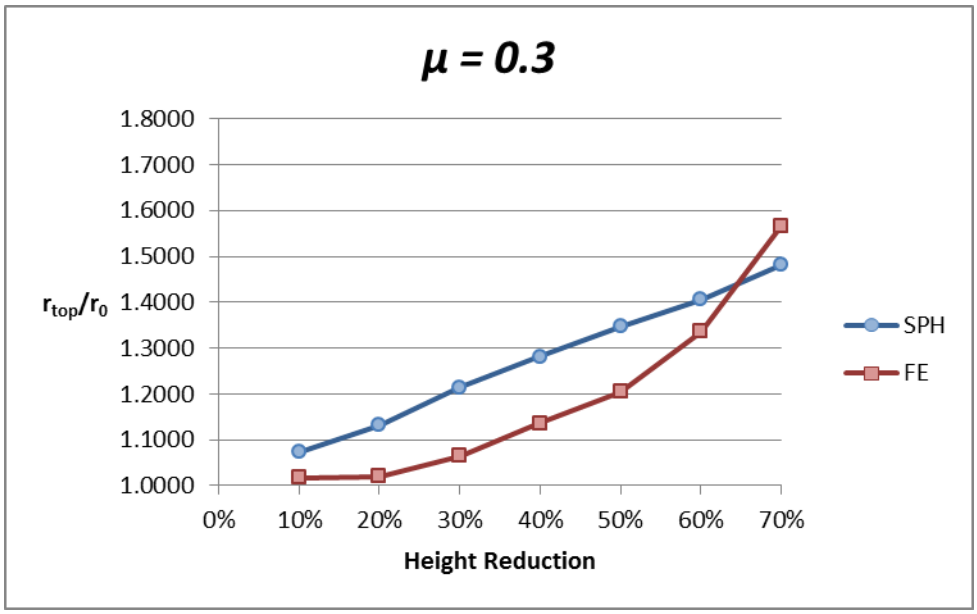

Figure *5-45 - Ratio of top radius to initial top radius for* $\mu = 0.3$

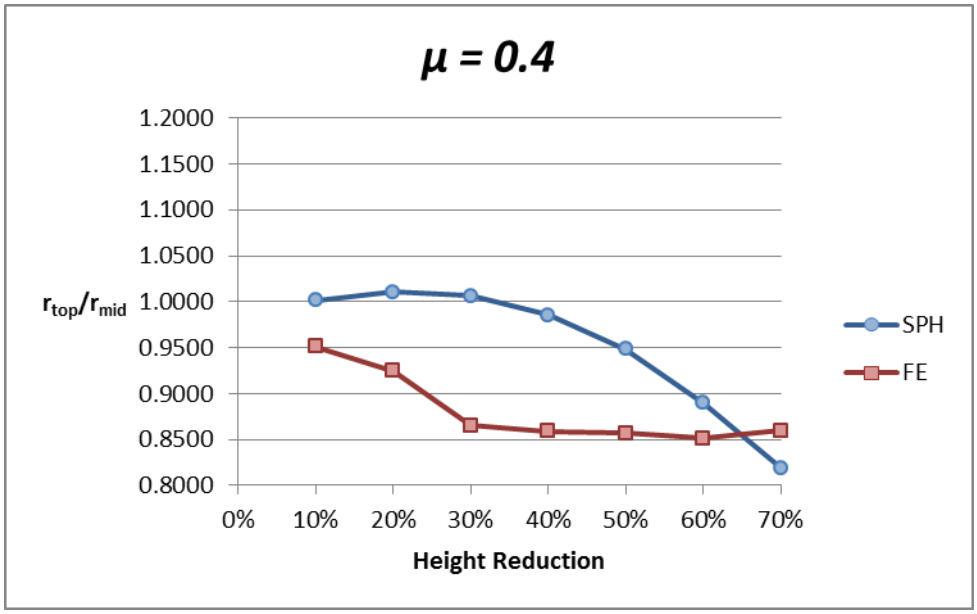

Figure *5-46 - Ratio of top radius to barrelled mid radius for* $\mu = 0.4$

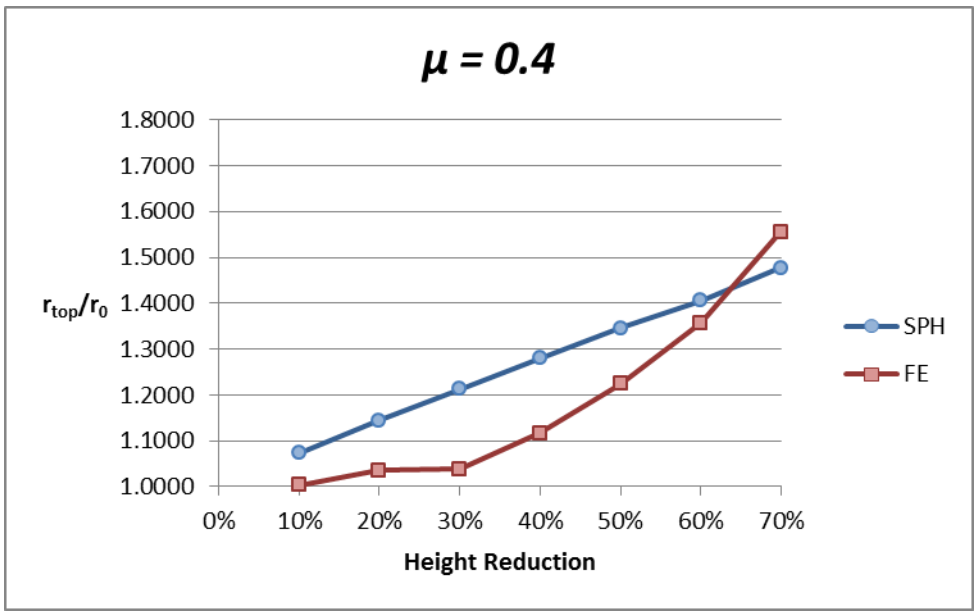

Figure *5-47 - Ratio of top radius to initial top radius for* $\mu = 0.4$

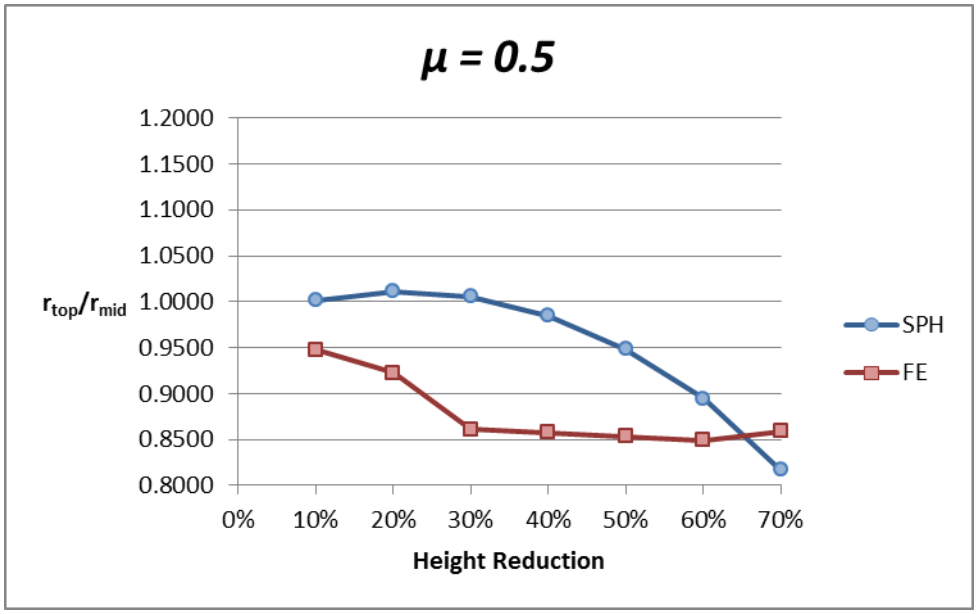

Figure *5-48 - Ratio of top radius to barrelled mid radius for* $\mu = 0.5$

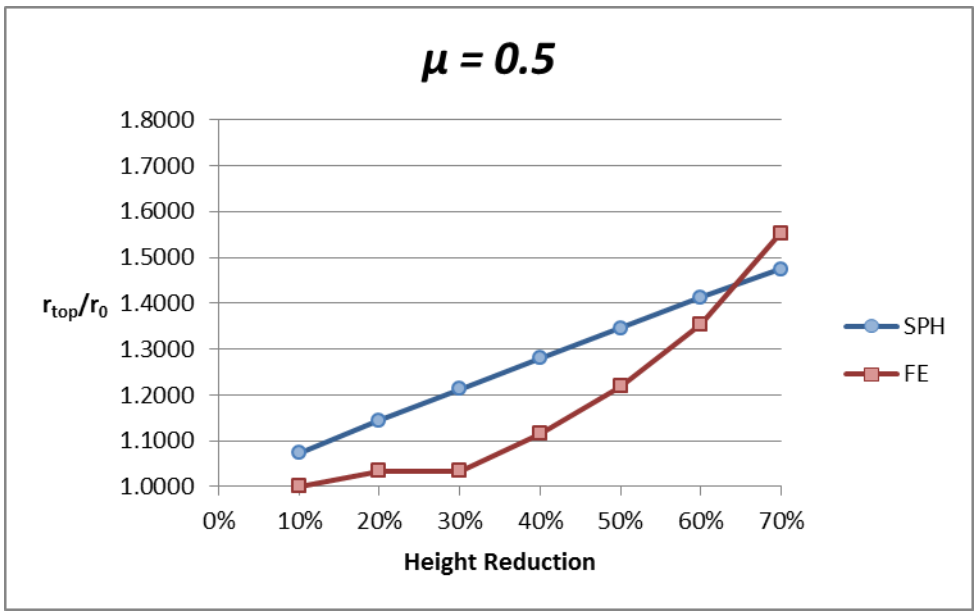

Figure *5-49 - Ratio of top radius to initial top radius for* $\mu = 0.5$

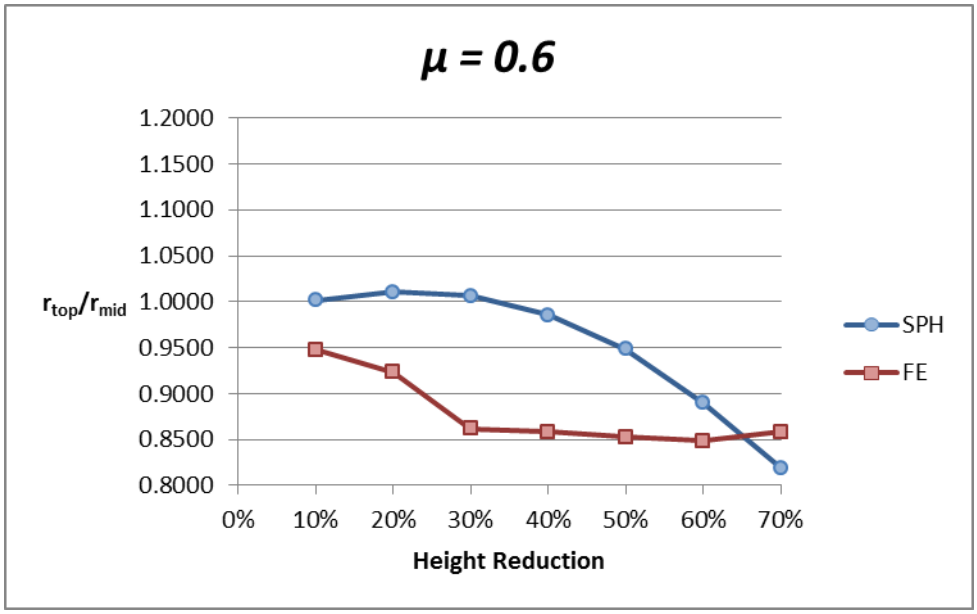

Figure *5-50 - Ratio of top radius to barrelled mid radius for* $\mu = 0.6$

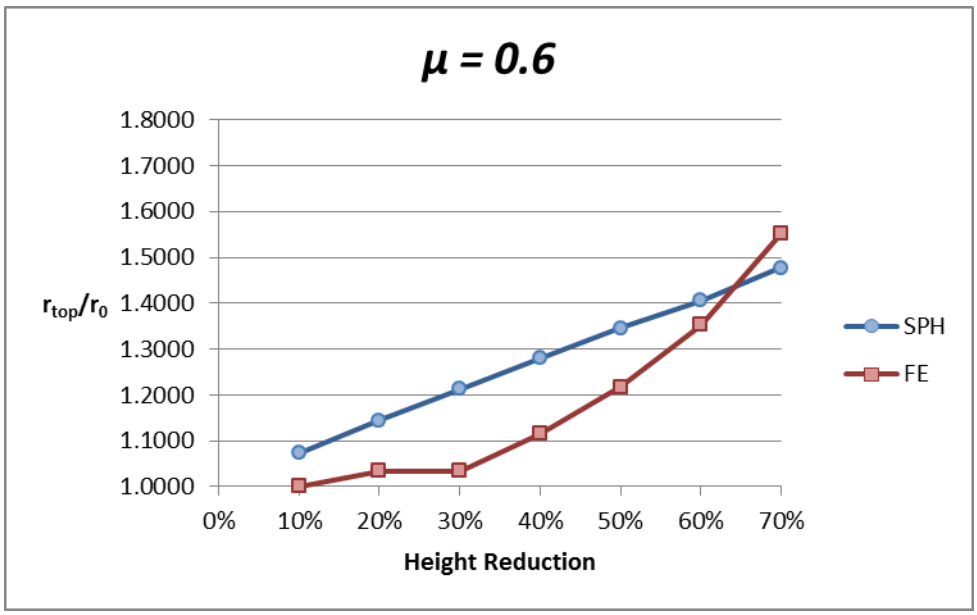

Figure *5-51 - Ratio of top radius to initial top radius for* $\mu = 0.6$

5.6 Conclusions

The test cases presented in this chapter clearly verify the contact friction algorithm that is implemented in an SPH framework. Analytical results in 2D can be matched with good accuracy. In 3D the forging example performs less well but the contribution of the friction algorithm is clearly seen. The differences are thought to be down to the numerical methods in question rather than solely down to differences in the modelling of friction. The tests would benefit from an analytical solution to compare to, some of which are available but often simplified in terms of the friction coefficient.

This chapter completes the final part of the objective defined in chapter one, §1.4.1, resulting in a relevant and novel improvement to the SPH method which to date is not to be found in literature. The completion of this objective sets a strong foundation for further research concentrating on the remaining objectives.

6 Correcting for Loss of Mass Continuity

6.1 Introduction

The tensile instability as described in chapter three is essentially the manifestation of either an incorrect approximation of the acceleration via the momentum equation, or an incorrect approximation of density via the interpolation of the velocity gradient. These errors could in turn come from errors in other parts of the calculation such as the kinematic relations or the constitutive model. Therefore one type of solution is to make appropriate corrections to account for these errors, but the other more fundamental problem is to identify the original source of the error. This process of heuristic solutions is reviewed in chapter three.

A key calculation in the SPH calculation is the approximation of density through the SPH continuity equation, this then feeds into other parts of the calculation such as the calculation of the pressure, the central difference algorithm used in the MCM code is described in chapter two.

In this chapter a possible source of error is identified in the discrete form of the continuity equation, which when fixed will mimic the continuous form more closely. The objective of this chapter is to provide an investigation into the effect of this correction on the stability properties of the SPH method.

The influence of conservative properties on the stability and convergence of a numerical scheme is investigated and builds on the review provided in chapter three, the correction method developed in this chapter has not yet been studied in and SPH framework.

Figure 6-1 shows a common representation of the phasing of displacement, velocity and acceleration, which are said to be 90^{o} out of phase with one another, in other words displacement is at a maximum or minimum when there is no velocity, and velocity is at a maximum when there is no acceleration. In SPH these field variables are calculated sequentially in the explicit central difference scheme, which is described step by step in chapter one. The acceleration is calculated by solving the momentum equation via SPH interpolation, the velocity is then updated, followed by the particle positions. Therefore the field variables are strongly linked, suggesting that error in the calculation of one of these field variables, left uncorrected, could lead to unstable growth.

Corrections to the method will often correct one of the three phases, for example Monaghan's artificial stress [41] [42] is added to the momentum equation which corrects the approximation of the particle acceleration, this then will follow through to the velocity and displacement, the XSPH variant [84] effects the movement of the particle at the displacement phase but does not directly affect the velocity and acceleration. Conservative smoothing involves a smoothing of the velocity, density and internal energy fields [23] [44]. Clearly there are many instances in the calculation where attempts can be made to supress the instability, which as was discussed in chapter three, does not necessarily address the root cause of the problem.

In this chapter, one potential source of error in the calculation is identified, leading towards a modified set of equations being developed, which is then tested against the benchmark test for tensile instability as was introduced in chapter three.

As discussed in chapter three, the SPH form of the continuity equation does not conserve volume exactly. The calculation involves finding the gradient of the velocity field, related to the strain rate or rate of deformation. This means the error is in the velocity phase (strain is related to displacement and therefore strain *rate* is phased with the velocity). It has been identified that corrections can be made to account effect of this error. The stability properties of the correction can then be investigated.

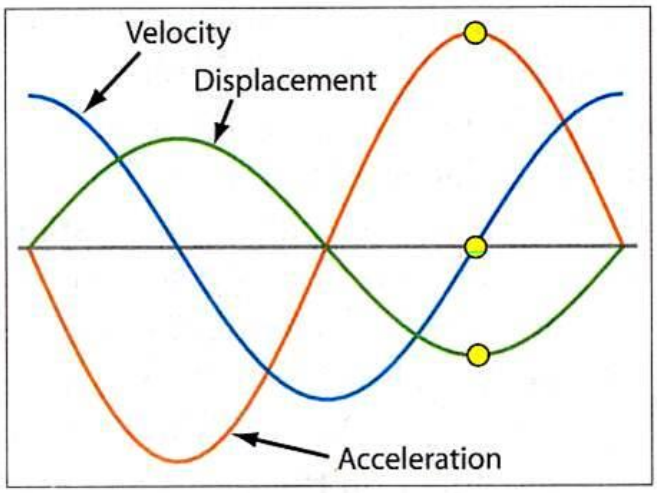

Figure *6-1 Phasing regime for acceleration, velocity, and acceleration, (source: [88])*

6.2 Density Approximation

The governing equations (momentum and continuity) were stated in chapter two along with their discrete counterparts in SPH form. The continuity equation is typically used to approximate the density and evolve it in time. However the density can also be calculated directly, by simply performing a kernel weighted (SPH) average of the masses over the neighbouring particles. This method is widely used in SPH codes due to its simplicity and since this approximation preserves volume both locally and globally, however a drawback of this approach is that material discontinuities become overly smoothed [54], [89], so therefore although the SPH form of the continuity equation does not conserve volume exactly (mass is inherently conserved since it is assumed constant for each particle), it is often more desirable to use this form (see discussion in chapter three)

Although the form of the momentum equation, as derived in §2.2.5, is well known to produce more accurate results than simpler forms, it has been understood that discretisation's that conserve momentum exactly are more likely to exhibit instabilities [46]. This leads to a rationale for investigating improvements in this area, is it possible to maintain conservation properties but improve stability. Similarly, is it possible to do the same with mass continuity, can the desirable properties of the discrete continuity equation be maintained but without allowing conservation of mass to be violated.

6.3 Additional Terms in the Momentum Equation

In chapter two, the governing equations of mass continuity and momentum were derived in full, from these derivations a potential source of error is identified which is neglected in the conventional SPH equations. If the continuity equation is met exactly, then equation (2.19) also holds exactly, however if the opposite is true, then for momentum to be conserved an extra term must be added, in-fact the equation is now (2.27) or in terms of the material derivative:

$$\rho\left(\frac{Dv}{Dt}\right) = \nabla\cdot\sigma - v\left(\frac{\partial\rho}{\partial t} + \rho(\nabla\cdot v)\right) \qquad (6.1)$$

The equation above basically states that momentum must be corrected with the discrepancy in the mass calculation. Clearly the two terms, $\frac{\partial \rho}{\partial t}$ and $\rho(\nabla \cdot v)$ as stated before are equal in continuous form but to make the correction in the SPH method this term must be implemented carefully in order to ensure that the discrete equations correctly mimic the continuous form.

6.4 SPH Implementation

The SPH implementation of the correction term outlined above will make use of both forms of density estimation, Summation form (6.3) and the continuity approximation (6.2), as well as a simple backward difference formula.

$$\langle \frac{\partial \rho}{\partial t} \rangle_i = \sum_j^{nnbr} (v_j - v_i) \nabla W_{ij} \frac{m_j}{\rho_j} \tag{6.2}$$

$$\langle \rho \rangle_i = \sum_j^{nnbr} (m_j) W_{ij} \tag{6.3}$$

$$\frac{\partial \langle \rho \rangle_i}{\partial t} = \frac{\langle \rho \rangle_i{}^n - \langle \rho \rangle_i{}^{n-1}}{\Delta t} \tag{6.4}$$

With these definitions it is possible to re-write the SPH momentum equation to account for the extra terms

$$\langle \frac{Dv_i}{Dt} \rangle = \sum_j^{np} m_j \left(\frac{\sigma_i}{\rho_i^2} + \frac{\sigma_j}{\rho_j^2} \right) \nabla W_{ij} - v_i \left(\frac{\partial \langle \rho_i \rangle}{\partial t} + \rho_i \langle \frac{\partial \rho}{\partial t} \rangle_i \right) \tag{6.5}$$

In (6.5) all variable are at time n, except for the density at n-1 which is contained within the backwards difference formula.

There are clearly many ways to account for this extra term, however this implementation is considered the most simple and straightforward to implement, noting that the backwards difference formula is inherently stable.

6.5 Numerical Results

Two benchmark tests are used to test the SPH implementation of (6.5), the tests are described in chapter three, and identical parameters are used to achieve the results in this section. The Swegle test provides a basic test for stability and the second problem tests both stability and whether the correction to the continuity affects mechanical response.

6.5.1 Swegle Test

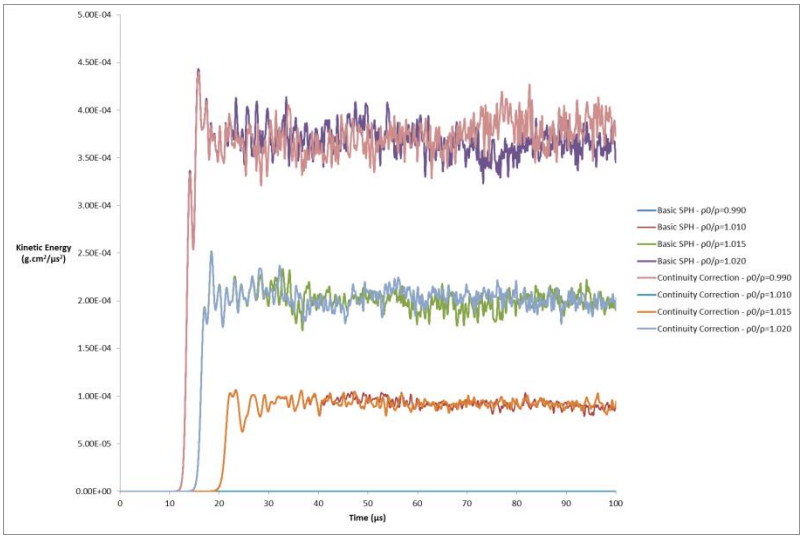

Figure 6-2 *Swegle Test Case for Various Levels of Stress, Basic SPH vs. SPH with Continuity Correction*

6.5.2 2D Plane Strain Elastic Impact

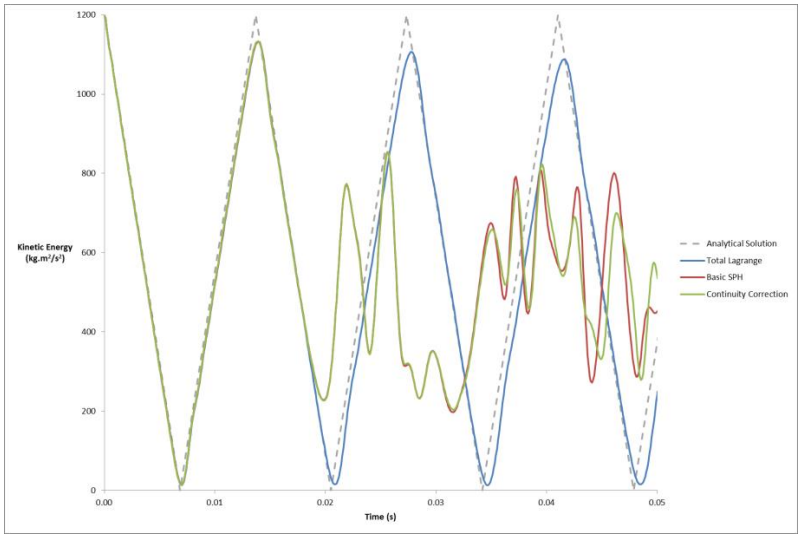

Figure 6-3 *2D Plane Strain Problem, Elastic Impact at 2m/s*

6.6 Conclusions

A potential source of error was identified in the discrete continuity equation, which meant that the discrete SPH form does not correctly mimic the behaviours of the continuous form; a correction term was added to the momentum equation to account for this, whilst still allowing the SPH continuity equation to be used to evolve the density. A number of different implementations would be possible but only one is implemented and tested in the MCM code. The test cases show that the effect of the correction term is very small, for the Swegle test this is because the different forms of the density calculation give very similar results; however it clearly does have a small effect but not enough to significantly affect the growth rate of the instability. Similar results are seen with the 2D plane strain problem, the mechanical behaviour of the problem is not affected and only a small difference is observed in the kinetic energy. A possible reason for the effect of the correction term being so small is that the growth rate is related to the level of background stress in the problem [44], however the correction term is only a function of density and velocity.

In summary, the objective defined in §1.4.2 has been completed, in which the question was raised as to whether stability is related to the properties of conservation and continuity, after the current study is completed the conclusion can be made that; for the selected test cases, and the specific choice of discrete equation implemented, there does not appear to be a significant improvement in the stability properties of the SPH method.

7 Corrections on Interpolation Errors in SPH

7.1 Introduction

It is well understood that the conventional form of SPH suffers from issues regarding consistency and accuracy as discussed in chapter three; in particular the conventional SPH method cannot approximate the gradient of a constant non-zero field. Therefore it can be said that the discrete approximation of the governing equations does not properly mimic the properties of the continuous equations.

$$\langle \frac{Dv}{Dt} \rangle = -\sum_{j}^{np} m_j \left(\frac{\sigma_j}{{\rho_j}^2} + \frac{\sigma_i}{{\rho_i}^2} \right) \nabla W_{ij} \tag{7.1}$$

The common form of the SPH momentum equation is shown again here (7.1) and for a derivation refer to chapter two. This form of the momentum equation is reliant of the approximation of the gradient of a constant field, which approximated correctly should always be zero. It is not understood properly why this form of the momentum equation often yields better results, for a full discussion see chapter three.

Equation (7.1) includes the following term (7.2):

$$\sum_{j}^{np} \left(\frac{\sigma_i}{{\rho_i}^2} \right) \nabla W_{ij} = \left(\frac{\sigma_i}{{\rho_i}^2} \right) \sum_{j}^{np} \phi \nabla W_{ij} \tag{7.2}$$

Where ϕ is an arbitrary constant.

This term should equate to zero, this is true if the particle are distributed evenly, however if they are not then it is observed that an erroneous gradient field results from the calculation. In the case of the momentum equation this erroneous gradient field is scaled by the term outside the summation $\frac{\sigma_i}{{\rho_i}^2}$. Therefore the approximation of the divergence of the stress is now a function of the magnitude of the stress as well as the gradient, which is not physically correct. In other words, in the continuous momentum equation, the choice of ϕ is not important since its gradient will always yield zero. It has been noted in [90] that the choice of this constant function ϕ in the discrete SPH equations is not yet fully understood, since a form of the SPH equations derived rigorously does not exist.

This issue is identified a potentially route towards the development of a stable SPH method and understanding the source of the current issues surrounding stability that occur in the SPH method. In chapter three it was noted that Swegle [12], found that the growth of the instability was dependant on the magnitude of the stress in the problem. It appears that a link exists between the conclusions of Swegle and the erroneous gradient field that occurs due to SPH approximation of a gradient of a constant field, i.e. the error that is introduced by (7.1).

The objective therefore is to provide an investigation into the effect of (7.1) on the stability of the SPH method, leading toward a rigorous derivation of the SPH equations, and in improved understanding of any stability criteria.

7.2 Numerical Examples in 1D

An example of the effect of an irregular particle distribution on gradient field is demonstrated in Figure 7-1 to Figure 7-4 which depicts a simple 1D SPH approximation of constant fields and the effect of (7.2) on the interpolation of a gradient.

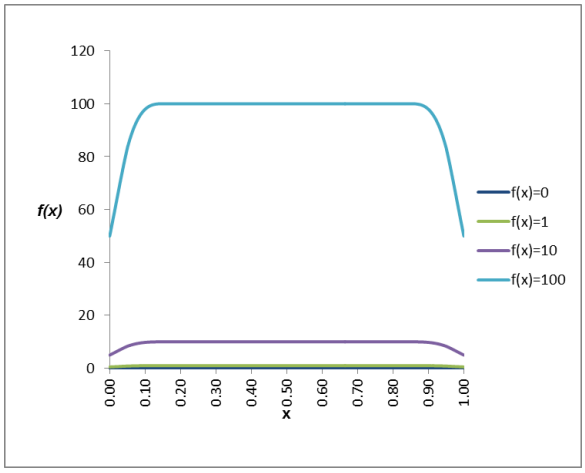

Figure *7-1 SPH Approximation of Constant Functions with Regularly Spaced Particles*

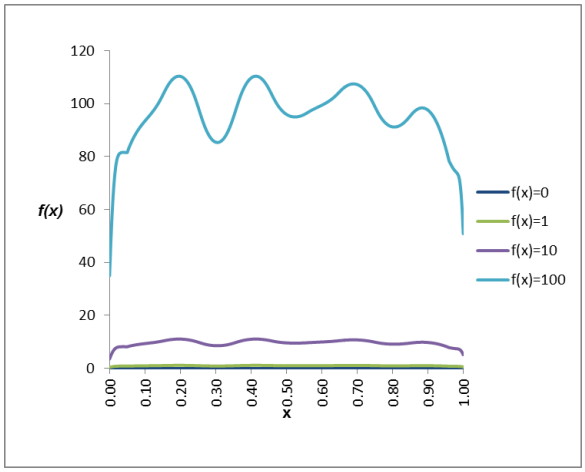

Figure *7-2 SPH Approximation of Constant Functions with Irregularly Spaced Particles*

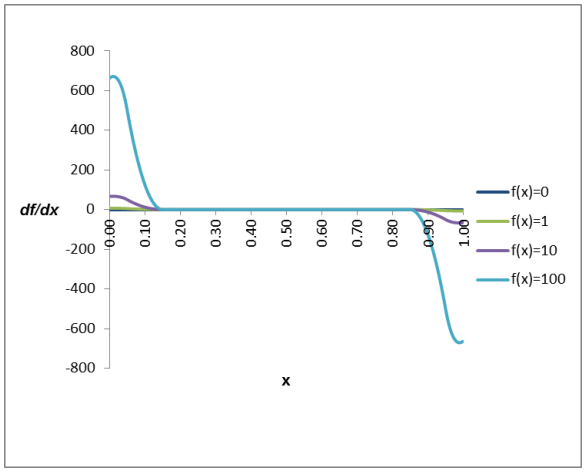

Figure *7-3 SPH Approximation of the Gradient of a Constant Functions with Regularly Spaced Particles*

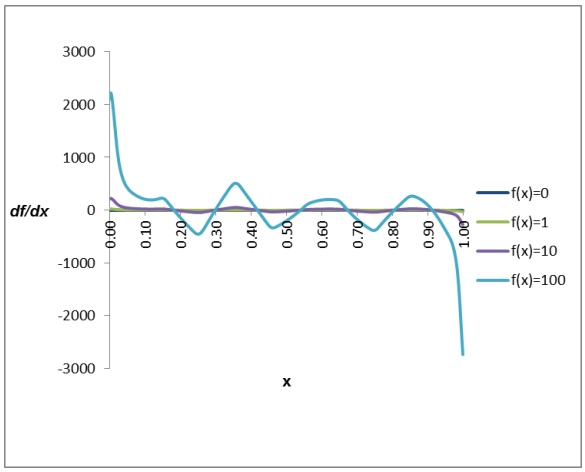

Figure *7-4 SPH Approximation of the Gradient of a Constant Functions with Irregularly Spaced Particles*

These examples (Figure 7-1 to Figure 7-4) demonstrate the effect of a non-uniform particle distribution has on the calculation of the gradient field. When the spacing of the particles is even the function and its gradient are calculated correctly except at boundaries due to an incomplete neighbourhood. When the particles are perturbed slightly however, errors develop and the solution begins to oscillate, this effect increases as the value of the constant, ϕ is increased.

The remainder of this chapter focuses on minimising the error in this calculation and investigating the impact on stability.

7.3 A Modified SPH Form

In this section the SPH momentum equation is derived in such a way that the calculation is not dependent on the magnitude of the stress field, and therefore the error introduced by the approximation of the constant part of the equations will not arise, this modified form of the governing equations is then implemented in the MCM code and assessed on its effect on the stability of the method.

Starting from the continuous momentum equation

$$\frac{Dv}{Dt} = \frac{\nabla \cdot \sigma}{\rho} \tag{7.3}$$

Integrate over the volume and multiply by a smoothing function

$$\int_{\Omega} \frac{Dv}{Dt} W(x - x', h) = \int_{\Omega} \frac{\nabla \cdot \sigma}{\rho} W(x - x', h) d\Omega \tag{7.4}$$

Integrate by parts and disregard boundary terms

$$\langle \frac{Dv}{Dt} \rangle = - \int_{\Omega} \frac{\sigma}{\rho} \cdot \nabla W(x - x', h) d\Omega \tag{7.5}$$

Write as SPH particle summation

$$\langle \frac{Dv}{Dt} \rangle = -\sum_{j}^{nnbr} m_j \frac{\sigma_j}{\rho_j^2} \cdot \nabla W_{ij} \tag{7.6}$$

Split $\frac{\sigma_j}{\rho_j^2}$ into its mean and fluctuating parts.

$$\langle \frac{Dv}{Dt} \rangle = -\sum_{j}^{nnbr} m_j \left[\overline{\left(\frac{\sigma_J}{\rho_J^2} \right)} + \widetilde{\left(\frac{\sigma_J}{\rho_J^2} \right)} \right] \cdot \nabla W_{ij} \tag{7.7}$$

The mean part is constant over the neighbourhood and therefore has no gradient.

$$\langle \frac{Dv}{Dt} \rangle = -\sum_{j}^{nnbr} m_j \widetilde{\left(\frac{\sigma_J}{\rho_J^2} \right)} \cdot \nabla W_{ij} \tag{7.8}$$

Therefore it should be sufficient to only interpolate the fluctuating part, however this value is not known directly and must be calculated:

$$\frac{\sigma_j}{\rho_j^2} - \overline{\left(\frac{\sigma_\iota}{\rho_\iota^2} \right)} = \widetilde{\left(\frac{\sigma_J}{\rho_J^2} \right)} \tag{7.9}$$

Leaving:

$$\langle \frac{Dv}{Dt} \rangle = -\sum_{j}^{nnbr} m_j \left[\frac{\sigma_j}{\rho_j^2} - \overline{\left(\frac{\sigma_\iota}{\rho_\iota^2} \right)} \right] \cdot \nabla W_{ij} \tag{7.10}$$

Where $\overline{\left(\frac{\sigma_\iota}{\rho_\iota^2} \right)}$ is the averaged portion of this term, this leaves a choice in the averaging procedure, the most simple option would be to use the un-weighted average over the neighbourhood with its centre at particle i .

$\widetilde{\left(\frac{\sigma_J}{\rho_J^2} \right)}$ is the fluctuating portion of the term. This essentially means that the error brought about by the interpolation of the mean part of the stress is removed; effectively this should provide an approximation equivalent to using a regular particle distribution.

7.3.1 Conservation of Linear Momentum

In order to conserve linear momentum, symmetry must be preserved between particle pairs (see §3.5). In other words for a particle pair, the forces between them must be equal and opposite.

For a pressure difference form of the momentum equation, taking a single particle pair and multiplying through by the mass as $F = ma$.

$$F_{ij} = -m_i m_j \left[\frac{\sigma_j}{\rho_j^2} - \frac{\sigma_i}{\rho_i^2}\right] \cdot \nabla W_{ij} \tag{7.11}$$

Exchanging the i and j components must produce an equal and opposite force to conserve linear momentum, such that:

$$-F_{ij} = F_{ji} = m_i m_j \left[\frac{\sigma_j}{\rho_j^2} - \frac{\sigma_i}{\rho_i^2}\right] \cdot \nabla W_{ij} \tag{7.12}$$

Starting with (7.11) and swapping the components:

$$F_{ji} = -m_j m_i \left[\frac{\sigma_i}{\rho_i^2} - \frac{\sigma_j}{\rho_j^2}\right] \cdot \nabla W_{ji} \tag{7.13}$$

Re-arranging gives:

$$-m_i m_j \left[-\frac{\sigma_j}{\rho_j^2} + \frac{\sigma_i}{\rho_i^2}\right] \cdot \nabla W_{ji} \tag{7.14}$$

Due to the anti-symmetric kernel gradient, $\nabla W_{ij} = -\nabla W_{ji}$:

$$m_i m_j \left[\frac{\sigma_j}{\rho_j^2} - \frac{\sigma_i}{\rho_i^2}\right] \cdot \nabla W_{ij} \tag{7.15}$$

As required to show symmetry between particle pairs. Therefore assuming that $\frac{\sigma_i}{\rho_i^2}$ is a reasonable choice of $\overline{\left(\frac{\sigma_i}{\rho_i^2}\right)}$ in (7.10), linear momentum is conserved.

7.3.2 Von Neumann Stability Analysis (Evenly Spaced Particles)

As mentioned previously, a number of stability analyses have been performed by various authors, including Von Neumann type analyses in 1D [12], [32], [49], [48]. The authors come to similar conclusions on the stability criteria and suggest optimal ranges for the smoothing length. Due to the relative simplicity, the stability analysis in this section will follow the analysis of Ferrari [49], who concludes that the conventional SPH method is unconditionally unstable.

$$\frac{Dv}{Dt} = \frac{\nabla \cdot \sigma}{\rho} \tag{7.16}$$

A similar procedure is followed here, now adopting a modified SPH approximation:

Considering the one dimensional linear advection equation

$$\frac{\partial u}{\partial t} + \frac{\partial f}{\partial \xi} = 0 \tag{7.17}$$

$$f(u) = au \tag{7.18}$$

Where a is some constant.

The SPH approximation of the derivative of a function can be written

$$\nabla f(\xi_i) = \sum_j^{np} (\tilde{f}_J) \nabla W_{ij} \frac{m_j}{\rho_j} \tag{7.19}$$

The gradient approximation of the function is only dependant on the fluctuation from the mean value of the field variable.

Applying the SPH approximation at a point ξ_i and advancing in time using an explicit forward Euler scheme

$$\frac{u_i^{n+1} - u_i^n}{\Delta t} + \sum_j^{np} (\tilde{f}_j^n) W_{ij} \frac{m_j}{\rho_j} = 0 \tag{7.20}$$

Leading to:

$$u_i^{n+1} = u_i^n - a\Delta t \sum_j^{np} (\tilde{f}_j^n) \nabla W_{ij} \frac{m_j}{\rho_j} \tag{7.21}$$

Assuming for the moment that the particles are distributed evenly, the usual Von Neumann method is followed, considering the following trial solution

$$u = u(t^n, \xi) = u_i^n e^{I(K\xi)} \tag{7.22}$$

Where k is the wavenumber

$$k = \frac{\phi}{\Delta\xi} \tag{7.23}$$

The modulus of the amplification factor is defined as

$$\left|\hat{A}_f\right| = \left|\frac{u_i^{n+1}}{u_i^n}\right| \tag{7.24}$$

Which for a stable solution procedure must remain less than one at all times.

$$\left|\hat{A}_f\right| \leq 1 \tag{7.25}$$

Substituting the trial solution into (7.21) and applying Von Neumann analysis we obtain

$$\frac{u_i^{n+1} - u_i^n e^{I(K\xi_i)}}{\Delta t} = \sum_j^{nnbr} \left(u_i^n e^{I(K\xi_j)}\right) \nabla W_{ij} \frac{m_j}{\rho_j} \tag{7.26}$$

Re-arranging gives:

$$u_i^{n+1} = u_i^n + \Delta t \sum_j^{np} \left(u_i^n e^{I(K\xi_j)}\right) \nabla W_{ij} \frac{m_j}{\rho_j} \tag{7.27}$$

Dividing through by u_i^n:

$$\frac{u_i^{n+1}}{u_i^n} = 1 + \Delta t \sum_j^{np} \left(\frac{u_i^n e^{I(K\xi_j)}}{u_i^n e^{I(K\xi_i)}} \right) \nabla W_{ij} \frac{m_j}{\rho_j} \tag{7.28}$$

Simplifying:

$$\frac{u_i^{n+1}}{u_i^n} = 1 + \Delta t \sum_j^{np} \left(e^{IK(\xi_j - \xi_i)} \right) \nabla W_{ij} \frac{m_j}{\rho_j} \tag{7.29}$$

Now, assuming that the particles are distributed evenly, the summation is performed in pairs as per Figure 7-5 and equation (7.30)

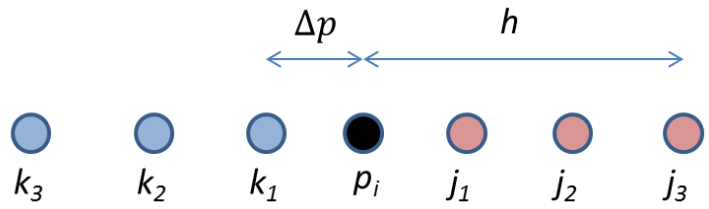

Figure *7-5 Domain of influence for 1D example*

$$\frac{u_i^{n+1}}{u_i^n} = 1 + \Delta t \left[\sum_{j=1}^{nnbr/2} \left(e^{IK(\xi_j - \xi_i)} \right) \nabla W_{ij} \frac{m_j}{\rho_j} + \sum_{k=1}^{nnbr/2} \left(e^{IK(\xi_k - \xi_i)} \right) \nabla W_{ik} \frac{m_k}{\rho_k} \right] \tag{7.30}$$

Noting that $(\xi_j - \xi_i) = -(\xi_k - \xi_i)$ and $\nabla W_{ik} \frac{m_k}{\rho_k} = -\nabla W_{ij} \frac{m_j}{\rho_j}$ assuming equally spaced particles, the summation can be performed over only one half of the domain.

$$u_i^{n+1} = 1 + \Delta t \left[\sum_{j=1}^{nnbr/2} \left(e^{IK(\xi_j - \xi_i)} - e^{-IK(\xi_j - \xi_i)} \right) \nabla W_{ij} \frac{m_j}{\rho_j} \right] \tag{7.31}$$

$$e^{IK(\xi_j - \xi_i)} - e^{-IK(\xi_j - \xi_i)} = 2isin\left(K\left(\xi_j - \xi_i \right) \right) \tag{7.32}$$

Leaving

$$u_i^{n+1} = 1 + 2\Delta t \left[\sum_{j=1}^{nnbr/2} \left(isin(K(\xi_j - \xi_i)) \right) \nabla W_{ij} \frac{m_j}{\rho_j} \right] \tag{7.33}$$

Referring back to (7.24) and (7.25), the following condition must hold so that the error does not grow unbounded as time advances.

$$\left| 1 + 2\Delta t \left[\sum_{j=1}^{nnbr/2} \left(isin(K(\xi_j - \xi_i)) \right) \nabla W_{ij} \frac{m_j}{\rho_j} \right] \right| < 1 \tag{7.34}$$

$$-1 \leq 1 + 2\Delta t \left[\sum_{j=1}^{nnbr/2} \left(isin(K(\xi_j - \xi_i)) \right) \nabla W_{ij} \frac{m_j}{\rho_j} \right] \leq 1 \tag{7.35}$$

The term inside the summation in (7.35) is purely imaginary, since the bounds of the inequality are real numbers, the only way the inequality can be true is if

$$isin(K(\xi_j - \xi_i)) = 0 \tag{7.36}$$

Which will be true if

$$sin\left(K(\xi_j - \xi_i)\right) = 0 \tag{7.37}$$

Which will be true only when the term inside the brackets is a multiple of π (since $\sin(N\pi) = 0\,, \forall N$)

The point at which the error term will grow the quickest is when the wavelength is shortest. The wavenumber, $K = \frac{2\pi}{\lambda}$, where λ is the wavelength; the shortest possible wavelength that can be resolved numerically is twice the particle spacing $2(\xi_j - \xi_i)$

$$K(\xi_j - \xi_i) = \frac{2\pi(\xi_j - \xi_i)}{2(\xi_j - \xi_i)} = \pi \tag{7.38}$$

Therefore as long as the particle spacing is chosen such that $\frac{\lambda}{2} \leq (\xi_j - \xi_i)$ then the system is stable.

7.3.3 Von Neumann Stability Analysis (Unevenly Spaced Particles)

Now suppose that the particles are not positioned randomly, the stability regime will look the same as above but with the additional term

$$-1 \leq \left[1 + 2\Delta t \left(\sum_{j=1}^{\frac{nnbr}{2}} \left(isin(K(\xi_j - \xi_i)) \nabla W_{ij} \frac{m_j}{\rho_j} \right) \right] - \left[\sum_{j=1}^{nnbr} \nabla W_{ij} \frac{m_j}{\rho_j} \right] \leq 1 \qquad (7.39)$$

In which the term that arises from the particle disorder must be removed as per (7.10) ; The approximation of a gradient of a constant function. Assume the stability criterion for the first term is satisfied, and only the additional term needs to be examined:

$$-1 \leq -\left[\sum_{j=1}^{nnbr} \nabla W_{ij} \frac{m_j}{\rho_j} \right] \leq 1 \qquad (7.40)$$

Taking the absolute value of (7.40):

$$0 \leq \left| \sum_{j=1}^{nnbr} \nabla W_{ij} \frac{m_j}{\rho_j} \right| \leq 1 \qquad (7.41)$$

7.3.4 Analogy to the SPH Momentum Equation

The stability criteria for this term can be summarised as follows;

If (7.41) holds, the error term is small enough so that the solution does not grow unbounded in time, and the modified form of the SPH equations can be used to approximate the gradient. (7.1)

If (7.41) does not holds, the error term will cause unstable growth as time advances, and the modified SPH form is not appropriate.

7.3.5 Summary

The SPH momentum equation has been derived rigorously which results in a form that does not introduce additional error terms into the solution, correctly mimicking the continuous form of the governing equations, a Von Neumann stability analysis demonstrated that the conventional SPH is only stable when certain criteria are met, relating to the particle spacing, when this criteria is not met the modified form derived in this chapter must be used to prevent the solution from developing errors that grow unbounded as time advances.

7.4 SPH Implementation

The test cases introduced in chapter three are used here to examine the stability properties of the new modified SPH equation derived in this chapter, firstly (7.10) is implemented and the stability regime is ignored for the initial tests.

The modified form of the momentum equation is defined as :

$$\langle \frac{Dv}{Dt} \rangle = -\sum_{j}^{nnbr} m_j \left[\frac{\sigma_j}{\rho_j^2} - \overline{\left(\frac{\sigma_\iota}{\rho_\iota^2} \right)} \right] \cdot \nabla W_{ij} \qquad (7.42)$$

Where the term averaged term is initially defined as the un-weighted average over the neighbourhood of the term $\overline{\left(\frac{\sigma_\iota}{\rho_\iota^2} \right)}$. This is calculated using

$$\overline{\left(\frac{\sigma_\iota}{\rho_\iota^2} \right)} = \frac{1}{nnbr+1} \left[\sum_{j=1}^{nnbr} \frac{\sigma_i}{\rho_i^2} + \frac{\sigma_i}{\rho_i^2} \right] \qquad (7.43)$$

Note that the summation is divided by the number of neighbouring particles plus one, this is because the average over the field is also dependant on the i particle itself.

The first problem used to investigate the new set of equations is the test developed by Swegle [12] which was introduced in chapter three, in which a 2D domain of hydrostatic fluid is initially in tension, that is to say its relative volume is greater than one. A particle is then given a very small perturbation which should not excite any particle motion, however for the basic SPH form; the instability develops and exhibits an unphysical particle motion.

7.4.1 Swegle Test

As usual, the instability growth is examined via the growth of kinetic energy in the domain.

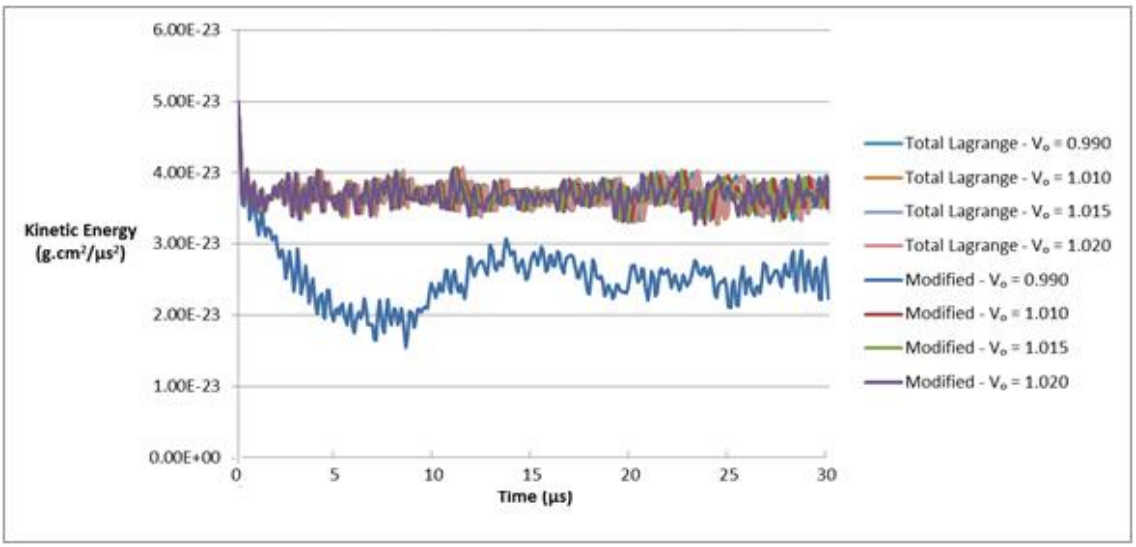

Figure *7-6– The modified momentum equation exhibits stable behaviour under compression and tension*

In the simple test case demonstrated above, the use of a modified momentum equation removes the instability from the problem, no unphysical particle motion is observed and the kinetic energy mimics the stable total Lagrange solution.

7.4.2 2D Plane Strain Impact

The second test case, also introduced in chapter three, for the 2D plane strain problem of the impact of two elastic blocks, is investigated in order to assert whether the mechanics of a problem can be preserved using this modified implementation

The initial test breaks down soon after the problem begins to advance in time, closer examination shows it is the free boundaries that are first to exhibit unstable behaviour, this result is consistent with the stability criterion (7.41), since the incomplete domain at the boundary causes this term to grow. This result is also consistent with momentum equations based on a pressure difference form, since for a for a uniform stress field it relies on the stress contribution for the i and j particles cancelling out, so that the gradient of a uniform stress field is calculated correctly, at the boundaries this is not possible.

This was not observed in the Swegle test case since the boundaries are made up of constrained SPH particles, so the domain of influence in the SPH interpolation is always complete for the region of interest.

The results in Figure 7-7 show the outcome of a slightly modified test case, where symmetry planes are defined to surround the two elastic blocks, essentially now the problem is a 2d semi-infinite bar. It is clear now from Figure 6 that the modified SPH form is stable when the stability criterion (7.41) is met.

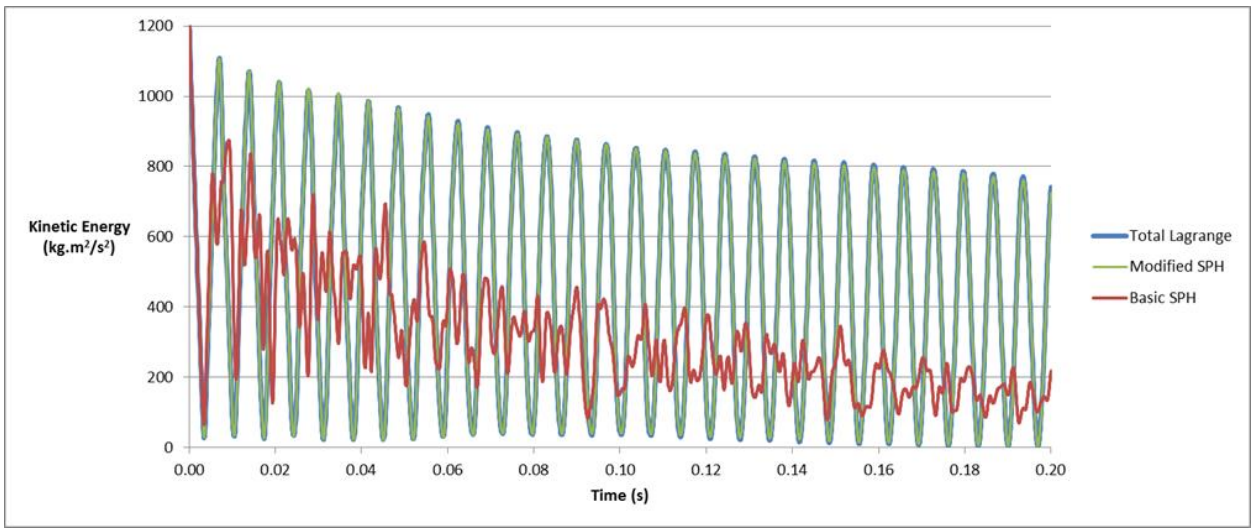

Figure *7-7- Modified SPH showing stable behaviour when all boundaries are constrained.*

7.4.3 Optimal Implementation

Although the modified form of the SPH equation are stable under certain regimes, it is a severe restriction if the method breaks down at free boundaries, therefore an implementation is tested based on the stability criterion (7.41). If this criterion is met, then the modified form (7.10) is used to calculate acceleration, however if the criterion is not met, the standard form (7.1) is used instead. Typically this will mean the modified form is used throughout the domain and the standard form will be used at boundaries, although this does not mean that the position of free boundaries needs to be defined, only the value of the term:

$$\left| \sum_{j=1}^{nnbr} \nabla W_{ij} \frac{m_j}{\rho_j} \right| \qquad (7.44)$$

The value of the term (7.41) is used to determine the point at which the switch occurs between the conventional SPH momentum equation and the modified form derived in this chapter. It is assumed that it is appropriate to represent the averaged term $\overline{\left(\frac{\sigma_i}{\rho_i^2}\right)}$ simply by the value at the i particle itself, i.e. $\overline{\left(\frac{\sigma_i}{\rho_i^2}\right)} \approx \frac{\sigma_i}{\rho_i^2}$, thus preserving symmetry and conserving linear momentum, see §7.3.1

7.4.4 Numerical Results

A quick re-run of the Swegle test confirms that the solution is still stable when a switch is in place between the two forms of the momentum equation. The 2D plane strain problem is then repeated as described in chapter three, where the boundaries are the top and bottom of the domain are left free, the solution appears not to exhibit any unstable growth in time, and mimics the total Lagrange solution closely.

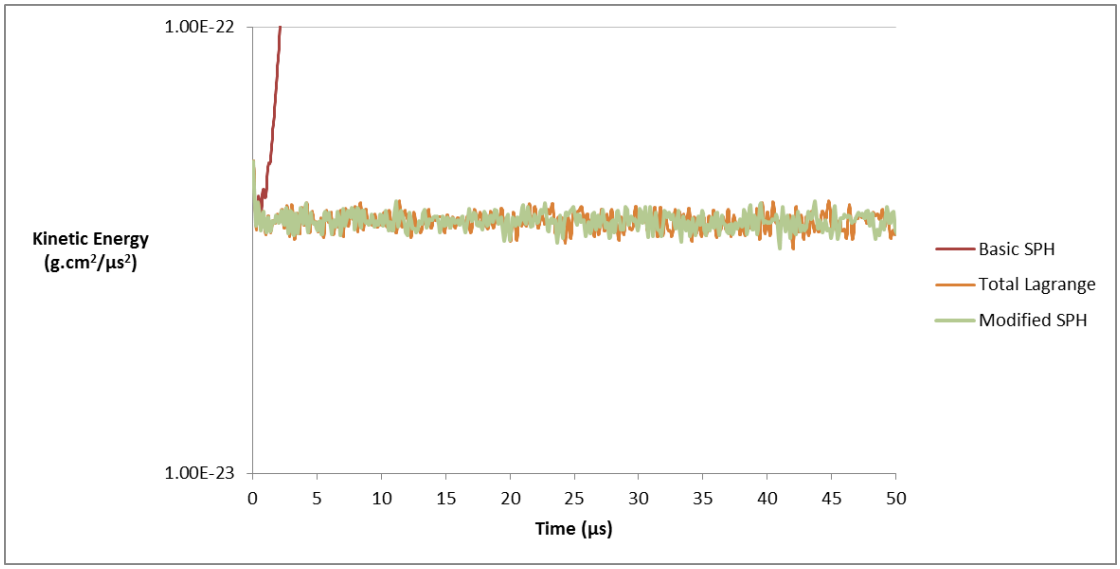

Figure *7-8 - Swegle Test for the Modified SPH Form*

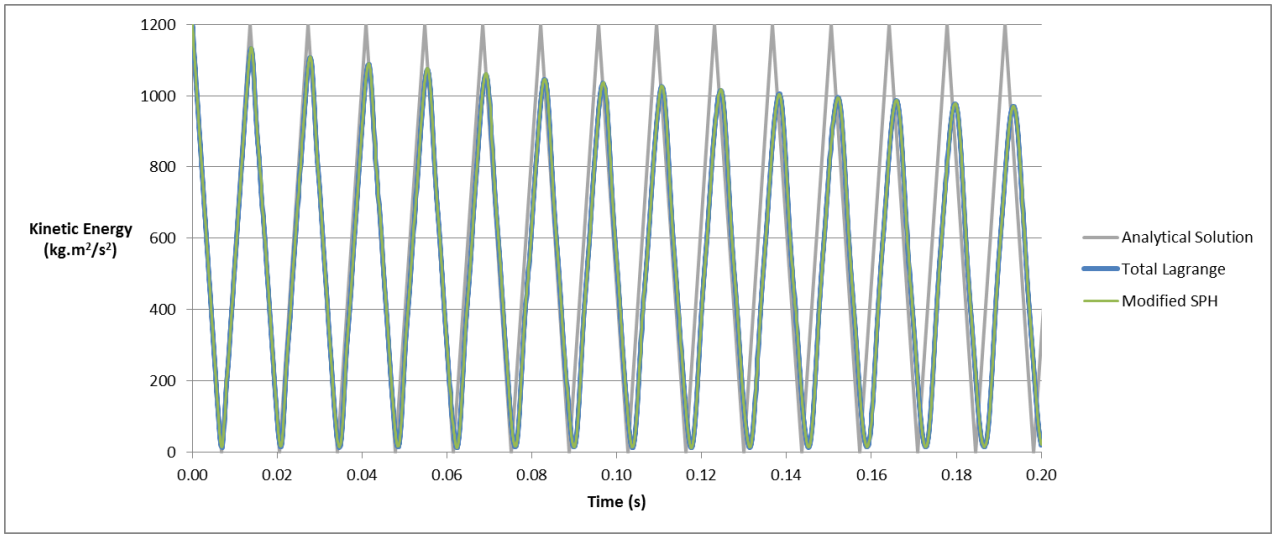

Figure *7-9 - 2D Plane Strain Problem using SPH Form Based on Stability Criterion*

7.5 Conclusions

For the test problems identified in chapter three, the Swegle test and the 2D plane strain problem, the modified SPH form appears not to cause unstable growth in the solution for the parameters tested in this chapter. These results suggest that the instability could be directly related to the magnitude of the background stress as Swegle [12] also concluded; this in turn suggests that this instability is related to the choice of ϕ in (7.2), and since the conventional SPH form is unable to approximate a constant gradient field correctly for particles that are not spaced evenly. The error term that arises due to this erroneous gradient approximation has been studied and a modified SPH form has been derived rigorously which naturally removes this error term and a stability criterion is provided which also confirm that a stable solution requires a relatively regular particle distribution for this modified SPH. An optimal solution appears to require a switch between this modified form and the standard form, however the stability properties of the standard form are still not well understood, but for the problems tested it seems to be adequate when the stability criterion of the modified SPH form is not met which is mainly at free boundaries.

Objective §1.4.3 is addressed here, resulting in an improved understanding of the assumptions that are made in the standard derivations of the SPH momentum equation. To summarise, the derivation in §2.2.5 relies on the correct approximation of a constant

function, in certain circumstances it is appropriate to remove the error of this approximation as per the stability criterion (7.44), which can be achieved naturally through use of the modified SPH momentum equation derived in this chapter.

8 Mixed Methods in SPH

As outlined in chapter three, the use of mixed element methods can lead to significantly improved results in finite element methods, and can alleviate a number of issues with the basic formulations. There is a question as to whether mixed element methods can offer advantages when adapted to work in an SPH framework.

Firstly, the background of the mixed method and the reasons for using these methods in the finite element approach will be discussed.

Mixed element methods were first established in the 1960's and used to describe a finite element method in which both stress and displacement fields are treated as primary or independent variables [91], as opposed to only displacements as in the classical finite element method. In general, mixed element methods have shown a significant improvement over displacement based methods in a number of scenarios; Improved approximations of pressure have been observed [92] [93], and improved modelling of fluids has been achieved using a mixed pressure-displacement form of the finite element methods [94]. Studies of stability of mixed methods have been published [91] showing that stability can be achieved even for elements of low order, which leads to the most common reasons for the use of mixed element methods, which is avoid the hourglass modes that are common in finite element methods when using a displacement based approach in conjunction with under-integrated elements. Detailed analyses of mixed methods have been published in [95].

8.1 Hourglass Modes in FEM

Volumetric locking is used to describe the situation in which the displacements are under predicted by large factors [59], which occurs because of the use of fully integrated elements. Volumetric locking is often observed for incompressible or nearly incompressible materials. Shear locking on the other hand will occur when elements are subject to bending, and the stiffness of the structure is significantly over predicted, again displacements becoming significantly under-predicted.

The over-estimation of stiffness in these problems that exhibit locking can generally be avoided by the reducing the number of integration points in the element. This method can

reduce the accuracy of the solution but does avoid the locking problems that can prevent convergence.

The use of under-integrated elements however can lead to hourglass modes where the stiffness matrix becomes zero [96], leading to unphysical motion under zero strain. Analogies can be made between hourglass modes in FEM and zero-energy type instabilities in SPH [14].

Reviews of hourglass modes along with detailed descriptions of locking phenomena can be found in most books on finite element theory, in particular [57] [59].

Mixed element technology can be used to avoid hourglass modes by allowing the elements to be fully integrated, whilst also avoiding problems with locking. An example of how the mixed element method can be used in FEM is provided in a simple example in §8.3.1

The advantages of mixed element methods in FEM in constructing stable elements lead to the method being identified as a potential route towards a stable SPH method if the same methods can be adapted successfully into an SPH framework.

The tensile instability is not yet fully understood but can be thought of as an error arising from the constitutive relationship resulting in an erroneous pressure, this leads on to a further question; can the constitutive relation be adapted to remove the instability but at the same time preserving the proper mechanics of the problem in question. The use of mixed element methods provides a potential route whereby the strong links between the dependant variables are weakened.

SPH offers flexibility in the way that variables are interpolated, a wide number of interpolating functions are available all with their strengths and weaknesses, and it has already been shown that using different interpolating functions in for the strain and stress calculations provides limited improvements. It is therefore logical to investigate possible corrections to the various interpolations. Corrections during the phase of acceleration such as Monaghans repulsive force [41] only appear to work in very limited situations. Corrections could be also made during the displacement and velocity phases of the problem, given that they are 90 degrees out of phase with one another, it could well mean that calculations in the velocity of displacement phases are driving the growth of the instability. One possible route would be to add artificial corrections such as artificial

viscosity, however since we are interested in more rigorous solutions, the mixed element methods may provide a solution whereby the links between the variables are weakened and therefore removing the source of the instability before it propagates through the solution in time.

8.2 Hu-Washizu Mixed Form

The Hu-Washizu principle is traditionally used to develop mixed finite element method, in which more than one field variable is interpolated independently of the others. The principle is named after the authors and was originally developed in 1955 [97] [98].

The Hu-Washizu principle provides the foundation of what is the most general of mixed methods, in which displacements, strains and stresses are evaluated independently of one another. The strong form of the equations contains the kinetic equations, i.e. the momentum equation, boundary conditions, the strain-displacement relation, and the constitutive relation.

The form presented in this chapter is written in terms of the rate of deformation and is the formulation found in [59], derived from the principle of virtual power. This form is well suited to non-linear problems where the strain rate is used conventionally rather than the strain; this explicit form is well suited to the SPH implementation.

The weak form of the Hu-Washizu principle implies the following governing equations, written in strong form:

$$\rho \dot{v}_i - \bar{\sigma}_{ij,j} - \rho b_i = 0 \text{ in } \Omega \qquad (8.1)$$

$$[\![\bar{\sigma}_{ij} n_j]\!] = 0 \text{ on } \Gamma \qquad (8.2)$$

$$\bar{t}_j - \bar{\sigma}_{ij} n_j = 0 \text{ on } \Gamma \qquad (8.3)$$

$$D_{ij}(\boldsymbol{v}) - \overline{D}_{ij} = 0 \text{ in } \Omega \qquad (8.4)$$

$$\sigma_{ij}(\overline{\boldsymbol{D}}) - \bar{\sigma}_{ij} = 0 \text{ in } \Omega \qquad (8.5)$$

Where these equations refer to: the conservation of momentum (8.1), interior continuity conditions (8.2), traction boundary conditions (8.3), strain displacement equation (8.4), and constitutive equation (8.5).

The full derivation of these equations starting from the weak form of the Hu-Washizu principle is given in the Appendix.

The over bar in the equations (8.4) and (8.5) shows that the variable is evaluated independently. In the above equations this means that the assumed rate of deformation and assumed stress are interpolated independently of the velocity field. $D_{ij}(\boldsymbol{v})$ and $\sigma_{ij}(\overline{\boldsymbol{D}})$ are the rate of deformation and stress tensor evaluated from the velocity field via the strain displacement and constitutive equations.

Figure 8-1 shows the relationship between the various field variables for a conventional displacement based analysis, each variable is calculated in turn, for example the nodal velocities are used to calculate the rate of deformation through the kinematic relations, this is then passed into the constitutive law to give a stress measure, which is then used in the equation for momentum balance in order to find the nodal accelerations. This is much the same as the explicit scheme used in typical SPH implementations (see §2.3.1).

Figure 8-2 shows how the variables are linked when the rate of deformation and the stress are evaluated independently of one another, now there is only a weak link between them, enforced by the conditions (8.4) and (8.5). The rate of deformation calculated from the nodal velocities is now equal to an assumed or interpolated rate of deformation; this assumption weakens the strong links between the nodal velocities and the strain rate. The same can be said of the stress and the constitutive relation.

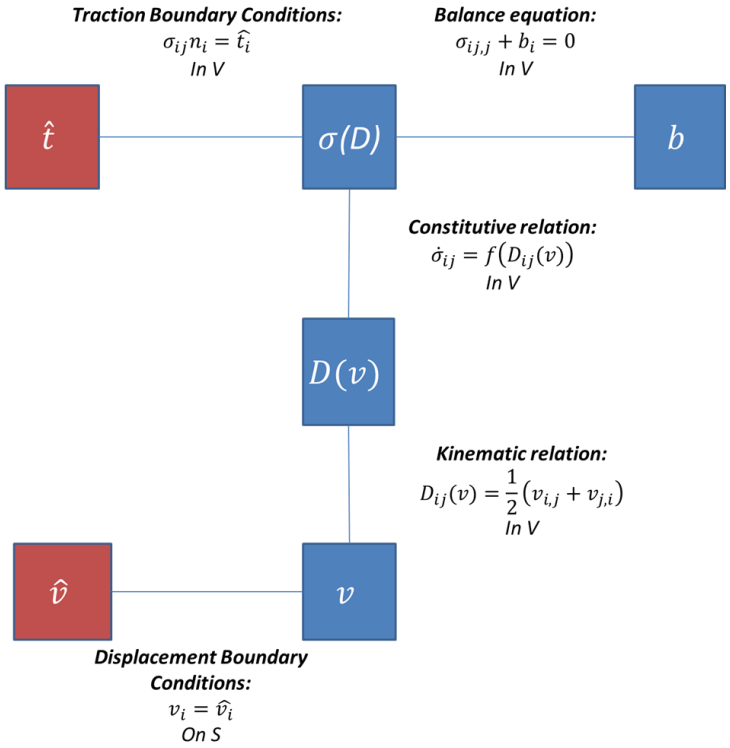

Figure *8-1 - Flow chart a displacement based analysis*

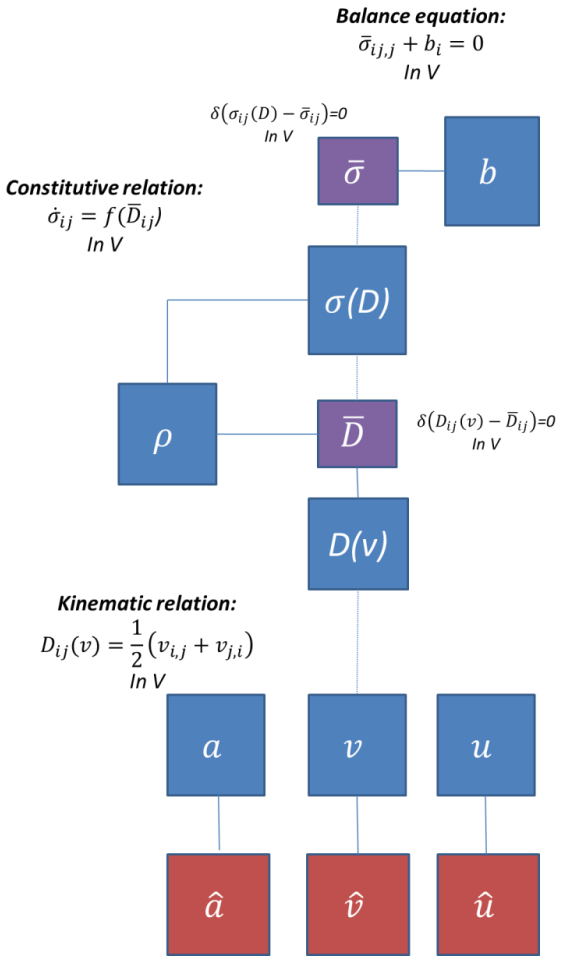

Figure *8-2 – Hu Washizu virtual power strong and weak links between variables*

The main difference in the two approaches is the addition of (8.4) and eq. (8.5) i.e. the constraints that now act on the rate of deformation and the stress. The remainder of this chapter will focus on the development of an SPH method which incorporates these additional constraints.

There are two potential routes that will be investigated, the discretisation of either the strong or the weak form. Discretising the strong form is the standard SPH approach and the method that was demonstrated in earlier in chapter two for the governing equations of mass and momentum, discretising the weak form is the method that is commonly applied in finite element methods.

Weak form – The equation is no longer required to hold absolutely and only has weak solutions with respect to some test function, this could mean that the equation is not required to hold at every point but only in an averaged or integral sense.

Strong form – The equation must hold at every point in the domain

8.3 Solution Procedure

In this section the weak form of the Hu-Washizu principle in written in SPH form, we see that this provides a complex set of equations and hence, a complicated implementation. Firstly the weak form will be discretised, using the finite element approach, which then in turn can be transformed in an SPH form using analogies for the FEM shape functions [56].

For a full description and derivation of the virtual power equations see [59], which results the the following equations being defined (a full derivation is also given in the appendix):

$$\{\tilde{\sigma}_C^e\} = \int_{\Omega_e} (\boldsymbol{N}_D)^T \{\boldsymbol{\sigma}(\bar{\boldsymbol{D}})\} d\Omega \tag{8.6}$$

$$\tilde{\boldsymbol{B}}_e = \int_{\Omega_e} \boldsymbol{N}_\sigma^T \boldsymbol{B} d\Omega \tag{8.7}$$

$$\boldsymbol{G}_e = \int_{\Omega_e} \boldsymbol{N}_\sigma^T \boldsymbol{N}_{\boldsymbol{D}} d\Omega \tag{8.8}$$

$\boldsymbol{N}$ is the element shape function with its subscript representing the interpolating function for either the stress tensor $\boldsymbol{\sigma}$, or the rate of deformation. $\bar{\boldsymbol{D}}$ is the rate of deformation tensor, with the over-bar representing an assumed or interpolated value. $\boldsymbol{B}$ is the strain displacement matrix and $d\Omega$ represents an infinitesimal volume element. Ω_e indicates the volume element itself.

8.3.1 1D Finite Element Example

The mixed element method is demonstrated in the following example which is taken from [59].

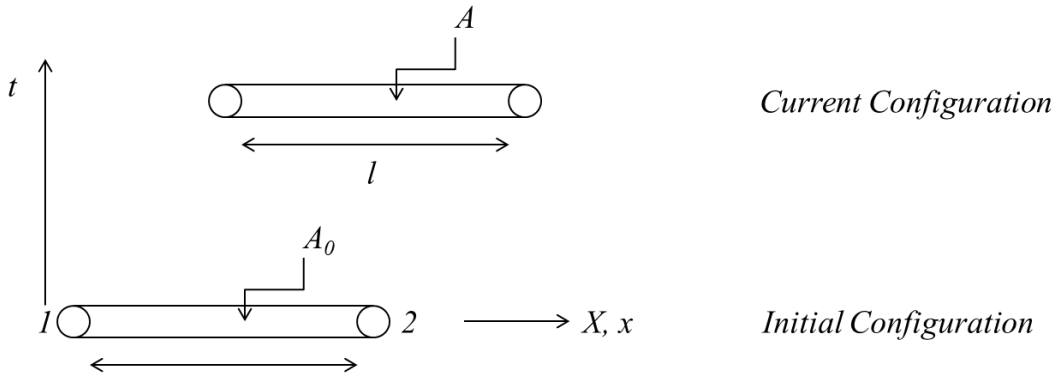

Figure *8-3 Configuration of 2-Node Rod Element*

To understand how the mixed method works in the finite element method, a simple example is presented:

Consider a two-node rod element, with the following properties:

Linear velocity

Constant velocity strain & stress

Area – A, length, l

The components of interest are the nodal velocity $v_x(\xi, t)$, the rate of deformation, $D_{xx}(\xi, t)$ and the stress $\sigma_{xx}(\xi, t)$. Where:

$$\xi = \frac{x}{l} = X = l_0 \tag{8.9}$$

The linear approximations for velocity, rate of deformation, and stress are:

$$v_x(\xi, t) = [1 - \xi, \xi] \begin{Bmatrix} v_{x1}(t) \\ v_{x2}(t) \end{Bmatrix} = \boldsymbol{N\dot{d}^e} \tag{8.10}$$

$$\overline{D}_{xx} = [1, \xi] \begin{Bmatrix} \alpha_1 \\ \alpha_2 \end{Bmatrix} = \boldsymbol{N_D \alpha} \tag{8.11}$$

$$\bar{\sigma}_{xx} = [1, \xi]\begin{Bmatrix}\beta_1 \\ \beta_2\end{Bmatrix} = \boldsymbol{N_\sigma \beta} \tag{8.12}$$

Where α and β, are unknowns. Next, writing the B Matrix as:

$$B = \frac{\partial}{\partial x}[N] = \frac{\partial}{\partial x}[1 - \xi, \xi] = \frac{1}{l}[-1,\ 1] \tag{8.13}$$

Writing $\tilde{B}$ (8.7) and G matrices (8.8)

$$\tilde{B} = \int_{\Omega_e} \boldsymbol{N_\sigma^T B} d\Omega = \int_0^1 \begin{Bmatrix}1 \\ \xi\end{Bmatrix} \frac{1}{l}\ [-1,\ 1] A l d\xi = \frac{A}{2}\begin{bmatrix}-2 & +2 \\ -1 & +1\end{bmatrix} \tag{8.14}$$

$$G = \int_{\Omega_e} \boldsymbol{N_\sigma^T N_D} d\Omega = \int_0^1 \begin{Bmatrix}1 \\ \xi\end{Bmatrix}\ [1,\ \xi] A l d\xi = \frac{Al}{6}\begin{bmatrix}6 & 3 \\ 3 & 2\end{bmatrix} \tag{8.15}$$

Inverting G:

$$\left(\frac{Al}{6}\begin{bmatrix}6 & 3 \\ 3 & 2\end{bmatrix}\right)^{-1} = \frac{2}{Al}\begin{bmatrix}2 & -3 \\ -3 & 6\end{bmatrix} \tag{8.16}$$

α can then be calculated from:

$$\alpha = G^{-1}\tilde{B}\dot{d} \tag{8.17}$$

$$\alpha = \begin{Bmatrix}\alpha_1 \\ \alpha_2\end{Bmatrix} = \frac{A}{2}\begin{bmatrix}-2 & +2 \\ -1 & +1\end{bmatrix}\frac{2}{Al}\begin{bmatrix}2 & -3 \\ -3 & 6\end{bmatrix}\begin{Bmatrix}v_{x1} \\ v_{x2}\end{Bmatrix} \tag{8.18}$$

Now $\overline{D}_{xx}$, the assumed rate of deformation can be calculated:

$$\overline{D}_{xx} = [1, \xi]\begin{Bmatrix}\alpha_1 \\ \alpha_2\end{Bmatrix} = \boldsymbol{N_D \alpha} \tag{8.19}$$

$\boldsymbol{\sigma_{xx}}(\overline{D}_{xx})$ can then be calculated through a constitutive relation; allowing the assumed stress to be calculated by first finding β.

$$\tilde{\boldsymbol{\sigma}} = \int_\Omega \begin{Bmatrix}1 \\ \xi\end{Bmatrix} \boldsymbol{\sigma_{xx}}(\overline{D}_{xx}) \mathrm{d}\boldsymbol{\Omega} \tag{8.20}$$

$$\beta = G^{-1}\tilde{\sigma} = \frac{2}{Al}\begin{bmatrix} 2 & -3 \\ -3 & 6 \end{bmatrix}\int_{\Omega} \begin{Bmatrix} 1 \\ \xi \end{Bmatrix} \boldsymbol{\sigma_{xx}}(\overline{D}_{xx})\mathrm{d}\boldsymbol{\Omega} \tag{8.21}$$

Finally the internal force can be calculated

$$\begin{aligned} f^{int} = \tilde{B}^T\beta &= \frac{A}{2}\begin{bmatrix} -2 & +2 \\ -1 & +1 \end{bmatrix}\frac{2}{Al}\begin{bmatrix} 2 & -3 \\ -3 & 6 \end{bmatrix}\int_{\Omega} \begin{Bmatrix} 1 \\ \xi \end{Bmatrix} \boldsymbol{\sigma_{xx}}(\overline{D}_{xx})\mathrm{d}\boldsymbol{\Omega} \\ &= \frac{1}{l}\begin{bmatrix} -1 & 0 \\ +1 & 0 \end{bmatrix}\int_{\Omega} \begin{Bmatrix} 1 \\ \xi \end{Bmatrix} \boldsymbol{\sigma_{xx}}(\overline{D}_{xx})\mathrm{d}\boldsymbol{\Omega} \end{aligned} \tag{8.22}$$

If stress is constant:

$$\begin{Bmatrix} f_{x1} \\ f_{x2} \end{Bmatrix} = \mathrm{A}\sigma_{xx}\begin{Bmatrix} -1 \\ +1 \end{Bmatrix} \tag{8.23}$$

This completes the example.

8.4 A Mixed SPH Framework

An SPH framework for the mixed formulation will now be developed from (8.6), (8.7), and (8.8).

This first requires the assumed rate of deformation, and assumed stresses to be defined; this will be done in the same way as in the finite element example:

$$\overline{D}_{ij} = \boldsymbol{N_D\alpha} \tag{8.24}$$

$$\bar{\sigma}_{ij} = \boldsymbol{N_\sigma\beta} \tag{8.25}$$

The subscripts in (8.24) and (8.25) represent the different shape functions that are used to interpolate the rate of deformation and the stress.

The element shape functions can be replaced by the SPH kernel function such that:

$$\boldsymbol{N} = \sum_{j=1}^{np} W_{ij}\frac{m_j}{\rho_j} \tag{8.26}$$

$$\boldsymbol{B} = \sum_{j=1}^{np} \nabla W_{ij} \frac{m_j}{\rho_j} \tag{8.27}$$

Therefore (8.6), (8.7) and (8.8) can be written respectively as

$$\int_{\Omega_e} \sum_{j=1}^{np} W_{ij} \frac{m_j}{\rho_j} \{\boldsymbol{\sigma}(\bar{\boldsymbol{D}})\} \, d\Omega \tag{8.28}$$

$$\int_{\Omega_e} \sum_{j=1}^{np} W_{ij} \frac{m_j}{\rho_j} \sum_{k=1}^{np} \nabla W_{ik} \frac{m_k}{\rho_k} d\Omega \tag{8.29}$$

$$\int_{\Omega_e} \sum_{j=1}^{np} W_{ij} \frac{m_j}{\rho_j} \sum_{k=1}^{np} W_{ik} \frac{m_k}{\rho_k} d\Omega \tag{8.30}$$

(8.24) and (8.25)can then be written:

$$\bar{D}_i = \sum_{j=1}^{nnbr} \alpha_j \frac{m_j}{\rho_j} \tag{8.31}$$

$$\bar{\sigma}_i = \sum_{j=1}^{nnbr} \beta_j \frac{m_j}{\rho_j} \tag{8.32}$$

The product of two summation terms in (8.29) and (8.30) can be written simply as a double summation, and the volume integral can approximation by a summation over the entire particle domain. i.e. (8.28) and (8.30) can be re-written:

$$\tilde{\boldsymbol{\sigma}} = \sum_{i=1}^{np} \left[\sum_{j=1}^{np} \{\boldsymbol{\sigma}(\bar{\boldsymbol{D}})\} W_{ij} \frac{m_j}{\rho_j} \right] \frac{m_i}{\rho_i} \tag{8.33}$$

$$\widetilde{\boldsymbol{B}} = \sum_{i=1}^{np}\left[\sum_{j=1}^{np}\sum_{k=1}^{np} W_{ik}\ \nabla W_{ij}\ \frac{m_k}{\rho_k}\frac{m_j}{\rho_j}\right]\frac{m_i}{\rho_i} \tag{8.34}$$

$$\boldsymbol{G} = \sum_{i=1}^{np}\left[\sum_{j=1}^{np}\sum_{k=1}^{np} W_{ik}\ W_{ij}\ \frac{m_k}{\rho_k}\frac{m_j}{\rho_j}\right]\frac{m_i}{\rho_i} \tag{8.35}$$

8.4.1 Solution Procedure

Now the SPH equations are established, a solution can be obtained.

Step one – Compute the assumed rate of deformation

By invoking arbitrariness of (11.41), the following expression is found

$$\widetilde{\boldsymbol{B}}_{\boldsymbol{e}}\dot{\boldsymbol{d}}_{\boldsymbol{e}} = \boldsymbol{G}_{\boldsymbol{e}}\boldsymbol{\alpha}_{\boldsymbol{e}} \tag{8.36}$$

Where $\boldsymbol{d}$ is the displacement and $\boldsymbol{\alpha}$ is an unknown.

The term on the left hand side can be calculated in SPH form using (8.34) replacing $\dot{\boldsymbol{d}}_{\boldsymbol{e}}$ with nodal velocities.

$$\widetilde{\boldsymbol{B}}_{\boldsymbol{e}}\dot{\boldsymbol{d}}_{\boldsymbol{e}} = \sum_{i=1}^{np}\left[\sum_{j=1}^{np}\sum_{k=1}^{np} \boldsymbol{v}_k W_{ik}\ \nabla W_{ij}\ \frac{m_k}{\rho_k}\frac{m_j}{\rho_j}\right]\frac{m_i}{\rho_i} \tag{8.37}$$

Writing $\sum_{k=1}^{np} \boldsymbol{v}_k W_{ik}$ as $\langle \boldsymbol{v} \rangle_{\boldsymbol{i}}$

$$\widetilde{\boldsymbol{B}}_{\boldsymbol{e}}\dot{\boldsymbol{d}}_{\boldsymbol{e}} = \sum_{i=1}^{np}\left[\sum_{j=1}^{np} \langle \boldsymbol{v} \rangle_{\boldsymbol{i}}\ \nabla W_{ij}\ \frac{m_j}{\rho_j}\right]\frac{m_i}{\rho_i} \tag{8.38}$$

Noting that the term inside the square brackets can be written as an inner product

$$\sum_{j=1}^{np} \langle \boldsymbol{v} \rangle_{\boldsymbol{j}} \, \nabla W_{ij} \frac{m_j}{\rho_j} = [\nabla W_{i,1} \quad \cdots \quad \nabla W_{i,np}] \begin{bmatrix} \langle v \rangle_1 \\ \vdots \\ \langle v \rangle_{np} \end{bmatrix} \tag{8.39}$$

The same can be done with the outer summation, leaving

$$\sum_{i=1}^{np} \left[\sum_{j=1}^{np} \langle \boldsymbol{v} \rangle_{\boldsymbol{i}} \, \nabla W_{ij} \frac{m_j}{\rho_j} \right] \frac{m_i}{\rho_i} = \begin{bmatrix} m_1/\rho_1 \\ \vdots \\ m_{np}/\rho_{np} \end{bmatrix} [\nabla W_{i,1} \quad \cdots \quad \nabla W_{i,np}] \begin{bmatrix} \langle v \rangle_1 \\ \vdots \\ \langle v \rangle_{np} \end{bmatrix} \tag{8.40}$$

The dimension of the above matrix expression are [np x 1] [1 x np] [np x 1] resulting in a vector with dimensions [np x 1].

Call the vector resulting from (8.40) V for simplicity.

$$V = \begin{bmatrix} \mathrm{V}_1 \\ \vdots \\ \mathrm{V}_{np} \end{bmatrix} \tag{8.41}$$

Repeat a similar procedure with the right hand side of (8.32)

$$\boldsymbol{G_e \alpha_e} = \sum_{i=1}^{np} \left[\sum_{j=1}^{np} \sum_{k=1}^{np} W_{ik} \, W_{ij} \frac{m_k}{\rho_k} \frac{m_j}{\rho_j} \right] \frac{m_i}{\rho_i} \boldsymbol{\alpha}_i \tag{8.42}$$

Leaving $\boldsymbol{\alpha}_i$ on the outside since it is unknown.

Simplifying slightly

$$\sum_{i=1}^{np} \left[\sum_{j=1}^{np} W_{ij} \frac{m_j}{\rho_j} \right] \frac{m_i}{\rho_i} \langle \boldsymbol{\alpha}_i \rangle \tag{8.43}$$

And writing in matrix form

$$\begin{bmatrix} W_{11} \frac{m_1}{\rho_1} \frac{m_1}{\rho_1} & \cdots & W_{1n} \frac{m_1}{\rho_1} \frac{m_{np}}{\rho_{np}} \\ \vdots & \ddots & \vdots \\ W_{n1} \frac{m_1}{\rho_1} \frac{m_{np}}{\rho_{np}} & \cdots & W_{nn} \frac{m_{np}}{\rho_{np}} \frac{m_{np}}{\rho_{np}} \end{bmatrix} \begin{bmatrix} \alpha_1 \\ \vdots \\ \alpha_{np} \end{bmatrix} \tag{8.44}$$

This finally results in a system of equations that needs to be solved for α

$$\begin{bmatrix} W_{11}\dfrac{m_1}{\rho_1}\dfrac{m_1}{\rho_1} & \cdots & W_{1n}\dfrac{m_1}{\rho_1}\dfrac{m_{np}}{\rho_{np}} \\ \vdots & \ddots & \vdots \\ W_{n1}\dfrac{m_1}{\rho_1}\dfrac{m_{np}}{\rho_{np}} & \cdots & W_{nn}\dfrac{m_{np}}{\rho_{np}}\dfrac{m_{np}}{\rho_{np}} \end{bmatrix} \begin{bmatrix} \alpha_1 \\ \vdots \\ \alpha_{np} \end{bmatrix} = \begin{bmatrix} \mathrm{V}_1 \\ \vdots \\ \mathrm{V}_{np} \end{bmatrix} \tag{8.45}$$

α can then be used to compute the assumed rate of deformation, by (8.54), which is essentially an SPH interpolation of **α**.

Step 2 – Compute stress

In this step the assumed rate of deformation is simply used in the normal constitutive relation to produce a stress term.

Step 3 – Compute assumed stresses

Solve (11.29 using the same process as for the assumed rate of deformation, which is the solution to the following system.

$$\begin{bmatrix} W_{11}\dfrac{m_1}{\rho_1}\dfrac{m_1}{\rho_1} & \cdots & W_{1n}\dfrac{m_1}{\rho_1}\dfrac{m_{np}}{\rho_{np}} \\ \vdots & \ddots & \vdots \\ W_{n1}\dfrac{m_1}{\rho_1}\dfrac{m_{np}}{\rho_{np}} & \cdots & W_{nn}\dfrac{m_{np}}{\rho_{np}}\dfrac{m_{np}}{\rho_{np}} \end{bmatrix} \begin{bmatrix} \beta_1 \\ \vdots \\ \beta_{np} \end{bmatrix} = \begin{bmatrix} \tilde{\sigma}_1 \\ \vdots \\ \tilde{\sigma}_{np} \end{bmatrix} \tag{8.46}$$

Step 4 – Compute acceleration

Replace the stress tensor in the standard SPH momentum equation with the assumed stress tensor and use this to move the particles.

8.4.2 Discussion

After implementing the above, a difficulty arose in achieving a solution to the system of equations, because of a fundamental (but not so obvious) problem which on closer inspection comes from the fact that the matrix is formed from an outer product of two vectors. Knowledge of linear algebra tells us that a matrix formed in this way will always have a rank of one, and therefore cannot be inverted. This can be demonstrated easily:

For any two vectors, of arbitrary size.

$$\boldsymbol{A} = \begin{bmatrix} \mathrm{a}_1 \\ \vdots \\ \mathrm{a}_n \end{bmatrix}, \boldsymbol{B} = \begin{bmatrix} \mathrm{b}_1 \\ \vdots \\ \mathrm{b}_n \end{bmatrix} \tag{8.47}$$

An outer product can be written, $\boldsymbol{A} \times \boldsymbol{B}$

$$A \times B = \begin{bmatrix} a_1 b_1 & \cdots & a_1 b_n \\ \vdots & \ddots & \vdots \\ a_n b_1 & \cdots & a_n b_n \end{bmatrix} \tag{8.48}$$

In the example above it is clear that every row in the matrix is a linear combination of the vector

$$\boldsymbol{B} = \begin{bmatrix} \mathrm{b}_1 \\ \vdots \\ \mathrm{b}_n \end{bmatrix} \tag{8.49}$$

And therefore all rows are linearly dependant, meaning the matrix has a rank of one, which as linear algebra tells us, cannot be inverted.

This shows that an implementation is problematic and would require some severe assumptions to be made on the structure of the matrix. Such assumptions are likely to compromise the rigour that is desirable in the objectives of this project, and therefore left as a suggestion for future work.

For instance, one potential method would be to calculate a pseudo-inverse of the matrix, which is possible using widely available linear algebra methods [99]. However it was decided not to continue with this since it would require significant work to understand the implications of this method and the effect it would have on the rigour of the solution method. Instead, alternative methods for implementing the mixed method are explored; in particular the direct discretisation of the strong form is attempted.

8.5 Strong Form of Hu-Washizu in an SPH Framework

The weak form of the mixed SPH equations cannot easily be solved due to the reasons described in §8.4.2. Therefore the next step is to attempt a discretisation of the strong form of the mixed equations, derived in the appendix resulting in (8.1), (8.2), (8.3), (8.4), and (8.5).

8.5.1 Assumed Rate of Deformation

We will begin with eq. (8.4) , which is a restriction on the rate of deformation. Conceptually this equation means that the velocity gradient calculated through the kinematic relation must be equal to the interpolated velocity that is the kernel estimation of the velocity gradient at particle I around the neighbouring particles, i.e.

$$D_{ij}(\boldsymbol{v}) - \overline{D}_{ij} = 0 \tag{8.50}$$

Where

$$D(\boldsymbol{v}) = sym \sum_{j}^{nnbr} (v_j - v_i) \nabla W_{ij} \frac{m_j}{\rho_j} \tag{8.51}$$

And:

$$\overline{D}_i = \sum_{j=1}^{np} \alpha_j W_{ij} \frac{m_j}{\rho_j} \tag{8.52}$$

Where in (8.52), the value α is an unknown quantity held at each of the neighbouring particles, and could be described as the discrete rate of deformation. Equating (8.51) and (8.52) leaves a system of equations in the form Ax-b=0

$$\boldsymbol{A} = \begin{bmatrix} W_{11}\frac{m_1}{\rho_1} & \cdots & W_{1n}\frac{m_n}{\rho_n} \\ \vdots & \ddots & \vdots \\ W_{n1}\frac{m_1}{\rho_1} & \cdots & W_{nn}\frac{m_n}{\rho_n} \end{bmatrix} \tag{8.53}$$

$$\boldsymbol{x} = \begin{bmatrix} \alpha_1 \\ \vdots \\ \alpha_n \end{bmatrix} \tag{8.54}$$

$$\boldsymbol{b} = \begin{bmatrix} D_1(v) \\ \vdots \\ D_n(v) \end{bmatrix} \tag{8.55}$$

The size of the matrix A will be $n \times n$, with n being the number of particles in the system, $\boldsymbol{x}$ will be $n \times 1$, and $\boldsymbol{b}$ will be $n \times 1$, which comprises of the rate of deformation term for each particle**.** A system would have to be formed for each entry of the rate of deformation tensor, 6 in 3D and 3 in 2D (assuming symmetry).

The system can then be solved for $\boldsymbol{x}$, leaving us with a value for α at each particle position, if α is then interpolated again then clearly the result will be the same as the value obtained through the evaluation of the velocity gradient. The components of $\boldsymbol{x}$ can be thought of as discrete particle values for strain rate.

$$\sum_{j}^{nnbr} \alpha_j W_{ij}^{\varepsilon} \frac{m_j}{\rho_j} = sym \sum_{j}^{nnbr} (v_j - v_i) \nabla W_{ij}^{v} \frac{m_j}{\rho_j} \tag{8.56}$$

The superscripts distinguish the kernel functions from one another.

Once the assumed rate of deformation is known then it can be used in the evaluated of the stress tensor through the constitutive relation.

8.5.2 Assumed stress

A similar approach can be followed for the calculation of the assumed stress,

$$\sigma_{ij}(\bar{\boldsymbol{D}}) - \overline{\sigma}_{ij} = 0 \text{ in } \Omega \tag{8.57}$$

$$\bar{\boldsymbol{\sigma}} = \sum_{j}^{nnbr} \beta_j W_{ij}^{\sigma} \frac{m_j}{\rho_j} \tag{8.58}$$

Identical steps as before can be followed, solving the same system of equations, this time for:

$$\boldsymbol{x} = \begin{bmatrix} \beta_1 \\ \vdots \\ \beta_n \end{bmatrix} \tag{8.59}$$

$$\boldsymbol{b} = \begin{bmatrix} \sigma_1(\bar{D}_{\mathbf{1}}) \\ \vdots \\ \sigma_n(\bar{D}_{\boldsymbol{n}}) \end{bmatrix} \tag{8.60}$$

When the assumed stress is known, (8.1) can be solved.

8.5.3 Solution procedure

The solution procedure is identical for both cases, the below outlines the method for the rate of deformation, where D can simply be replaced with the stress tensor

Step one – Find $\boldsymbol{\alpha}$

Solve the system using standard linear algebra methods

$$\begin{bmatrix} W_{11} & \cdots & W_{1n} \\ \vdots & \ddots & \vdots \\ W_{n1} & \cdots & W_{nn} \end{bmatrix} \begin{bmatrix} \alpha_1 \dfrac{m_1}{\rho_1} \\ \vdots \\ \alpha_{np} \dfrac{m_{np}}{\rho_{np}} \end{bmatrix} = \begin{bmatrix} D_1(\boldsymbol{v}) \\ \vdots \\ D_{np}(\boldsymbol{v}) \end{bmatrix} \tag{8.61}$$

Step Two

Calculate the assumed rate of deformation by (8.52)

Step Three

Calculate the stress from the assumed rate of deformation through the constitutive relation.

Step Four

Find β by solving the system:

$$\begin{bmatrix} W_{11} & \cdots & W_{1n} \\ \vdots & \ddots & \vdots \\ W_{n1} & \cdots & W_{nn} \end{bmatrix} \begin{bmatrix} \beta_1 \dfrac{m_1}{\rho_1} \\ \vdots \\ \beta_{np} \dfrac{m_{np}}{\rho_{np}} \end{bmatrix} = \begin{bmatrix} \sigma_1(\bar{D}_1) \\ \vdots \\ \sigma_n(\bar{D}_n) \end{bmatrix} \tag{8.62}$$

Step Five

Replace $\sigma_n(\bar{D}_n)$ with $\bar{\sigma}_n$ and calculate acceleration through the conventional SPH momentum equation, (2.41).

8.6 Implementation

The implementation of the mixed SPH formation requires the following additional subroutines.

Linear Algebra Solver – The mixed method requires either the inversion of a matrix, or a method to solve a linear system of equations, convention is generally to avoid inverting large matrices, therefore a subroutine is taken from numerical methods [99] which is used to solve a system of equations. A method that is considered efficient for solving large matrices is the conjugant gradient method, which is implemented in the MCM code for the purpose of this investigation.

Matrix Construction – A subroutine is implemented in order to construct the matrix from the kernel function values and the strain and stress terms, the same routine is used for both operations.

The matrix that is formed must be of dimension $np \times np$. This is due to the way in which the SPH interpolation works, the operation must be done globally and the same matrix cannot be constructed locally over only the neighbouring particles. This matrix has not particular fixed form, the matrix will always be sparse, but is not necessarily diagonal or

symmetric; the number of entries in each row is equal to the number of neighbouring particles of each i particle.

The additional subroutine can be found in the appendix.

8.6.1 Verification

The implementation of the mixed form requires a considerable amount of additional computation, the majority of which is due to the requirement to solve a large system of equations, which avoid the need to invert the matrix directly. Therefore it is essential that the code is verified to ensure that the method is working as desired. Thankfully the verification can be performed in a fairly simple way.

Firstly the conjugate gradient method was performed within the code on an arbitrary system of equation, the solution of which can easily be checked through elementary linear algebra. The results of this are omitted since no differences were found; instead a second more robust method of verification is presented which proves that the method of linear algebra used is working within the SPH framework.

The steps are as follows:

1. Populate the $np \times np$ matrix using particle values for the Swegle problem, both for the strain rate and stress.
2. Solve the system of equations using the conjugate gradient method. The result being the discrete values for strain rate and stress.
3. Rebuild the original strain rates and stresses by simply interpolating using the conventional cubic spline kernel.
4. Compare the results with those obtained from the basic SPH method.
5. If the method is working correctly both results should be the same, proving that the system was solved correctly.

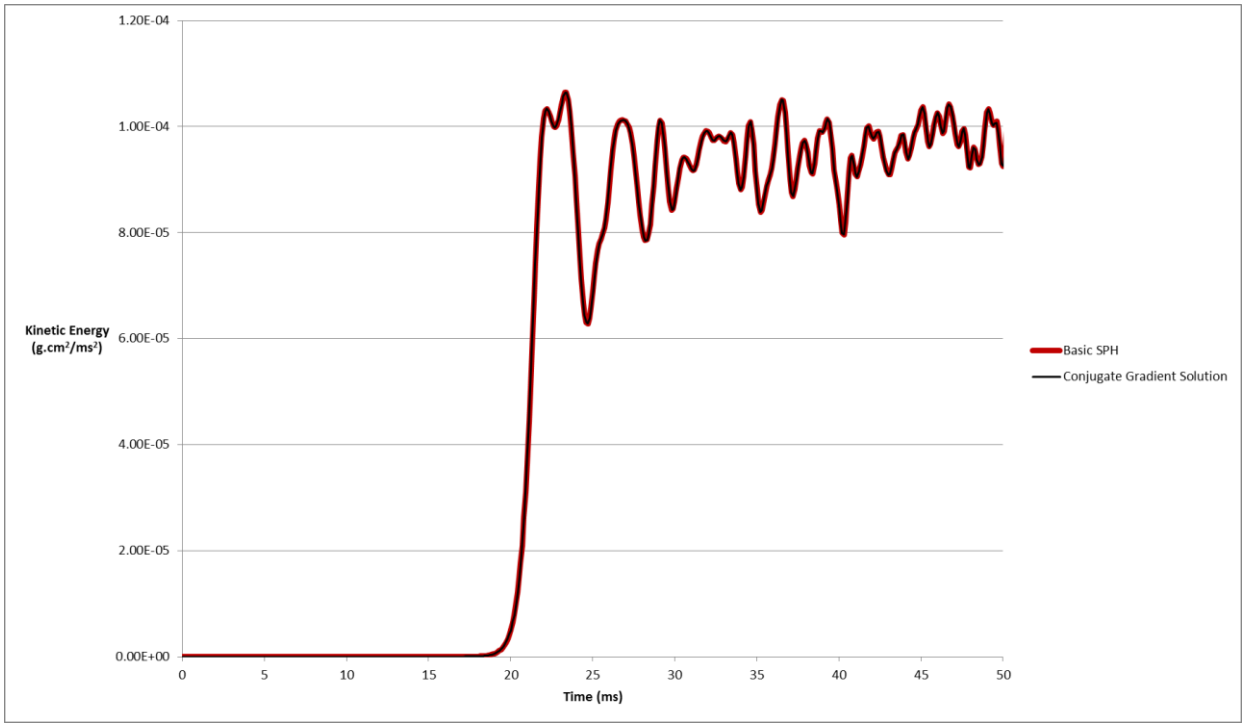

Figure *8-4 - Verification of the mixed element solution method for the Swegle problem*

Figure 8-4 shows that the two sets of results are identical, with the exception of some very small differences which are of such small magnitude that they can be considered purely numerical and as a consequence of the large number of additional operations on the data. Therefore it is considered that this method can be used as part of the implementation with full confidence.

8.6.2 Numerical Results

Figure 8-5 and Figure 8-6 show the results from the Swegle test using the mixed SPH method, using both the quadratic and quantic spline kernels as the secondary interpolation functions for the assumed rate of deformation and assumed stress, it is clear that the additional operations performed on the variables do not have a stabilising effect on the solution for this particular problem, in face the growth rate of the error seems to have increased in both cases.

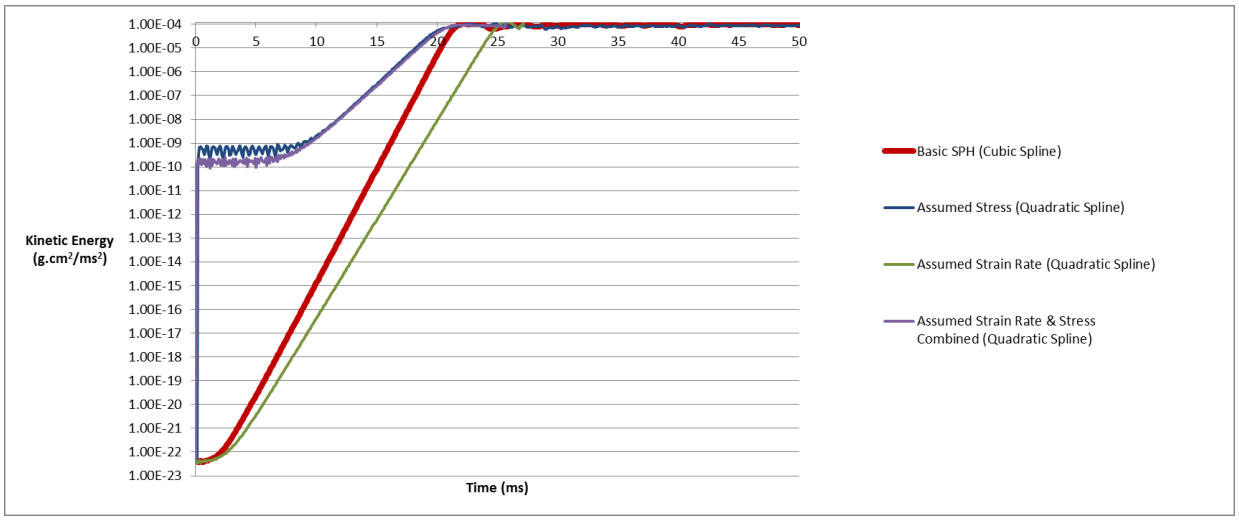

Figure *8-5 Assumed values calculated from the quadratic spline kernel*

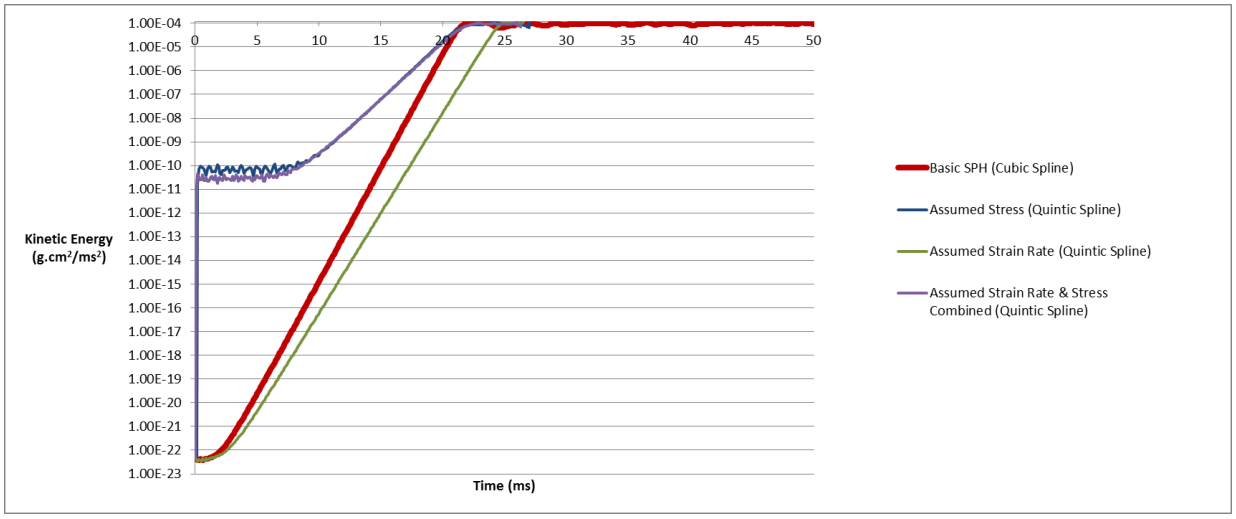

Figure *8-6 Assumed values calculated from the quintic spline kernel*

8.7 Conclusions

The objective of this chapter was to provide an investigation into potential improvements to the SPH method based on existing solutions that exist in finite element analysis. One particular topic of mixed element methods was identified as an appropriate method to investigate, (see §1.4.4), which can be derived and implemented in a number of ways, only one specific form was chosen due to the considerable effort required to adapt this form to work in an SPH framework, also since other mixed element type solutions were being investigated in other PhD work at the time. The form that was chosen to be implemented into the SPH code was the virtual power form using an assumed rate of deformation and stress. The implementation was verified to work correctly but when tested against the Swegle case, no improvement on the stability properties were observed. Since in the Swegle test there is only a hydrostatic pressure, the implementation tested was essentially equivalent to a rate of deformation – pressure form.

Since only one particular form was tested it is impossible to make conclusions about mixed methods in general, but it appears that the mixed form that was implemented does not improve the stability properties of the SPH method when tested against the benchmark cases used throughout this thesis.

9 Conclusions

9.1 Discussion

Each chapter in this thesis has addressed one of the aims defined in §1.4, which results in the aim of the thesis (§1.3) being met, i.e. To provide an investigation toward a rigorous derivation of a stable and consistent numerical method based on the established Smoothed Particle Hydrodynamics method, suitable for modelling the large deformation transient response of fluids and solids.

In order to achieve this a number of specific objectives were set in §1.4

Develop Understanding of the SPH Method

This fundamental objective was required in order to address the other objectives required in order to meet the overall aim. This objective was met through the completion of the following tasks, which were presented in chapters four and five:

a) Capability study of the SPH method. The capability of the SPH method to model complex problems of fluid structure interaction was demonstrated here, the coupled FE-SPH method was used to simulate the impact of a rigid cylinder on water, the simulation was performed in 2D and a convergence study showed that that good consistency can be achieved with experimental results when comparing pressure on the surface of the cylinder, results also showed that peak pressure can be predicted well even for a lower particle resolution. The same results could not be achieved in 3 dimensions; for this problem a solid sphere was dropped onto water and again the acceleration of the sphere was recorded and compared with experiment, which showed that the FE-SPH method overestimation the acceleration by almost a factor of two. The reasons for the differences are unknown and suggest that further investigation should be conducted using this type of problem.

   The next demonstration was the response of a steel plate subjected to loading from an underwater explosion; this is a complex problem especially due to the difficulty in simulating nearly incompressible flow, which is achieved in SPH by assuming weak compressibility. The deflection of the centre of a steel plate was compared

with experiment showing reasonable results for smaller explosive quantities, as the strength of the blast is increased the discrepancy between simulation and experiment grows. However, this is to be expected; as the strength of the initial shock increases it becomes harder to capture the peak pressure, i.e. an extremely fine particle distribution would be required close to the blast. That being said the steel plate behaves in the correct manner; other reasons for the differences would include differences in the material properties for the steel used in the experiment compared to the properties used in the material model in the FE-SPH analysis.

The capability study continued with the implementation of a turbulence model in the MCM code. Turbulence modelling is an important part of fluid modelling and had not been implemented in the MCM code, since turbulence models have been well studied and already adapted for use in an SPH code; this was a good opportunity to implement a relevant improvement to the code. A two equation $k-\varepsilon$ model was implemented and verified using a dam-break problem which was reproduced using the volume of fluid method (VOF) in Fluent. Since the objective was not to validate this model for any particular application and for that reason this particular study was concluded.

b) The capability study was concluded by the development and implementation of a friction model in SPH so as to determine the suitability of the contact algorithm implemented in MCM to model lateral forces between two SPH materials using the relative velocities between materials. To date the contact algorithm was not able to model lateral forces, and the work completed here provides the first novel improvement to the SPH method in this thesis. Friction modelling was identified as an appropriate problem in order to validate the approach, a friction model was tested using a simple sliding block problem which showed encouraging results with only a small amount of unphysical slippage suggesting that improved stiction models could be developed. The friction model was tested for a more complex problem involving metal forging which was simulated in 3D in which the metal is subject to a barrelling effect due to the effects of friction. This barrelling was reproduced well in the SPH simulation when compared to FE results from LS-DYNA; however some differences were observed in the forces that were produced during the forging. This could have been due to the fundamental differences in the

numerical method or could be due to the problem identified with the stiction model in the 2D results. It can be concluded however that the modified contact algorithm is able to resolve lateral forces between materials and is suitable for coupling with a structural FE model.

Investigate the Discrete Continuity Equation and its Effect on Stability

It was demonstrated in chapter two that mass continuity is implied by the continuous momentum equation, however in the discrete SPH form the continuity equation does not hold exactly, this suggests that the momentum equation must be corrected in order to account for this. This objective contributes to the overall aim by providing understanding into the effect of the conservation properties of the SPH equations on numerical stability. It was found after implementing a correction term in the MCM code that the stability of the method was not improved for the particular test problems used and the particular form of the correction term that was implemented; This suggests that the loss of volume that is associated with the SPH form of the continuity equation is not the main source of stability problems with the method

Investigation into Errors in the Gradient Approximation in SPH

A literature review presented in chapter three identifies issues with consistency and accuracy of the conventional SPH method as areas for potential improvement which may lead to an improved method in terms of stability. The continuous form of the momentum equation undergoes some manipulation before it is discretised, often leading to better results for reasons which are not well understood; In addition it has been noted that forms of the momentum equation which are fully conservative are more likely to exhibit instabilities. In this work a momentum equation is derived rigorously which minimises the error which develops due to the inability to approximate the gradients of constant non-zero function using non-uniform particle spacing. Consequently, stability is achieved for the Swegle test problem as well as the elastic impact problem, this also provides a possible explanation as to why certain forms of the momentum equation perform better than others; in some cases the error is minimised through the addition of extra terms; however in other cases the error is magnified leading to unstable growth. Stable solutions can be

achieved through the use of two different forms of momentum equation, which can be switched between subject to the stability criterion derived in chapter seven.

Investigate the Compatibility of FEM Solutions with SPH

The final objective looks toward solutions that are commonly applied in finite element methods to solve numerical issues with convergence and stability. The mixed element method was identified as an area for investigation which led to several attempts at mixed SPH methods developed using the same methods used in the explicit finite element method. Significant issues arise when developing a weak form of the mixed form that is compatible with SPH; the result is a system of equations which has a rank of one and cannot be inverted. Another potential option was investigated in the direct discretisation of the strong form of the equations which are a consequence of the virtual power form of the Hu-Washizu mixed formulation. The resulting SPH framework was implemented and tested using the Swegle test, which showed that in this instance, stability properties of the method did not appear to show improvement. However only one particular formulation was tested, many other variations are possible in terms of the variables that are treated independently in the mixed form and the way in which they are discretised.

To summarise, each objective has been addressed, which has resulted in:

- A set of SPH equation in which the momentum equation is consistent with the SPH form of the continuity equation.
- A contact algorithm in which the lateral forces between two SPH materials are resolved, suitable for coupling with a structural FE model.
- A rigorously derived set of SPH equations with improved stability properties and accompanying stability criterion.
- A derivation and implementation of a mixed SPH form based on the strong form of the Hu-Washizu virtual power equations.

9.2 Future Work

Continuations of the work presented in this thesis should include:

- Alternative discretisation's of the correction derived in chapter six preserving consistency between the continuity and momentum equations, this could involve alternative finite difference form used to calculate the rate of change of density (in summation form), as well as applying this correction at different phases in the calculation (e.g. velocity, displacement).
- Further work on the contact algorithm would look at other forms of lateral forces between materials, perhaps fluid and solid such as a wall roughness in pipe flow for example. Chapter five concluded that improved stiction models could be developed for the friction model in particular; continuations of this work should look at other potential implementations.
- Further investigations on the calculation for the average stress term of the neighbourhood developed in chapter seven in the modified SPH form should be conducted, such as using an SPH interpolation over the neighbouring particles, also other forms of stability analysis could be useful in determining the stability regime and identifying other forms of a stable SPH method suitable for resolving boundaries. One such method is eigenvalue stability analysis.
- Alternative mixed forms should be developed and tested using the framework developed in chapter eight, only one possible formulation was derived here; other potential options could involve mixed forms based on displacements, pressure, or velocity. Additionally a rigorous stability analysis should be done to identify specific stability criteria for the mixed SPH method.

10 References

1. *Smoothed Particle Hydrodynamics: Theory and Application to Non-Spherical Stars.* R, Gingold. and J, Monaghan. 1977, Monthly notices of the royal astronomical society, pp. 375-389.

2. *SPH Simulation of Multiphase Flow.* J, Monaghan. and A, Kocharyan. 1995, Computer Physics Communication, pp. 225-235.

3. *Parallel Simulation of Pore Scale Flow through Pourus Media.* Morris.J.P. 1999, Computers and Geotechnics, Vol. 25, pp. 227-246.

4. *Smooth Particle Hydrodynamics with Strength of Materials.* Libersky.L and A, Petschek. 1991, Advances in the free-Lagrange method including contributions on adaptive gridding and the smooth particle hydrodynamics method, pp. 248-257.

5. *High Strain Lagrangian Hydrodynamics: Three dimensional SPH Code for Material Response.* L.D., Libersky., et al. 1993, Journal of computational Physics, Vol. 109, pp. 67-75.

6. *A turbulence model for smoothed particle hydrodynamics.* J., Monaghan. 2009, European Journal of Mechanics, Vol. 30, pp. 360-370.

7. *Numerical modelling of complex turbulent free-surface flows with the SPH method : an overview.* Violeau.D and Issa.R. 2007, Vol. 53, pp. 277-304.

8. *Simulation of breaking wave by SPH method coupled with k-ε model.* S, Shao. 3, 2008, Journal of Hydraulic Research, Vol. 44, pp. 338-349.

9. *Incompressible SPH simulation of wave breaking and overtopping with turbulence modelling.* S, Shao. 2006, International Journal of Numerical Methods for Fluids, Vol. 50, pp. 597-621.

10. *A first Atempt to Adapt 3D Large Eddy Simulation to the Smoothed Particle Hydrodynamics Gridless Method.* Issa.R, Violeau.D and Laurence.D. Stara-Lesna (Slovakia) : s.n., 2004. International conference of computational and experimental engineering and sciences.

11. D, Violeau. *Fluid Mechanics and the SPH Method: theory and Applications.* Oxford : Oxford University Press, 2012.

12. *Smoothed Particle Hydrodynamics Stability Analysis.* J, Swegle., D, Hicks. and S, Attaway. 1995, Journal of Computational Physics, pp. 123-134.

13. *Correction and Stabilization of Smooth Particle Hydrodynamics Methods with Applications in Metal forming Simulations.* Bonet.J and Kulasegaram.S. 2000, International journal for numerical methods in engineering., Vol. 47, pp. 1189-1214.

14. Liu.G.R and Liu.M.B. *Smoothed Particle Hydrodynamics: A Meshfree Particle Method.* s.l. : World Scientific Publishing Co. Pte. Ltd, 2003.

15. *A Frictionless Contact Algorithm for Meshless Methods.* Vignjevic.R, Campbell.J and Vuyst.T, De. 2, 2007, ICCES, Vol. 3, pp. 107-112.

16. LeVeque.R.J. *Numerical Methods for conservation Laws.* 132. Basel : Birkhauser, 1992.

17. Smith.G. *Numerical Solution of partial Differential Equations: Finite Difference Methods.* Oxford : Oxford University Press, 1985.

18. Marchuk.G.I. *Method of Numerical Mathematics.* New York : Sringer, 1975.

19. *Improving convergence in Smoothed particle Hydrodynamics Simulations without Pairing Instability.* Dehnen.W and Aly.H. 2012, Royal astronomical Society, pp. 1-15.

20. *Numerical Convergence in Smoothed Particle Hydrodynamics.* Zhu, Qirong, Lars Hernquist, Yuexing Li. 6, 2015, The Astrophysical Journal , Vol. 800.1.

21. *Survey of the stability of linear finite difference equations.* P.D., Lax. and R.D., Richtmyer. 1956, Communications in Pure and Applied Mathematics, Vol. 9, pp. 267-293.

22. Trefethen.L.N. *Finite Difference and Spectral Methods for Ordinary and Partial Differential Equations.* s.l. : Cornell University - Department of computer Science and Center for Applied Mathematics, 1996.

23. *Smoothed Particle Hydrodynamics: Some Recent Improvements and Applications.* P.W, Randles. and Liberski.L.D. 1996, Computational Methods in Applied Mechanics and Engineering, Vol. 139, pp. 375-408.

24. *A Treatment for Zero-Energy Modes in the Smoothed Particle Hydrodynamics Method.* Vignjevic.R, Campbell.J and Libersky.L. 1, 2000, Computer Methods in Applied Mechanics and Engineering, Vol. 184, pp. 67-85.

25. *Element Free Galerkin Methods.* Belytschko.T., Lu.Y.Y and Gu.L. 1994, International journal for Numerical Methods in Engineering, Vol. 37, pp. 229-256.

26. *Consistent pseudo derivatives in meshless methods.* Y., Krongauz. and T, Belytschko. 1997, Computer Methods in Applied Mechanics and Engineering, Vol. 146, pp. 371-386.

27. *Reproducing Particle Methods for Structural Dynamics.* W., Liu., et al. 1995, International Journal for Numerical Methods in Engineering, Vol. 38, pp. 1655-1679.

28. *A new Meshless Local Petrov Galerkin (MLPG) approach in computational mechanics.* S., Atluri. and T., Zhu. 2000, journal of computational mechanics, Vol. 22, pp. 117-127.

29. *Error estimation in smoothed particle hydrodynamics and a new scheme for second derivatives.* R. Fatehi, M.T. Manzari. 2, 2011, Computers & Mathematics with Applications, Vol. 61.

30. *Truncation error in mesh-free particle methods.* N. Quinlan, M. Basa, M. Lastiwka. 13, 2006, International Journal for Numerical Methods in Engineerin, Vol. 66.

31. Strand.R.K. *SPH Modelling for Failure in Metals.* Cranfield university. 2010. Thesis.

32. *Towards a Better Undestanding of the Smoothed Particle Hydrodynamics Method.* M, Gourma. 2003.

33. Powell.S. *Non-reflecting boundary conditions and tensile instability in smooth particle hydrodynamics.* Cranfield University. s.l. : Cranfield Thesis, 2012. Thesis.

34. Reveles.J.R. *Development of a Total Lagrange SPH Code for the Simulation of Solids Under Dynamic Loading.* Cranfield University. 2007. Thesis.

35. *SPH in a Total Lagrangian Formalism.* R, Vignjevic., J, Reveles. and J, Campbell. 2006, Computational Methods in Engineering and Science, Vol. 14, pp. 181-198.

36. *Review of Development of the Smooth Particle Hydrodynamics Method.* R., Vignjevic. and J, Campbell. 2009, Predictive Modeling of Dynamic Processes., pp. 367-396.

37. *Momentum Conserving Methods that Reduce Clustering in SPH.* S.P, Korzilius., et al. June 2014, 9th International Smoothed Particle Hydrodynamics European Research Interest Community Workshop (SPHERIC 2014, Paris, France), pp. 268-275.

38. Neuenschwander.D.E. *Emmy noether's Wonderful Theorem.* s.l. : JHU Press, 2010.

39. *Addressing Tension Instability in SPH Methods.* Dyka.C.T. 1994, NRL Report, NRLIMR/6384.

40. *Stability analysis of Particle Methods with corrected Derivatives.* Belytschko.T and Xiao.S. 2002, Computational Mathematics, Vol. 43, pp. 329-350.

41. *SPH Without a Tensile Instability.* Monaghan.J. 2000, Journal of Computational Physics, pp. 290-311.

42. *SPH Elastic Dynamics.* P., Gray. J., Monaghan.J.J and Swift.R.P. 49, 2001, Computer methods in applied mechanics and engineering, Vol. 190, pp. 6641-6662.

43. *SPH Hydrocodes can be Stabilized with Shapeshifting.* D.L, Hicks. and L.M, Liebrook. 1999, Computers and Mathematcis with Applications, Vol. 38, pp. 1-16.

44. *SPH: Instabilities, Wall Heating and Conservative Smoothing.* Hicks.D.L, Swegle.J.W and Attaway.S.W. 1993, Proc: Workshop pn Advances in Smoothed Particle Hydrodynamics, Los Alamos National Laboratory Report, Vols. #LA-UR-93-4375, pp. 223-256.

45. *Stabilizing SPH with Conservative Smoothing.* Wen.Y, Hicks.D.L and Swegle.J.W. 1994, Sandia Report.

46. *A study of the stability properties of smoothed particle hydrodynamics.* Morris.J. 1996, Publications of the Astronomical Society of Australia, Vol. 13, pp. 97-102.

47. *An improvement for tensile instability in smoothed particle hydrodynamics.* Chen.J.K, Beraun.J.E and Jih.C.E. 1999, Journal of Computational Mechanics, Vol. 23, pp. 279-287.

48. *von Neumann stability analysis of smoothed particle hydrodynamics—suggestions for optimal algorithms.* Balsara.D. 1995, Journal of Computational Physics, pp. 357-372.

49. *A new stable version of the SPH method in lagrangian coordinates.* A, Ferrari., et al. 2008, Communications in Computational Physics, pp. 378-404.

50. *Derivation of SPH equations in a moving referential coordinate system.* Vignjevic.R., et al. 30-32, 2009, Computer Methods in Applied Mechanics and Engineering, pp. 2403-2411.

51. *Conservation of Momentum and Tensile Instability in Particle Methods.* Swegle.J. 2000, SANDIA Report, Vols. SAND2000-1223.

52. *An Introduction to SPH.* J.J., Monaghan. 1988, Computer Physics Communications, Vol. 48, pp. 89-96.

53. *Smoothed Particle Hydrodynamics in cosmology: a comparative study of implementations.* Thacker.R.J., et al. 2000, Monthly Notes from the Royal Astronomical Society, Vol. 319, pp. 619-648.

54. Colagrossi.A. *A Meshless Lagrangian Method for Free-Surface and Interface with Fragmentation.* Università di Roma La Sapienza. 2003. PhD Thesis.

55. *Smoothed Particle Hydrodynamics.* Monaghan.J.J. 1992, Annual Review of Astronomy and Astrophysics, Vol. 30, pp. 543-574.

56. *Hydrocode modelling of water impact.* T, De Vuyst. 2003, PhD Thesis.

57. K.J, Bathe. *Finite Element Procedures.* s.l. : Prentice Hal, 2006.

58. Shen.S.W and Gu.L. *Introduction to the Explicit finite element Method for nonlinear Transient Dynamics.* s.l. : John wiley & Sons, 2012.

59. T, Belytschko. *Nonlinear finite elements for continua and structures.* s.l. : John Wiley & Sons, 2013.

60. *Displacement/pressure based mixed finite element formulations for acoustic fluid-structure interaction problems.* W., Xiaodong. and K.J, Bathe. 11, 1997, International journal for Numerical Methods in Engineering, Vol. 40, pp. 2001-2017.

61. *Hydrodynamic Impact Analysis.* Gross.M.B, et al. June 1978, EPRI Report NP-824, Projects 812-1, 2, 3 and 965-3, Palo Alto, CA.

62. *Simulating space capsule water landing with explicit finite element method.* J.T., Wang. and Lyle.K.H. April 2007, 48 th AIAA/ASME Conference, pp. 23-26.

63. *The effects of air and underwater blast on composite sandwich panels and tubular laminate structures.* H., Arora., Hooper.P.A. and Dear.J.P. 1, 2012, Experimental mechanics, Vol. 52, pp. 59-81.

64. *Explosion Effects and Properties. Part II. Explosion Effects in Water.* Swisdak.M. 1978, NAVAL SURFACE WEAPONS CENTER WHITE OAK LAB SILVER SPRING MD, Vols. No. NSWC/WOL/TR-76-116.

65. *Estimating Equivalency Of Explosives Through A Thermochemical Approach.* Maienschein.J.L. 2002, No. UCRL-JC-147683, Lawrence Livermore National lab, CA.

66. *Performance of HSLA Steel Subjected to Underwater Explosion.* Rajendran.R and Narasimhan.K. 2001, Journal of Materials Engineering and Performance.

67. . *Smoothed particle hydrodynamics model applied to hydraulic structures: a hydraulic jump test case.* D., Lopez., R., Marivela. and L., Garrote. 2010, Journal of Hydraulic Research, Vol. 48, pp. 142-158.

68. *Turbulence Modeling Validation, Testing, and Development.* Bardina, J.E., Huang, P.G., Coakley, T.J. 1997, NASA Technical Memorandum, Vol. 110446.

69. *Computational Modeling of the Hydraulic Jump in the Stilling.* Babaali, H. and A.Shamsai. 2, 2015, Arabian Journal for Science and Engineering, Vol. 40.

70. *k-ε turbulence modelling of submerged hydraulic jump using boundary-fitted coordinates.* Gunal, M., and R. Narayanan. 2, 1998, Proceedings of the Institution of Civil Engineers. Water, maritime and energy, Vol. 130.

71. J, Raiford. *Numerical and physical modeling of turbulent shear flows - PhD Thesis.* s.l. : Clemson University, 2007.

72. *The Compressibility of Media under Extreme Pressures.* F.D., Murnaghan. 1944. Proceedings of the National Academy of Sciences of the United States of America. pp. 244-247.

73. Larocque.L.A. *Experimental and Numerical Modeling of Dam-Break and Levee-Breach Flows - Doctoral Dissertation.* s.l. : University of South Carolina, 2012.

74. *A penalty approach for contact in smoothed particle hydrodynamics.* R, Vignjevic. and J, Campbell. 1, 1999, International Journal of Impact Engineering, Vol. 23, pp. 945-956.

75. *A contact Algorithm for Smoothed Particle Hydrodynamics.* Campbell.J, Vignjevic.R and Libersky.L. 2000, Computational Method in Applied Mechanical Engineering, Vol. 184, pp. 49-65.

76. S., Li. and W.K., Liu. *Meshfree Particle Methods.* Berlin : Springer, 2004.

77. *Coupling of smooth particle hydrodynamics with the finite element method.* Attaway.S, Heinstein.M. and Swegle.J. 1994, Nuclear engineering and Design, pp. 199-205.

78. *Linking of Particle Lagrangian Methods to Standard Finite element Methods for High Velocity Imact Computations.* G, Johnson. 1994, Nuclear engineering and Design, pp. 265-274.

79. *SPH for High Velocity Impact Computations.* Johnson.G.R, .R.A, Stryk and Beissel.S.R. 1996, Computer Methods in Applied Mechanics and Engineering, Vol. 139, pp. 347-374.

80. *A parametric study of bird strike on engine blades.* R., Vignjevic., et al. 2013, International Journal of Impact Engineering, Vol. 60, pp. 44-57.

81. *From aerospace to offshore: Bridging the numerical simulation gaps–Simulation advancements for fluid structure interaction problems.* K., Hughes., et al. 2013, International Journal of Impact Engineering, Vol. 61, pp. 48-63.

82. *Coupling between meshless and finite element methods.* Vuyst.T, De, Vignjevic.R and Campbell.J. 2005, International Journal of Impact Engineering, Vol. 31, pp. 1054–1061.

83. *A Contact Algorithm for Smoothed Particle Hydrodynamics.* Campbell, J, Vignjevic, R and Libersky, L. 2000, Computer Methods in Applied Mechanics and Engineering, pp. 49-65.

84. *On the Problem of Penetration in Particle Methods.* Monaghan.J.J. 1989, Computational Physics, Vol. 82, pp. 1-15.

85. *A Frictionless Contact Algorithm for Meshless Methods.* Vignjevic.R, Campbell.J and Vuyst.T, De. 2006, Computer Modelling in Engineering & Sciences, Vol. 13, pp. 35-48.

86. C., Zienkiewicz. O., L., Taylor. R. and C., Zienkiewicz. O. *The Finite element Method (Vol 3).* London : McGraw-Hill, 1977.

87. R, Wagoner. and J, Chenot. *Metal forming analysis.* s.l. : Cambridge University Press, 2001.

88. http://freevibrationanalysis.blogspot.co.uk/2011/08/brief-introduction-to-vibration_04.html. [Online] November 2015.

89. *Smoothed Particle Hydrodynamics.* Monaghan.J.J. 2005, Reports in Progress in physics, Vol. 68, pp. 1703-1759.

90. *Review of the Development of the Smooth Particle Hydrodynamics (SPH) Method.* R, Vignjevic. and J, Campbell. 2009, Predictive Modeling of Dynamic Processes, pp. 367-396.

91. *Mixed finite element methods for elliptic problems.* Arnold.N. 1, 1990, Computer Methods in Applied Mechanics and Engineering, Vol. 82, pp. 281-300.

92. *Simulation of miscible displacement using mixed methods and a modified method of characteristics.* T., Ewing., T., Russell. and M, Wheeler. 1983, Seventh Symposium on Reservoir Simulation, SPE 12241, San Fransisco.

93. *Mixed finite element methods for miscible displacement in porous media.* B., Darlow., E., Ewing. and M., Wheeler. 1982, Sixth Symposium for Reservoir Simulation, SPE 10501, New Orleans.

94. *Displacement/pressure based mixed finite element formulations for acoustic fluid-structure interaction problems.* X, Wang. and K.J, Bathe. 1997, International Journal for Numerical Methods in Engineering, pp. 2001-2017.

95. M, Fortin. and F, Brezzi. *Mixed and hybrid finite element methods.* New York : Springer-Verlag, 1991.

96. *www.twi-global.com.* [Online] Accessed: October 2015. http://www.twi-global.com/technical-knowledge/faqs/structural-integrity-faqs/faq-what-is-reduced-integration-in-the-context-of-finite-element-analysis/.

97. *On some variational principles in the theory of elasticity and the theory of plasticity.* H, Hu. 1955, Scientia Sinica, pp. 33-54.

98. K, Washizu. *Variational Methods in Elasticity and Plasticity.* s.l. : Elsevier Science & Technology, 1974.

99. H., Press. W., et al. *Numerical recipes in FORTRAN.* Cambridge : Cambridge University Press, 1992.

100. *A Penalty Approach for Contact in Smoothed Particle Hydrodynamics.* Vignjevic, R and Campbell, J. 1999, Journal of Impact Engineering, pp. 945-956.

101. *Normalized SPH with Stress Points.* Randles. P.W., Libersky. L.D. 10, 2000, International journal for Numerical Methods in Engineering, Vol. 48, pp. 1445-1462.

102. *Improvements in SPH method by means of interparticle contact algorithm and analysis of perforation tests at moderate projectile velocities.* Parshikov, A, et al. 2000, International Journal of Impact Engineering, pp. 779-796.

103. *Simulation of the Effects of an Air Blast Wave.* M, Larcher. 2007, JRC Technical note, Pubsy, JRC41337, Ispra.

104. *A Moving Least Squares Particle Hydrodynamics - Consistency and Stability.* G.A., Dilts. 1997, International Journal for Numerical Methods in Engineering.

105. *A contact algorithm for smoothed particle hydrodynamics.* Campbell, J, Vignjevic, R and Libersky, L. 2000, Computer methods in applied mechanics and engineering , pp. 49-65.

106. *SPH granular flow with friction and cohesion.* Alduán, I and Otaduy, M. 2011, pp. 25-32.

107. *Smoothed particle hydrodynamics using interparticle contact algorithms.* Parshikov, A and Stanislav.A. 2002, Journal of computational physics, pp. 358-382.

108. *SPH Elastic Dynamics.* Gray.P, Monaghan.J.J and Swift.R.P. 2001, Computer methods in applied mechanics and engineering, pp. 6641-6662.

109. *A numerical Approach to the Testing of the Fission Hypothesis.* L, Lucy. 1977, Astronomical Journal, pp. 1013-1024.

110. *Smoothed particle hydrodynamics: theory and application to non-spherical stars.* Gingold.R.A. and Monaghan.J.J. 1977, Monthly Notices Royal Astronomical Society, pp. 375-389.

111. *A displacement method for the analysis of vibrations of coupled Fluid structure systems.* M.A, Hamdi., Y., Ousset. and Verchery.G. 1978, International Journal of Numerical Methods in Engineering, Vol. 13.

112. *Contact-impact by the pinball algorithm with penalty and Lagrangian methods.* T, Belytschko. and Neal.M. 1991, International Journal for Numerical Methods in Engineering, pp. 547-572.

113. *Smoothed Particle Hydrodynamics with Strength of Materials.* L.D., Libersky. and A.G, Petschek. 1991, Proceedings of the Next Free Lagrange Conference, pp. 248-257.

114. *Coupling of Smoothed Particle Hydrodynamics with the Finite Element Method, Post-SMIRT Impact IV Seminar.* Attaway.S.W, Heinstein.M.W and Swegle.J.W. 1994, Nuclear Engineering and Design, p. 150.

115. *Stress points for Tension Instability in SPH.* C.T, Dyka., Randles.P.W and R.P, Ingel. 1997, International journal of Numerical Methods, Vol. 40, pp. 2325-2341.

116. *A frictionless contact algorithm for meshless methods.* Vignjevic, . R, T, De Vuyst. and J, Campbell. 2006, Computer Modeling in Engineering and Sciences.

117. *On the Implementation of the k - ε turbulence model in incompressible flow solvers based on a finite element discretization.* Kuzmin.D. and Mierka.O. 2006, International conference on boundary layers and interior layers, pp. 1-8.

118. *SPH without a Tensile Instability.* J.J, Monaghan. 2000, Journal of computational Physics, Vol. 159, pp. 290-311.

11

Appendix

11.1 .Hu-Washizu Derivation

The derivation of the virtual power from of the Hu-Washizu form is presented here, taken from [59].

The equations of motion can be written in a generalized form through the principle of virtual power

$$\delta P = \delta P^{int} - \delta P^{ext} + \delta P^{kin} = 0 \tag{11.1}$$

With

$$\delta P^{int} = \int_{\Omega} \delta D_{ij} \sigma_{ij} d\Omega \tag{11.2}$$

$$\delta P^{ext} = \int_{\Omega} \delta v_i \rho b_i d\Omega + \sum_{j=1}^{dim} \int_{\Gamma_{t_j}} \delta v_j \bar{t}_j d\Gamma \tag{11.3}$$

$$\delta P^{kin} = \int_{\Omega} \delta v_i \rho \dot{v}_i d\Omega \tag{11.4}$$

We will now see how the equations of motion is strong form can be deduced from the above equations, if we start with the right had side of (11.2)

$$\int_{\Omega} \delta D_{ij} \sigma_{ji} d\Omega = \int_{\Omega} \frac{\partial(\delta v_i)}{\partial x_j} \sigma_{ji} d\Omega = \int_{\Omega} \frac{\partial(\delta v_i \sigma_{ji})}{\partial x_j} d\Omega - \int_{\Omega} \frac{\partial \sigma_{ji}}{\partial x_j} \delta v_i d\Omega \tag{11.5}$$

Now applying divergence theorem to the first term on the right hand side of (11.5)

Where (11.5) can be arrived at since the product of the symmetric tensor σ_{ij} and the anti-symmetric spins tensor W_{ij} in (11.6) is equal to zero.

$$\sigma_{ij} \frac{\partial v_i}{\partial x_j} = \sigma_{ij}(D_{ij} + W_{ij}) \tag{11.6}$$

$$\int_{\Omega} \frac{\partial(\delta v_i \sigma_{ji})}{\partial x_j} d\Omega = \int_{\Gamma} \delta v_i n_j \sigma_{ji} d\Gamma + \int_{\Gamma_{int}} \delta v_i [\![n_j \sigma_{ji}]\!] d\Gamma$$
$$= \sum_{i=1}^{dim} \int_{\Gamma} \delta v_i n_j \sigma_{ji} d\Gamma + \int_{\Gamma_{int}} \delta v_i [\![n_j \sigma_{ji}]\!] d\Gamma \quad (11.7)$$

Substituting the terms for δP^{int} (11.7), δP^{ext} (11.3), and δP^{kin} (11.4) into (11.1).

$$\sum_{i=1}^{dim} \int_{\Gamma} \delta v_i n_j \sigma_{ji} d\Gamma + \int_{\Gamma_{int}} \delta v_i [\![n_j \sigma_{ji}]\!] d\Gamma - \int_{\Omega} \delta v_i \rho b_i d\Omega + \sum_{j=1}^{dim} \int_{\Gamma_{t_j}} \delta v_j \bar{t}_j d\Gamma$$
$$+ \int_{\Omega} \delta v_i \rho \dot{v}_i d\Omega - \int_{\Omega} \frac{\partial \sigma_{ji}}{\partial x_j} \delta v_i d\Omega \quad (11.8)$$

And collecting the terms

$$\sum_{i=1}^{dim} \int_{\Gamma} \delta v_i (n_j \sigma_{ji} - \bar{t}_j) d\Gamma + \int_{\Gamma_{int}} \delta v_i [\![n_j \sigma_{ji}]\!] d\Gamma -$$
$$\int_{\Omega} \delta v_i \left(\frac{\partial \sigma_{ji}}{\partial x_j} + \rho b_i - \rho \dot{v}_i \right) d\Omega \quad (11.9)$$

The variations will now vanish; this is due to the fundamental theorem of variational calculus, leaving

$$n_j \sigma_{ji} = \bar{t}_j \text{ on } \Gamma_{int} \quad (11.10)$$

$$[\![n_j \sigma_{ji}]\!] = 0 \text{ on } \Gamma_{t_j} \quad (11.11)$$

$$\frac{\partial \sigma_{ji}}{\partial x_j} + \rho b_i = \rho \dot{v}_i \text{ in } \Omega \quad (11.12)$$

Which are the traction boundary condition (11.10), the interior continuity conditions (11.11), and the momentum equation (11.12).

11.2 Mixed form of virtual power

The Hu-Washizu form of the virtual power equations takes the following form.

$$\delta P = \int_{\Omega} \delta \overline{D}_{ij} \sigma_{ij}(\overline{\boldsymbol{D}}) d\Omega + \int_{\Omega} \delta\left[\overline{\sigma}_{ij}\left(D_{ij}(\boldsymbol{v}) - \overline{D}_{ij}\right)\right] d\Omega - \delta P^{ext} + \delta P^{kin} = 0 \quad \textit{(11.13)}$$

In the above, the over-bar indicates an assumed value, i.e. a value that is evaluated independently. $\overline{D}_{ij}$ is the assumed rate of deformation, $\sigma_{ij}(\overline{\boldsymbol{D}})$ are the stresses written as a function of the assumed rate of deformation

$\overline{D}_{ij}$	Assumed rate of deformation
$\overline{\sigma}_{ij}$	Assumed stress
$\sigma_{ij}(\overline{\boldsymbol{D}})$	Stress calculated from the assumed rate of deformation through the constitutive relation.
$D_{ij}(\boldsymbol{v})$	Rate of deformation calculated through kinematic relations.

The same process can be used as in the previous example, the only difference in the second term on the right of (11.13) involving the strain rate D.

$$\begin{aligned} &\int_{\Omega} \delta\left[\overline{\sigma}_{ij}\left(D_{ij}(\boldsymbol{v}) - \overline{D}_{ij}\right)\right] d\Omega \\ &\qquad = \int_{\Omega} \delta\overline{\sigma}_{ij}\left(D_{ij}(\boldsymbol{v}) - \overline{D}_{ij}\right) d\Omega - \int_{\Omega} \overline{\sigma}_{ij}\left(\delta D_{ij}(\boldsymbol{v}) - \delta\overline{D}_{ij}\right) d\Omega \end{aligned} \quad \textit{(11.14)}$$

Since the stress tensor is symmetric the following is true.

$$\int_{\Omega} \bar{\sigma}_{ij}\delta D_{ij} d\Omega = \int_{\Omega} \bar{\sigma}_{ij}\delta v_{i,j}\, d\Omega = \int_{\Omega} \left(\bar{\sigma}_{ij}\delta v_i\right)_{,j} d\Omega - \int_{\Omega} \bar{\sigma}_{ij,j}\delta v_i\, d\Omega \tag{11.15}$$

Applying divergence theorem

$$\begin{aligned}\int_{\Omega} \left(\bar{\sigma}_{ij}\delta v_i\right)_j d\Omega - \int_{\Omega} \bar{\sigma}_{ij,j}\delta v_i d\Omega \\ = \int_{\Gamma_t} \delta v_i \bar{\sigma}_{ij} n_j d\Gamma + \int_{\Gamma_{int}} \delta v_i \left[\!\left[\bar{\sigma}_{ij} n_j\right]\!\right] d\Gamma - \int_{\Omega} \bar{\sigma}_{ij,j}\delta v_i\, d\Omega\end{aligned} \tag{11.16}$$

Substituting (11.16) back into (11.15)

$$\begin{aligned}\int_{\Omega} \delta\bar{D}_{ij}\sigma_{ij}(\bar{\boldsymbol{D}})d\Omega + \int_{\Omega} \delta\bar{\sigma}_{ij}\left(D_{ij}(\boldsymbol{v}) - \bar{D}_{ij}\right) d\Omega + \int_{\Gamma_t} \delta v_i \bar{\sigma}_{ij} n_j d\Gamma \\ + \int_{\Gamma_{int}} \delta v_i \left[\!\left[\bar{\sigma}_{ij} n_j\right]\!\right] d\Gamma - \int_{\Omega} \bar{\sigma}_{ij,j}\delta v_i\, d\Omega + \int_{\Omega} \delta\bar{D}_{ij}\bar{\sigma}_{ij} d\Omega \\ - \int_{\Omega} \delta v_i \rho b_i d\Omega + \sum_{j=1}^{dim} \int_{\Gamma_{t_j}} \delta v_j \bar{t}_j d\Gamma + \int_{\Omega} \delta v_i \rho \dot{v}_i d\Omega\end{aligned} \tag{11.17}$$

Collecting terms:

$$\begin{aligned}\int_{\Omega} \delta\bar{D}_{ij}\left(\sigma_{ij}(\bar{\boldsymbol{D}}) - \bar{\sigma}_{ij}\right)d\Omega + \int_{\Gamma_{int}} \delta v_i \left[\!\left[\bar{\sigma}_{ij} n_j\right]\!\right] d\Gamma \\ + \int_{\Gamma_{t_j}} \delta v_j \left(\bar{t}_j - \bar{\sigma}_{ij} n_j\right) d\Gamma + \int_{\Omega} \delta v_i \left(\rho \dot{v}_i - \bar{\sigma}_{ij,j} - \rho b_i\right) d\Omega \\ + \int_{\Omega} \delta\bar{\sigma}_{ij}\left(D_{ij}(\boldsymbol{v}) - \bar{D}_{ij}\right) d\Omega\end{aligned} \tag{11.18}$$

After applying the fundamental theorem of variational calculus, the variation vanishes leaving:

$$\rho \dot{v}_i - \bar{\sigma}_{ij,j} - \rho b_i = 0 \text{ in } \Omega \tag{11.19}$$

$$\left[\left[\overline{\sigma}_{ij} n_j\right]\right] = 0 \text{ on } \Gamma \tag{11.20}$$

$$\bar{t}_j - \overline{\sigma}_{ij} n_j = 0 \text{ on } \Gamma \tag{11.21}$$

$$D_{ij}(\boldsymbol{v}) - \overline{D}_{ij} = 0 \text{ in } \Omega \tag{11.22}$$

$$\sigma_{ij}(\overline{\boldsymbol{D}}) - \overline{\sigma}_{ij} = 0 \text{ in } \Omega \tag{11.23}$$

Which are the momentum equation (11.19), the interior continuity conditions (11.20), traction boundary conditions (11.21), the strain measure (11.22), and the constitutive relation (11.23).

11.3 Finite Element Discretisation of the Hu-Washizu equations

The Hu-Washizu form of the virtual power equations takes the following form.

$$\delta\Pi^{HW}(\boldsymbol{v},\overline{\boldsymbol{D}},\overline{\boldsymbol{\sigma}}) = 0$$
$$= \int_{\Omega} \delta\overline{D}_{ij}\sigma_{ij}(\overline{\boldsymbol{D}})d\Omega + \int_{\Omega} \delta\left[\bar{\sigma}_{ij}\left(D_{ij}(\boldsymbol{v}) - \overline{D}_{ij}\right)\right]d\Omega - \delta P^{ext} \qquad (11.24)$$
$$+ \delta P^{kin}$$

Where the virtual kinetic and external power terms are

$$\delta P^{ext} = \int_{\Omega} \delta v_i \rho b_i d\Omega + \sum_{j=1}^{dim} \int_{\Gamma_{t_j}} \delta v_j \bar{t}_j d\Gamma \qquad (11.25)$$

$$\delta P^{kin} = \int_{\Omega} \delta v_i \rho \dot{v}_i d\Omega \qquad (11.26)$$

δ	variation
Ω	volume
Γ_{t_j}	Surface on which traction boundary conditions are applied
$\boldsymbol{v}$	Velocity vector
$\overline{D}_{ij}$	Assumed rate of strain
$D_{ij}(\boldsymbol{v})$	Strain rate evaluated through kinematic relation.
$\sigma_{ij}(\overline{\boldsymbol{D}})$	Stress tensor evaluated from assumed strain rate through constitutive relation.

$\overline{\sigma}_{ij}$	Assumed stress tensor
b	Body force
$\bar{t}_j$	Traction vector

The dependant variables are velocity, strain rate and stress. Their finite element approximations are given by:

$$v_i(\boldsymbol{\xi}, t) = N_{iA}(\boldsymbol{\xi})\dot{d}_A(t) \tag{11.27}$$

$$\overline{D}_{ij}(\boldsymbol{\xi}, t) = N^D_{ijA}(\boldsymbol{\xi})\alpha^e_A(t) \tag{11.28}$$

$$\overline{\sigma}_{ij}(\boldsymbol{\xi}, t) = N^\sigma_{ijA}(\boldsymbol{\xi})\beta^e_A(t) \tag{11.29}$$

The test functions are

$$\delta v_i(\boldsymbol{\xi}) = N_{iA}(\boldsymbol{\xi})\delta\dot{d}_A \tag{11.30}$$

$$\delta\overline{D}_{ij}(\boldsymbol{\xi}) = N^D_{ijC}(\boldsymbol{\xi})\delta\alpha^e_C \tag{11.31}$$

$$\delta\overline{\sigma}_{ij}(\boldsymbol{\xi}, t) = N^\sigma_{ijB}(\boldsymbol{\xi})\delta\beta^e_B \tag{11.32}$$

Substituting into the first equation

$$\delta P = \sum_e \delta\alpha_C^e \int_{\Omega_e} N_{ijC}^D \sigma_{ij}(\bar{\boldsymbol{D}}) d\Omega + \sum_e \int_{\Omega_e} \delta\left[N_{ijB}^\sigma \beta_B^e \left(B_{iA}\dot{d}_A - N_{ijC}^D \alpha_C^e\right)\right] d\Omega \\ - \delta P^{ext} + \delta P^{kin} = 0 \tag{11.33}$$

$$\delta P^{ext} - \delta P^{kin} = \delta\dot{d}_A (f_A^{ext} - M_{AB}\ddot{d}_B) \tag{11.34}$$

For convenience the internal power is written as

$$\delta P_{HW}^{int} = \sum_e \delta\alpha_C^e \tilde{\sigma}_C^e + \delta\left[\beta_B^e \tilde{B}_{BA}^e \dot{d}_A - \beta_B^e G_{BC}^e \alpha_C^e\right] \tag{11.35}$$

Where

$$\tilde{\sigma}_C^e = \int_{\Omega_e} N_{ijC}^D \sigma_{ij}(\bar{\boldsymbol{D}}) d\Omega = \int_{\Omega_e} N_{aC}^D \{\sigma_a(\bar{\boldsymbol{D}})\} d\Omega \text{ or } \{\tilde{\sigma}_C^e\} = \int_{\Omega_e} (\boldsymbol{N}_D)^T \{\boldsymbol{\sigma}(\bar{\boldsymbol{D}})\} d\Omega \tag{11.36}$$

$$\tilde{B}_{BA}^e = \int_{\Omega_e} N_{ijB}^\sigma B_{ijA} d\Omega = \int_{\Omega_e} N_{aB}^\sigma B_{aA} d\Omega \text{ or } \tilde{\boldsymbol{B}}_e = \int_{\Omega_e} \boldsymbol{N}_\sigma^T \boldsymbol{B} d\Omega \tag{11.37}$$

$$G_{BC}^e = \int_{\Omega_e} N_{ijB}^\sigma N_{ijC}^D d\Omega = \int_{\Omega_e} N_{aB}^\sigma N_{aC}^D d\Omega \text{ or } G_e = \int_{\Omega_e} \boldsymbol{N}_\sigma^T \boldsymbol{N_D} d\Omega \tag{11.38}$$

Expanding eq. (11.35) leaves

$$\delta P_{HW}^{int} = \sum_e \delta\alpha_C^e \tilde{\sigma}_C^e + \delta\beta_B^e \tilde{B}_{BA}^e d_A + \beta_B^e \delta\tilde{B}_{BA}^e \dot{d}_A + \beta_B^e \tilde{B}_{BA}^e \delta\dot{d}_A - \delta\beta_B^e G_{BC}^e \alpha_C^e \\ + \beta_B^e \delta G_{BC}^e \alpha_C^e + \beta_B^e G_{BC}^e \delta\alpha_C^e \tag{11.39}$$

Then re-arranging to collect the variation terms

$$\delta P_{HW}^{int} = \sum_{e} \delta\alpha_C^e(\tilde{\sigma}_C^e + \beta_B^e G_{BC}^e) + \delta\beta_B^e(\tilde{B}_{BA}^e \dot{d}_A - G_{BC}^e \alpha_C^e) + \beta_B^e \tilde{B}_{BA}^e \delta\dot{d}_A \tag{11.40}$$

Substituting this into (11.34)

$$\begin{aligned}\delta\Pi_{HW} = \sum_{e} &\delta\alpha_C^e(\tilde{\sigma}_C^e + \beta_B^e G_{BC}^e) + \delta\beta_B^e(\tilde{B}_{BA}^e \dot{d}_A - G_{BC}^e \alpha_C^e) + \beta_B^e \tilde{B}_{BA}^e \delta\dot{d}_A \\ &+ \delta\dot{d}_A(f_A^{ext} - M_{AB}\ddot{d}_B)\end{aligned} \tag{11.41}$$

Which can then be used to obtain the following, by invoking the arbitrariness of each term:

$$f_A^{int,e} = \tilde{B}_{BA}^e \beta_B^e \tag{11.42}$$

$$\tilde{\sigma}_C^e = \beta_B^e G_{BC}^e \tag{11.43}$$

$$\bar{D}_{ij} = N_{ijA}^D (G_{AB}^e)^{-1} \tilde{B}_{BD}^e \dot{d}_D \tag{11.44}$$

Which are all the terms required in order to calculate the internal forces using the mixed method.

11.4 SPH Code Background Stress

```
DO k=1,par(i)%p%nnbr + par(i)%p%n_symnbr
        ipar = i-mcm_sep+1
        if(k.le.par(i)%p%nnbr) then
            j = mcm_eul_nbrlist(k,ipar)
        else
            l  = k - par(i)%p%nnbr
            j  = mcm_eul_sym_nbr(1,l,ipar)

            do m=1,3
                do n=1,3
                    if(m.eq.n) then
                        sigmaj(m,n) = par(j)%p%sigma(m,n)
                        qj(m,n) = par(j)%p%q(m,n)
                    else
                        sigmaj(m,n) = -par(j)%p%sigma(m,n)
                        qj(m,n) = -par(j)%p%q(m,n)
                    endif
                enddo
            enddo

        end if

        !and full stress tensor
        do n=1,mcm_ndim
            do m=1,mcm_ndim
                par(i)%p%sigavg(m,n) = par(i)%p%sigavg(m,n) + (sigmaj(m,n)-
qj(m,n))/par(j)%p%rho**2
            end do
        end do
END DO
    !add i particle contribution, assuming 2d
    do n=1,mcm_ndim
        do m=1,mcm_ndim
par(i)%p%sigavg(m,n) = par(i)%p%sigavg(m,n) + (par(i)%p%sigma(m,n)-
par(i)%p%q(m,n))/par(i)%p%rho**2
par(i)%p%sigavg(m,n) = par(i)%p%sigavg(m,n) / (par(i)%p%nnbr + par(i)%p%n_symnbr + 1)
        end do
    end do
```

11.5 SPH Code – Hu Washizu

```
module populate
    contains

    subroutine populatea(a,o)
    use nrtype
    use mcm_database
    IMPLICIT NONE

    REAL(DP),   DIMENSION(mcm_eep,mcm_eep) :: a
    integer :: i,j,o
    REAL(kind=real_acc) :: W, volj

    do i = mcm_sep, mcm_eep
        do j = mcm_sep, mcm_eep
            volj=par(j)%p%mass/par(j)%p%rho
            if (o.eq.0) then
                call mcm_kernel3(w,par(i)%p%x,par(j)%p%x,par(j)%p%h)
            else
                call mcm_kernel3(w,par(i)%p%x,par(j)%p%x,par(j)%p%h)
            end if
            a(i,j) = volj * W
        end do
    end do



    end subroutine populatea

    subroutine populateb(e,u,m,o,b)
    use nrtype
    use mcm_database
    IMPLICIT NONE


    REAL(DP),  DIMENSION(625) :: b
    REAL(DP),  DIMENSION(625) :: x
    integer :: i,u,m,o,k,j,e
    real::mixedrod2,volj,havg
    REAL(kind=real_acc)    :: W

    if (o.eq.1) then
        do i = mcm_sep, mcm_eep
            mixedrod2=0.0
```

```
            do k=1,par(i)%p%nnbr + par(i)%p%n_symnbr
                j= mcm_eul_nbrlist(k,i)
                volj=par(j)%p%mass/par(j)%p%rho
                havg=(par(i)%p%h+par(j)%p%h)/2
                call mcm_kernel(w,par(i)%p%x,par(j)%p%x,par(i)%p%h)
                mixedrod2=mixedrod2+par(j)%p%rod(u,m)*W*volj
            end do
            !add i particle
            call mcm_kernel(w,par(i)%p%x,par(i)%p%x,par(i)%p%h)
            !for cubic spline
            mixedrod2=mixedrod2 + par(i)%p%rod(u,m) * W * par(i)%p%mass/par(i)%p%rho
            b(i)=par(i)%p%rod(u,m)

        end do

    else
```

```
do i = mcm_sep, mcm_eep

            mixedrod2=0.0
            do k=1,par(i)%p%nnbr + par(i)%p%n_symnbr
                j= mcm_eul_nbrlist(k,i)
                volj=par(j)%p%mass/par(j)%p%rho
                havg=(par(i)%p%h+par(j)%p%h)/2
                call mcm_kernel(w,par(i)%p%x,par(j)%p%x,par(i)%p%h)
                mixedrod2=mixedrod2+par(j)%p%sigma(u,m)*W*volj

            end do
            !add i particle
            call mcm_kernel(w,par(i)%p%x,par(i)%p%x,par(i)%p%h)
            mixedrod2=mixedrod2 + par(i)%p%sigma(u,m) * W * par(i)%p%mass/par(i)%p%rho
            !update rod
            if(u.eq.2) then
                if(m.eq.2) then
                    continue
                end if
            end if
            b(i)=par(i)%p%sigma(u,m)
        end do
    end if


    end subroutine populateb

    subroutine populatex
    use nrtype
    use mcm_database
    IMPLICIT NONE


    REAL(DP),  DIMENSION(625) :: x
    integer :: i
    !if(allocated(x).eqv. .false.) then
    !allocate(x(mcm_eep))
    !end if

    do i = mcm_sep, mcm_eep
        x(i) = 0
        !if (allocated(mcm_mat(1)%X).eqv. .false.) then
        !allocate(mcm_mat(1)%X(mcm_eep))
        !end if
        !!mcm_mat(1)%X(i)=0
    end do
```

```
    end subroutine populatex
    end module populate
```

```
subroutine mixedform(u,m,o)

    use nrtype
    USE xlinbcg_data
    use populate
    use mcm_database
    USE mcm_database; USE nrtype; USE nrutil


    IMPLICIT NONE


    REAL(DP) ,DIMENSION(625, 625) :: a
    REAL(DP) :: thresh,cmin,cmax
    integer :: u,m,o,DeAllocateStatus,e

    REAL(DP), DIMENSION(625) :: b
    REAL(DP), DIMENSION(625) :: x
    REAL(DP), DIMENSION(625) :: v
    INTEGER(I4B) :: itol,itmax
    REAL(DP) :: tol
    INTEGER(I4B) :: iter
    REAL(DP) :: err


call populatex

    thresh =0.000001
    itol=2
    itmax=9999
    tol=0.000001

    if(u.eq.2) then
        if(m.eq.2) then
            continue
        end if
    end if

    call populateb(e,u,m,o,b)
    cmin=minval(b)
    cmax=maxval(b)
    if (cmin.eq.zero) then
        if (cmax.eq.zero) then
            return
        end if
    end if
    if (abs(cmin-cmax).lt.0.0000000001) then
```

```
        return

    end if

    call populatea(a,o)

    call sprsin_dp(a,thresh,sa)

    call linbcg(b,x,itol,tol,itmax,iter,err)

    call mixedrod(x,u,m,o,0,b)

    END SUBROUTINE mixedform
```

```
subroutine mixedrod(x,u,m,o,e,b)
    use mcm_database
    use nrtype
    IMPLICIT NONE

    REAL(DP),  DIMENSION(mcm_eep) :: x
    REAL(DP),  DIMENSION(mcm_eep) :: b
    integer :: u,m,j,o,e
    real(kind=real_acc) :: W, volj,mixedrod2,massj,rhoj,hj,sigmaj,qj,xj(mcm_ndim),havg
    integer :: i,k


    do i = mcm_sep, mcm_eep
        !o=i
        mixedrod2=0.0
        do k=1,par(i)%p%nnbr + par(i)%p%n_symnbr
            j= mcm_eul_nbrlist(k,i)
            !call mcm_get_j_eul_moment_info(i,k,xj,massj,rhoj,hj,sigmaj,qj)
            volj=par(j)%p%mass/par(j)%p%rho

            havg=(par(i)%p%h+par(j)%p%h)/2
            if(o.eq.0) then
                call mcm_kernel(w,par(i)%p%x,par(j)%p%x,havg)
            else
                call mcm_kernel(w,par(i)%p%x,par(j)%p%x,havg)
            end if
            mixedrod2=mixedrod2+x(j)*W*volj
        end do
        !add i particle
        if(o.eq.0) then
            call mcm_kernel(w,par(i)%p%x,par(i)%p%x,par(i)%p%h)
        else
            call mcm_kernel(w,par(i)%p%x,par(i)%p%x,par(i)%p%h)
        end if
        !W=1
        mixedrod2=mixedrod2 + x(i) * W * par(i)%p%mass/par(i)%p%rho
        !update rod
        if(u.eq.2) then
            if(m.eq.2) then
                continue
            end if
        end if
        !print *,par(i)%p%rod(u,m), mixedrod2,mcm_timestep

        if(o.eq.1) then
            if (e.eq.1) then
                par(i)%p%rod(u,m)=x(i)
            else
```

```
                par(i)%p%rod(u,m)=x(i)
            end if
        else
            if (e.eq.0) then
                !par(i)%p%sigma(u,m)=mixedrod2
                par(i)%p%sigma(u,m)=x(i)
            else
                b(i)=x(i)
            end if
        end if
    end do

    end subroutine mixedrod

    subroutine mixedtracerod
    use mcm_database
    implicit none
    integer :: i
    do i = mcm_sep, mcm_eep
        par(i)%p%tracerod=par(i)%p%rod(1,1)+ par(i)%p%rod(2,2)+par(i)%p%rod(3,3)
    end do
    end subroutine mixedtracerod
```

11.6 SPH Code – Friction Contact

```
SUBROUTINE mcm_rep_cont
.
.
.
! Main body of code is ommited
```

```
!friction here
!project the relative velocity vector onto the plane tangential to the contact
force between each contact pair.
            !the resulting vector will be the direction of the friction force.
            !take triple cross product of normal force and relative velocity f X
(f X V) = f(f.v) - v(f.f)

            !find f.f and f.v
            fdotv=0
            fdotf=0

            do l = 1,mcm_ndim
            fdotv=fdotv+par(i)%p%repulsion(l)*par(i)%p%vij(l)
            fdotf=fdotf+par(i)%p%repulsion(l)*par(i)%p%repulsion(l)
            end do

            !calculate f(f.v) - v(f.f). The resulting vector has
the correct direction              but the magnitude is that of the relative
velocity, need to normalise.
            len=0.0
            len2=0.0
            do l = 1,mcm_ndim
                velocity_ij(l)=par(i)%p%repulsion(l)*fdotv -
par(i)%p%vij(l)*fdotf
                len=len+velocity_ij(l)**2
                len2=len2 + par(i)%p%vij(l)**2

            end do


            !acceleration required to bring particle to rest over timestep
            !rest = sqrt(len2)/mcm_dt

            if (abs(len).le.1e-10) then
                friction_ij=0.0
                else

            !find length of vector and normalise
```

```
            len=sqrt(len)
            do l = 1,mcm_ndim
            friction_ij(l)=velocity_ij(l)/len

            end do

            vdotcf=0.0
            do l = 1,mcm_ndim
            vdotcf=vdotcf+(par(i)%p%vij(l)/par(i)%p%ncont)*friction_ij(l)
            end do

            rest = abs(vdotcf/mcm_dt)

            !find magnitude of contact force.
            len=0.0
            do l = 1,mcm_ndim
                len = len + par(i)%p%repulsion(l)**2

            end do
            len=sqrt(len)
                end if

                !is yield force greater than that required to bring particle to
rest over the timestep

                !velocity in direction of relative motion
                 !coefficient of friction
                len=len*0
                if (len.gt.rest) then
                    len=rest
                else
                    len=len
                end if

                area=(par(i)%p%h**2)/(1.3**2)
                !k1=1.44E+08
                !len=min(len, area*k1/par(i)%p%mass)




            do l = 1,mcm_ndim

              par(i)%p%repulsion(l) = par(i)%p%repulsion(l) +(friction_ij(l)*len)

            enddo
```

```
      !
    endif

  enddo
```

```
.
.
.
!Main body of code is ommited

end subroutine mcm_rep_cont
```